

INVESTIGATIONS OF CONDUCTION MECHANISMS OF ION-CONDUCTING,  
BRIDGING MEMORY DEVICES (CBRAM/PMC/ECM)

by

Kyle Bradley Campbell

A thesis

submitted in partial fulfillment

of the requirements for the degree of

Master of Science in Electrical Engineering

Boise State University

August 2012

© 2012

Kyle Bradley Campbell

ALL RIGHTS RESERVED

BOISE STATE UNIVERSITY GRADUATE COLLEGE

**DEFENSE COMMITTEE AND FINAL READING APPROVALS**

of the thesis submitted by

Kyle Bradley Campbell

Thesis Title: Investigations of Conduction Mechanisms of Ion-Conducting, Bridging Memory Devices (CBRAM/PMC/ECM)

Date of Final Oral Examination: 11 May 2012

The following individuals read and discussed the thesis submitted by student Kyle Bradley Campbell, and they evaluated his presentation and response to questions during the final oral examination. They found that the student passed the final oral examination.

Kristy A. Campbell, Ph.D. Chair, Supervisory Committee

Jim Browning, Ph.D. Member, Supervisory Committee

Vishal Saxena, Ph.D. Member, Supervisory Committee

The final reading approval of the thesis was granted by Kristy A. Campbell, Ph.D., Chair of the Supervisory Committee. The thesis was approved for the Graduate College by John R. Pelton, Ph.D., Dean of the Graduate College.

## ACKNOWLEDGEMENTS

I'd like to articulate my most profound thanks to the individuals without which I could not have completed this work. First, I'd like to thank my advisor Dr. Kristy A. Campbell. Her continual willingness to guide this work to its culmination has been critical to its success. I could not be more grateful for the use of the lab equipment and devices to make this research, experimentation, and analysis possible. I would also like to thank the committee members, Dr. Jim Browning and Dr. Vishal Saxena, who have made this achievement possible.

Also, I would like to thank Dr. Jennifer Regner for device fabrication. Also, Korey Moeller must be thanked for fabrication assistance. Terry Gafron has provided invaluable assistance with lab needs, especially fixing the low temp probe station vibration problem that clouded the data. Antonio Oblea provided excellent training in the safe and effective use of the low temp probe station.

I'd like to thank Micron Technology, especially my supervisors, Walt Rogers and Curtis Norris, for supporting me as I completed this work during my full time employment at Micron.

Finally, I would like to thank my wonderful wife, Jennifer Campbell, who has been a solid foundation of support during this effort. She gave me the powerful encouragement needed to sustain my progress in this endeavor, and I couldn't be happier to have her on my side.

## ABSTRACT

Electron storage memory devices are approaching the minimum dimensions that are physically possible due to the onward march of Moore's law. To continue to enable the increased memory densities needed for today's applications, especially low power and size constrained mobile devices, new memory solutions are needed. Several candidates are emerging in this space. Metal ion-conducting memory devices are being investigated due to excellent scalability, speed, and low power. These devices are part of a memory class called resistive memory. In the literature, they are referred to as CBRAM (conductive bridge random access memory), PMC (programmable metallization cell), ECM (electrochemical metallization cell), and Atomic Switch.

This work seeks to understand the ion-conduction mechanisms that are occurring in switching devices comprised of W/Ge<sub>32</sub>Se<sub>68</sub>/Ag, bottom to top, called Ag-only throughout, and in switching devices comprised of W/Ge<sub>32</sub>Se<sub>68</sub>/SnSe/Ag/W, bottom to top, called Ag+SnSe throughout. Additionally, the electron-conduction mechanisms in the Ge<sub>32</sub>Se<sub>68</sub> memory layer are investigated using devices comprised of W/Ge<sub>32</sub>Se<sub>68</sub>/W. The experimental method used to analyze the devices was DC voltage sweep across multiple temperatures over the range of 300 K to 10 K.

## TABLE OF CONTENTS

ACKNOWLEDGEMENTS .....	iv
ABSTRACT .....	v
LIST OF TABLES .....	xi
LIST OF FIGURES .....	xii
CHAPTER 1: INTRODUCTION .....	1
1.1 Introduction and Motivation .....	1
1.1.1 Description of Resistive Memory Technologies.....	2
1.2 Theories of Conduction in Ion-Conducting Bridging Memory .....	9
1.2.1 Metal Ions: Butler-Volmer Equation for Electrode Redox.....	10
1.2.2 Metal Ions: Mott-Gurney Hopping .....	12
1.2.3 Alternate Theory to Mott-Gurney Ion Hopping: Electron Tunneling Between Adjacent Impurity Sites.....	13
1.2.4 Electrons: Schottky Thermionic Emission.....	13
1.2.5 Electrons: Band Conduction in the Extended States.....	14
1.2.6 Electrons: Mott's $T^{1/4}$ Variable Range Hopping.....	15
1.2.7 Electrons: Poole-Frenkel Emission.....	16
1.2.8 Electrons: Fowler-Nordheim Tunneling.....	17
1.3 Device Structure.....	18
1.3.1 Structure of Resistive $\text{Ge}_{32}\text{Se}_{68}$ Test Devices .....	18
1.3.2 Structure of Silver Ion-Conducting Devices.....	19
CHAPTER 2: EXPERIMENTAL.....	21
2.1 Introduction.....	21

2.2 Device Fabrication .....	21
2.2.1 Device Fabrication .....	21
2.3 Test Equipment and Software Used.....	22
2.3.1 Low Temperature Probe Station .....	22
2.3.2 Probes.....	26
2.3.3 HP 4156A Semiconductor Parameter Analyzer .....	27
2.3.4 Triaxial Cables .....	27
2.3.5 Semiconductor Parameter Analyzer Control Software - MCP2 .....	28
2.4 Testing Procedures.....	28
2.4.1 General Low Temperature Testing Procedure.....	28
2.4.2 Die Layout .....	29
2.4.3 Testing of 300 Å Ge <sub>32</sub> Se <sub>68</sub> .....	30
2.4.4 Testing of Ag-Only and Ag+SnSe Devices .....	30
2.5 Data Analysis Procedures .....	31
2.5.1 Ge <sub>32</sub> Se <sub>68</sub> Devices – Electron Conduction .....	31
2.5.2 Ag-Only and Ag+SnSe Devices. ....	32
2.6 Experimental Summary .....	34
CHAPTER 3: CONDUCTION MECHANISMS OF 300 Å Ge <sub>32</sub> Se <sub>68</sub> .....	35
3.1 Introduction.....	35
3.2 IV Traces.....	36
3.2.1 IV Traces – 1 <sup>st</sup> Device.....	36
3.2.2 IV Traces – 2 <sup>nd</sup> Device.....	37
3.2.3 IV Traces – 3 <sup>rd</sup> Device .....	38
3.2.4 IV Traces – 4 <sup>th</sup> Device .....	39
3.2.5 IV Traces – 5 <sup>th</sup> Device .....	40

3.2.6 IV Traces – 6 <sup>th</sup> Device .....	41
3.2.7 Layout of Six Ge <sub>32</sub> Se <sub>68</sub> Devices by Temperature .....	42
3.2.8 Overlay of Six Ge <sub>32</sub> Se <sub>68</sub> Devices by Temperature.....	44
3.2.9 Summary of Qualitative Assessment of IV Traces.....	44
3.3 Conduction Mechanisms of 300 Å Ge <sub>32</sub> Se <sub>68</sub> .....	45
3.3.1 Band Conduction in the Extended States.....	45
3.3.2 Mott's T <sup>1/4</sup> Variable Range Hopping.....	48
3.3.3 Schottky Emission .....	50
3.3.4 Poole-Frenkel Emission.....	54
3.3.5 Fowler-Nordheim Tunneling.....	60
3.3.6 Conclusion of Conduction Mechanisms in 300 Å Ge <sub>32</sub> Se <sub>68</sub> .....	62
CHAPTER 4: WRITE CHARACTERISTICS OF ION-CONDUCTING SWITCHING DEVICES .....	65
4.1 Experimental Summary .....	65
4.1.1 Experimental Procedure – Devices Tested .....	66
4.1.2 Electrical Testing Sequences .....	67
4.1.3 Experimental Procedure – Temperature Measurements .....	69
4.1.4 Conduction Mechanisms.....	69
4.1.5 Notes on Potential Experimental Error .....	70
4.2 Electron Conduction During Write Process.....	71
4.3 Ag-Only Switching Device Write Characteristics – Devices Retested Across Temperatures .....	71
4.3.1 IV Traces of Ag-Only Ion-Conducting Ge <sub>32</sub> Se <sub>68</sub> Devices.....	72
4.3.2 Layout Plot of IV Write Traces of Ag-Only Devices Retested at Each Temperature .....	74
4.3.3 Ion-Conduction Mechanisms Comments.....	75

4.3.4	Threshold Voltage Characteristics.....	75
4.4	Ag-Only Switching Device Write Characteristics – Fresh Devices at Each Temperature.....	77
4.4.1	Write Traces of Ag-Only Fresh Devices.....	77
4.4.2	Threshold Voltage Characteristics of Ag-Only Write Traces for Fresh Devices.....	79
4.5	Ag+SnSe Switching Device Write Characteristics – Devices Retested Across Temperatures.....	81
4.5.1	IV Traces of Ag+SnSe Ion-Conducting Ge <sub>32</sub> Se <sub>68</sub> Devices.....	81
4.5.2	Layout Plot of IV Write Traces of Ag+SnSe Devices Retested at Each Temperature.....	83
4.5.3	Ion-Conduction Mechanisms of Ag+SnSe Devices Retested at Each Temperature.....	85
4.5.4	Threshold Voltage Characteristics of Ag+SnSe Devices Retested at Each Temperature.....	86
4.6	Ag+SnSe Switching Device Write Characteristics – Fresh Devices at Each Temperature.....	88
4.6.1	Write Traces of Ag+SnSe Fresh Devices.....	88
4.6.2	Threshold Voltage Characteristics of Ag+SnSe Write Traces for Fresh Devices.....	90
4.7	Post Write Resistance Characteristics.....	91
4.8	Conclusion of Writing Characteristics.....	94
4.8.1	Conduction Mechanisms.....	94
4.8.2	Threshold Voltage Characteristics.....	94
4.8.3	Resistance Characteristics.....	97
CHAPTER 5:	ERASE CHARACTERISTICS.....	98
5.1	Summary.....	98
5.2	Experimental Procedure for Erase.....	98
5.2.1	Procedure for Devices Retested at Each Temperature.....	98

5.2.2 Procedure for Devices Tested for the First Time at Each Temperature .....	99
5.3 Erase Traces for Devices Retested at Each Temperature .....	100
5.3.1 Erase Traces for Ag-Only Devices .....	100
5.3.2 Erase Traces for Ag+SnSe Devices .....	103
5.4 Erase Traces of Devices Tested Fresh at Each Temperature .....	106
5.4.1 Ag-Only Erase Traces.....	106
5.4.2 Ag+SnSe Erase Traces.....	107
5.5 Resistance Characteristics of Devices After Erase .....	107
5.6 Conclusion of Erase Characteristics .....	108
CHAPTER 6 : CONCLUSION .....	110
6.1 Introduction.....	110
6.2 Overview of Work .....	110
6.2.1 Devices Tested.....	111
6.2.2 Experiment Groups Within Devices .....	111
6.2.3 Conduction Mechanisms Investigated.....	112
6.3 Results.....	112
6.3.1 Electron Conduction in Ge <sub>32</sub> Se <sub>68</sub> .....	112
6.3.2 Conduction in Ag-Only and Ag+SnSe Switching Devices .....	113
6.3.3 Threshold Voltage Characteristics.....	113
6.3.4 Resistance Characteristics in Ag-Only and Ag+SnSe Switching Devices .....	114
6.3.5 Erase Characteristics.....	114
6.4 Future Work .....	115
6.5 Summary .....	115
REFERENCES .....	117

## LIST OF TABLES

Table 2.1	Summary of Transformations Performed on IV Traces of Resistive 300 Å Ge <sub>32</sub> Se <sub>68</sub> Devices to Determine Conduction Mechanism .....	32
Table 2.2	Summary of Parameters Collected from Ion-Conducting Switching Devices.....	32
Table 2.3	Summary of Ion-Conduction Mechanism Transformations Performed on the Write Traces of Ion-Conducting Switching Devices .....	33
Table 3.1	Summary of Electron Conduction Mechanism Results for 300 Å Ge <sub>32</sub> Se <sub>68</sub> .....	63
Table 4.1	Sequence of Testing for Fresh Switching Devices.....	68
Table 4.2	Sequence of Testing for Switching Devices Retested at Each Temperature .....	68
Table 4.3	Transformations Performed on Write Traces to Determine Ion- Conduction Mechanism .....	70
Table 4.4	Conductance at Threshold Activation Energies for Ag-Only Devices Retested Across Temperatures.....	77
Table 4.5	Temperatures where Ag+SnSe Devices Retested at Each Temperature Had Exponential Performance .....	85
Table 4.6	Activation energy for conductance at threshold for Ag+SnSe devices retested across temperatures .....	88
Table 4.7	Summary of Arrhenius Activation Energy of Conductance at Threshold for Devices Retested Across Temperatures.....	95
Table 4.8	Summary of Arrhenius Activation Energy of Conductance at Threshold for Devices Tested Fresh at Each Temperature Calculated from 200 K to 300 K.....	96
Table 5.1	Electrical Sequence for Devices Retested at Each Temperature .....	99
Table 5.2	Sequence of Testing for Fresh Switching Devices .....	100

## LIST OF FIGURES

Figure 1.1	Operation of a PCRAM Device, Red=Amorphous; Blue=Crystalline. (a) represents the high-resistance state, (b) is intermediate, and (c) represents low resistance.....	3
Figure 1.2	Image of a silver dendrite bridging the gap.....	4
Figure 1.3	Schematic of operation of CBRAM device.....	5
Figure 1.4	Schematic of filament formation and subsequent radial growth.....	6
Figure 1.5	Time required to erase based on written resistance and based on erase voltage.....	7
Figure 1.6	Comparison of write energy and switching speed of memory technologies. ....	7
Figure 1.7	Temperature dependence of device resistance from Hirose and Hirose.....	8
Figure 1.8	Butler-Volmer current-overpotential curve showing cathode and anode current ( $i_c$ and $i_a$ ). ....	11
Figure 1.9	Energy band diagram of an amorphous semiconductor. ....	15
Figure 1.10	Energy band diagram of a MOS structure with large applied positive voltage showing Fowler-Nordheim Tunneling. ....	17
Figure 1.11	Cross-sectional diagram of resistive memory layer test device with 300 Å $\text{Ge}_{32}\text{Se}_{68}$ .....	19
Figure 1.12	Cross-sectional diagram of silver-only ion-conducting test device. ....	19
Figure 1.13	Cross-sectional diagram of the Ag and SnSe ion-conducting device.....	20
Figure 2.1	LakeShore CRX-4K Probe Station.....	23
Figure 2.2	View of interior of vacuum chamber with sample stage exposed.....	23
Figure 2.3	LakeShore Model 340 temperature controllers.....	24
Figure 2.4	Sumitomo F-50 Cryocooler compressor unit. ....	24

Figure 2.5	Sumitomo SRDK Series cryocooler system – high-pressure helium supply lines. ....	25
Figure 2.6	Sumitomo SRDK Series cryocooler system – cold head. ....	26
Figure 2.7	LakeShore ZN50R-25-W probe. ....	26
Figure 2.8	HP 4156A Semiconductor parameter analyzer. ....	27
Figure 2.9	Illustration of importance of triaxial cabling for low current measurements.....	28
Figure 2.10	Die layout example showing device arrangement.....	30
Figure 3.1	Current-voltage traces of 300 Å Ge <sub>32</sub> Se <sub>68</sub> resistive memory layer device cycled 20 times.....	36
Figure 3.2	IV Traces of first 300 Å Ge <sub>32</sub> Se <sub>68</sub> device from 10 K to 300 K. ....	37
Figure 3.3	IV Traces of second 300 Å Ge <sub>32</sub> Se <sub>68</sub> device from 10 K to 300 K.....	38
Figure 3.4	IV Traces of third 300 Å Ge <sub>32</sub> Se <sub>68</sub> device from 10 K to 300 K. ....	39
Figure 3.5	IV Traces of fourth 300 Å Ge <sub>32</sub> Se <sub>68</sub> device from 10 K to 300 K. ....	40
Figure 3.6	IV Traces of fifth 300 Å Ge <sub>32</sub> Se <sub>68</sub> device from 10 K to 300 K.....	41
Figure 3.7	IV Traces of sixth 300 Å Ge <sub>32</sub> Se <sub>68</sub> device from 10 K to 300 K. ....	42
Figure 3.8	Layout plot of IV traces of six Ge <sub>32</sub> Se <sub>68</sub> Devices.....	43
Figure 3.9	Overlay of IV traces of the six devices, 300 Å Ge <sub>32</sub> Se <sub>68</sub> , that were retested at each temperature from 10 K to 300 K. ....	44
Figure 3.10	Arrhenius extended states band conduction plot from 10 K to 300 K of first and fifth 300 Å Ge <sub>32</sub> Se <sub>68</sub> devices. ....	46
Figure 3.11	Arrhenius extended states fit for 200 K to 300 K of first and fifth 300 Å Ge <sub>32</sub> Se <sub>68</sub> devices.....	47
Figure 3.12	Extended states conduction plot from 100 K to 300 K for first and fifth 300 Å Ge <sub>32</sub> Se <sub>68</sub> devices.....	47
Figure 3.13	Mott’s Variable Range Hopping Plot of first and fifth 300 Å Ge <sub>32</sub> Se <sub>68</sub> devices.....	48
Figure 3.14	Mott’s Variable Range Hopping fit for 200 K to 300 K for first and fifth 300 Å Ge <sub>32</sub> Se <sub>68</sub> devices.....	49

Figure 3.15	Mott VRH plot from 300 K to 100 K for first and fifth 300 Å $\text{Ge}_{32}\text{Se}_{68}$ devices.....	50
Figure 3.16	Schottky transformations of first 300 Å $\text{Ge}_{32}\text{Se}_{68}$ device.....	51
Figure 3.17	Slopes of Schottky transformations for first 300 Å $\text{Ge}_{32}\text{Se}_{68}$ device against inverse temperature.....	52
Figure 3.18	Schottky transformations of fifth 300 Å $\text{Ge}_{32}\text{Se}_{68}$ device. ....	53
Figure 3.19	Slopes of Schottky transformations for fifth 300 Å $\text{Ge}_{32}\text{Se}_{68}$ device against inverse temperature.....	54
Figure 3.20	Poole-Frenkel current-voltage transformations of first 300 Å $\text{Ge}_{32}\text{Se}_{68}$ device. ....	56
Figure 3.21	Slopes of Poole-Frenkel transformations for first 300 Å $\text{Ge}_{32}\text{Se}_{68}$ device against $1/T$ . ....	57
Figure 3.22	Y-intercept of Poole-Frenkel transformations for the first 300 Å $\text{Ge}_{32}\text{Se}_{68}$ device. ....	57
Figure 3.23	Poole-Frenkel current-voltage transformations of fifth 300 Å $\text{Ge}_{32}\text{Se}_{68}$ device. ....	58
Figure 3.24	Poole-Frenkel y-intercept of fifth 300 Å $\text{Ge}_{32}\text{Se}_{68}$ device against $1/T$ . ....	59
Figure 3.25	Slopes of Poole-Frenkel transformations for fifth 300 Å $\text{Ge}_{32}\text{Se}_{68}$ device plotted against $1/T$ . ....	59
Figure 3.26	Fowler-Nordheim tunneling current-voltage transformations for first 300 Å $\text{Ge}_{32}\text{Se}_{68}$ device.....	61
Figure 3.27	Fowler-Nordheim tunneling current-voltage transformations for fifth 300 Å $\text{Ge}_{32}\text{Se}_{68}$ device. ....	62
Figure 4.1	Cross-sectional diagram of Ag-only ion-conducting test device. ....	65
Figure 4.2	Cross-sectional diagram of the Ag+SnSe ion-conducting device. ....	66
Figure 4.3	Image of top electrode damage at 50 K of fresh Ag+SnSe device.....	71
Figure 4.4	IV traces of 50 $\mu\text{A}$ write for Ag-only switching device #1 retested across temperatures.....	72
Figure 4.5	IV traces of 50 $\mu\text{A}$ write for Ag-only switching device #2 retested across temperatures.....	73

Figure 4.6	IV traces of 50 $\mu$ A write for Ag-only switching device #3 retested across temperatures.....	73
Figure 4.7	Layout plot of IV write traces of Ag-only Devices Retested Across Temperatures.....	74
Figure 4.8	Threshold voltage of Ag-only devices retested across temperatures. ....	76
Figure 4.9	Arrhenius plot of conductance at threshold for Ag-only devices retested across temperatures. ....	76
Figure 4.10	First write traces for fresh Ag-only devices from 300 K to 10 K.....	78
Figure 4.11	Second write traces for fresh Ag-only devices from 300 K to 10 K. ....	79
Figure 4.12	Threshold voltages of fresh Ag-only first and second writes.....	80
Figure 4.13	Arrhenius plot of conductance at threshold for Ag-only fresh devices.....	80
Figure 4.14	IV traces of 50 $\mu$ A write for Ag+SnSe switching device #1 retested across temperatures.....	81
Figure 4.15	IV traces of 50 $\mu$ A write for Ag+SnSe switching device #2 retested across temperatures.....	82
Figure 4.16	IV traces of 50 $\mu$ A write for Ag+SnSe switching device #3 retested across temperatures.....	83
Figure 4.17	Layout Plot of IV Write Traces of Ag+SnSe Devices Retested at Each Temperature.....	84
Figure 4.18	Calculated MG ion hopping distance for Ag+SnSe devices retested at each temperature. ....	86
Figure 4.19	Threshold voltages of Ag+SnSe devices retested across temperatures.....	87
Figure 4.20	Arrhenius plot of conductance at threshold for Ag+SnSe devices retested across temperatures. ....	87
Figure 4.21	First write traces for fresh Ag+SnSe devices from 300 K to 10 K. ....	89
Figure 4.22	Second write traces for fresh Ag+SnSe devices from 300 K to 10 K. ....	90
Figure 4.23	Threshold voltages of fresh Ag+SnSe first and second writes.....	90
Figure 4.24	Arrhenius plot of conductance at threshold for Ag+SnSe fresh devices.....	91

Figure 4.25	Post write and erased resistance of devices retested across temperatures.....	92
Figure 4.26	Post write and erase resistances for “fresh” Ag-only devices.....	93
Figure 4.27	Post write and erased resistances for “fresh” Ag+SnSe devices.....	93
Figure 4.28	Overlay of threshold voltage for Ag-only and Ag+SnSe devices retested across temperatures.....	95
Figure 4.29	Overlay of threshold voltages for all devices tested fresh at each temperature.....	96
Figure 5.1	Erase traces for Ag-only device 1 retested across temperatures.....	101
Figure 5.2	Erase traces for Ag-only device 2 retested across temperatures.....	102
Figure 5.3	Erase traces for Ag-only device 3 retested across temperatures.....	103
Figure 5.4	Erase traces for Ag+SnSe device 1 retested across temperatures.....	104
Figure 5.5	Erase traces for Ag+SnSe device 2 retested across temperatures.....	105
Figure 5.6	Erase traces for Ag+SnSe device 3 retested across temperatures.....	105
Figure 5.7	Erase traces for fresh Ag-only devices at each temp.....	106
Figure 5.8	Erase traces for fresh Ag+SnSe devices at each temp.....	107
Figure 5.9	Resistance values of fresh devices after erase across temperatures.....	108

## CHAPTER 1: INTRODUCTION

### 1.1 Introduction and Motivation

As memory technologies become more advanced, device dimensions have become smaller and smaller. The aggressive scaling has exposed critical problems for conventional charge storage technologies such as capacitor-based Dynamic Random Access Memory (DRAM) and floating-gate flash memory. For advanced DRAM, it is increasingly difficult to build small footprint capacitors with enough capacitance to store detectable data. Flash memory suffers from low endurance, slow speed, and high write voltages [1]. To build flash memory that meets customer requirements, the next generations may require innovations such as charge trap [2] and 3D stacking [3], which are difficult and expensive.

Very soon, it will be necessary to replace conventional memory technologies with new technology that does not depend on storing electrons. Several possible technologies are under investigation such as ferroelectric RAM, magnetoresistive RAM, and a broad class of technologies called electrical resistance switching RAM. Within the group, there are the technologies of phase-change memory (PCRAM), metal oxide valence change (ReRAM), and ion-conducting bridging memory (called CBRAM, PMC, and ECM). The latter is of particular interest and is the topic of this thesis.

### 1.1.1 Description of Resistive Memory Technologies

Resistive memory technologies are designed using a metal-insulator-metal (MIM) structure. Using an applied potential, the resistance of the device is changed. Detection using low potential is required to avoid changing the resistance state of the device. Within this basic framework, there are essentially three competing technologies that are in various stages of manufacturing development. Those technologies are phase-change memory (PCRAM), valence-change memory (ReRAM, MVO), and ion-conducting bridging memory (CBRAM, ECM, PMC). The ion-conducting bridging memories are the topic of this work.

#### 1.1.1.1 Phase-Change Memory (PCRAM)

The technology that has already been introduced into production is phase-change memory (PCRAM). Phase-change is based on the ability of chalcogenide material, typically  $\text{Ge}_2\text{Sb}_2\text{Te}_5$ , to change structure from amorphous to crystalline and back, which corresponds to a change in material resistance. It was first reported in 1968 by Ovshinsky [4]. This technology, although being the farthest along in development of resistive-switching memories, suffers from some difficulties. One difficulty is structural stability after multiple cycles. It has been shown that after many cycles, there is a phase separation of Te [5]. Other difficulties are crystallization, structural relaxation, program disturb, and read disturb [6]. The general method of operation is shown in Figure 1.1 [6].

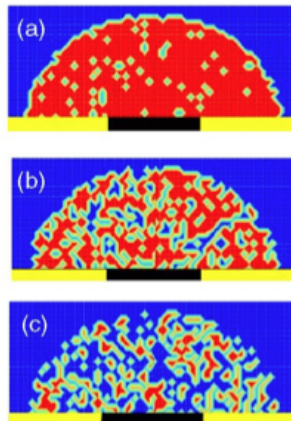


**Figure 1.1** Operation of a PCRAM Device, Red=Amorphous; Blue=Crystalline. (a) represents the high-resistance state, (b) is intermediate, and (c) represents low resistance [6].

#### 1.1.1.2 Valence-Change Memory

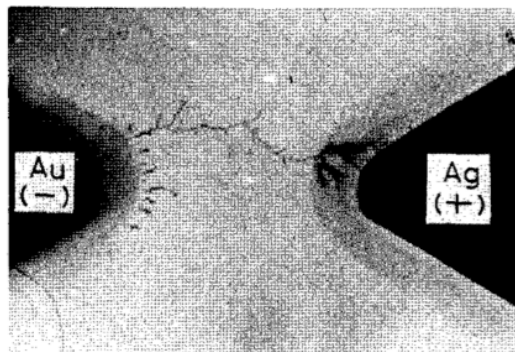
As a type of resistive memory, valence change is implemented as a system where oxygen vacancies can move. One example of such a device was implemented in the configuration Pt-TiO<sub>2-x</sub>-Pt [7]. Applying a voltage moves oxygen vacancies from the conductive TiO<sub>2-x</sub> layer into the insulating TiO<sub>2</sub> layer, causing the device to be more conductive. Reversing the polarity moves the oxygen vacancies back where it started, thus making the device more resistive. Another implementation of valence-change memory is the use of PCMO (Pr-Ca-Mn Oxide) as the memory material [8].

#### 1.1.1.3 Ion-Conducting Bridging Memory (CBRAM, PMC, ECM)

A promising candidate for next-generation memory and the topic of this work is ion-conducting bridging RAM. It is referred to as CBRAM (conductive bridge RAM), ECM (electrochemical metallization memory), and PMC (programmable metallization cell) to name a few. The device is comprised of an ion-conducting resistive material, often a binary chalcogenide, between two electrodes. The anode is made of a readily

oxidizable metal such as Ag or Cu. The cathode is made of a non-oxidizable metal such as W or Pt. The memory effect of these materials was first reported in 1976 by Hirose and Hirose [9]. Using Ag photodoped  $As_2S_3$  as an ion-conducting memory layer, a silver anode, and a platinum cathode, reversible electrical resistance switching was demonstrated.

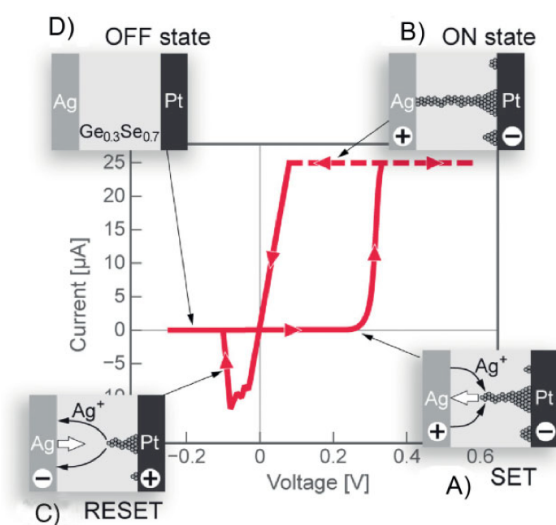
When an electric field is applied, an electrochemical reaction takes place at the anode-chalcogenide interface that generates silver ions. Because of the electric field, the ions travel across the chalcogenide memory layer and are reduced at the tungsten cathode. A metal filament forms that bridges the gap between cathode and anode, and eventually shorts the device. Once the gap is bridged, the device goes from high resistance to low resistance. An image of a bridged device from the Hirose and Hirose paper is shown in Figure 1.2 [9].



**Figure 1.2** Image of a silver dendrite bridging the gap [9].

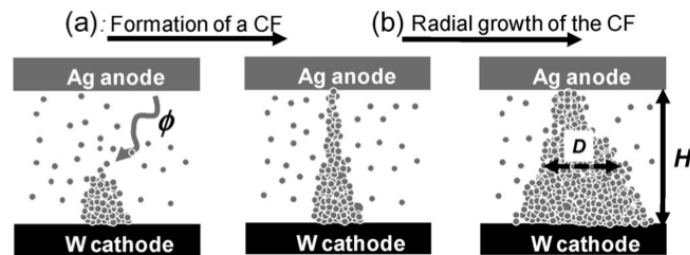
When the electric field is reversed, the silver filament dissolves. Most silver returns to the anode, while some silver remains in the memory layer. The device is then high resistance again.

Figure 1.3 schematically shows how the ion-conducting memory device works [10]. Starting with A), the write operation, the voltage increases. Silver oxidizes at the anode and migrates under the electric field to reduce on the cathode. A silver filament begins to form on the cathode. As the applied voltage increases, the Ag filament bridges the gap. Current flow immediately increases, as the filament provides a much lower resistance path between the two electrodes. The device is now written (B). In the Figure 1.3 example, the maximum compliance current is set to 25  $\mu\text{A}$ . Next, the applied voltage is reduced. The current-voltage response is linear at low voltages, since the filament is acting like a resistor. When the applied voltage is negative, the silver begins to oxidize from the filament and migrate back toward the Ag anode. When a gap opens in the filament, and silver no longer bridges the electrodes, the current immediately drops (C). As the voltage is driven more negative, most silver returns to the anode, and the device is fully erased (D). The resistance of the erased state is usually several orders of magnitude higher than the written state, allowing the device to act as memory.



**Figure 1.3 Schematic of operation of CBRAM device [10].**

Multiple resistance states have been demonstrated by changing the compliance current [11]. A possible explanation for the phenomenon is the radial growth of the filament with higher current. A schematic representation is shown in Figure 1.4 [11], where there is initial electrodeposition of silver on the cathode, formation of the filament, and radial growth. The possibility of multiple resistance states means that multibit storage per cell may be possible.



**Figure 1.4 Schematic of filament formation and subsequent radial growth [11].**

In addition to the possibility of multiple resistance states, there may be quantization of the conductance [12]. The conductive bridge may be narrowing to the atomic level. Conductance values may be in multiples of the fundamental conductance  $G_0 = 2e^2/h$  [12], which may mean the device can have conductive filaments as small as one atom wide. On the other hand, for very low written resistances, there may be radial growth of the filament as shown in Figure 1.4. With a large filament with a large amount of silver (low resistance), it may take more time or voltage to erase. The time needed to erase the cell has been shown to depend both on the erase voltage used and on the written resistance of the device [13]. Figure 1.5 shows that low-resistance devices take longer to erase than high-resistance devices, and it shows that lower erase voltages result in longer erase times [13].

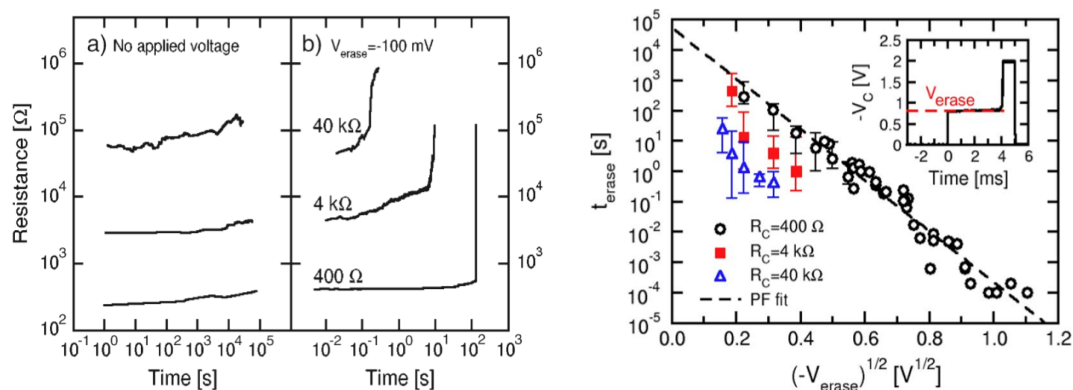


**Figure 1.5** Time required to erase based on written resistance and based on erase voltage [13].

One advantage of ionic memory is that the energy required to write the cell is much less than other resistive memories, such as phase-change memory (PCM) [14]. Device speed is graphed against write energy for competing memory technologies in Figure 1.6 [14]. The size of the circles indicates relative operating voltage. Ionic memory may operate at lower voltages than some competing technologies.

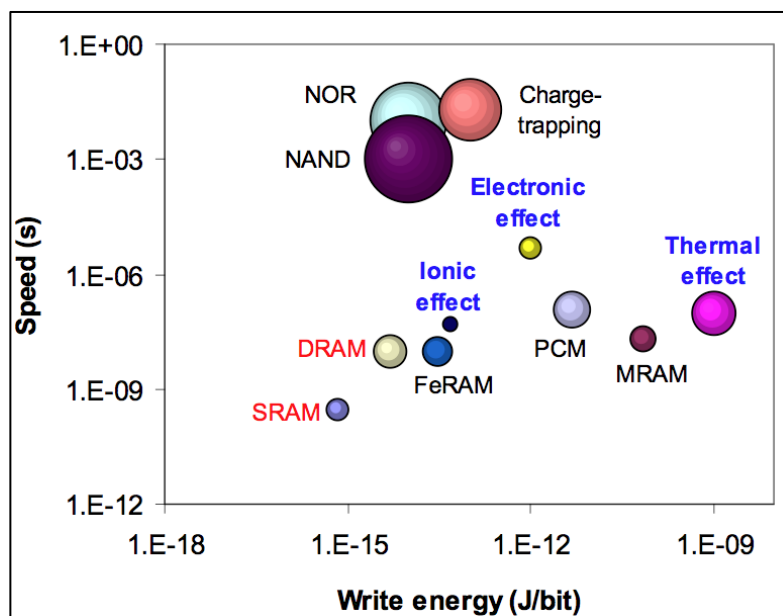


**Figure 1.6** Comparison of write energy and switching speed of memory technologies [14].

The structure of the chalcogenide memory layer is important. In many cases, it is fabricated as a binary chalcogenide, such as  $\text{Ge}_x\text{Se}_y$ . The first write may take more time, since Ag traverses the entire gap. Subsequent writes may be faster since the path has already been formed, and silver will already be available in the memory layer to quickly form a new filament. Some have incorporated silver into the memory layer to speed up the first write [10].

Hirose and Hirose showed that when the device's gap has been bridged, the resistance characteristics are metallic; while in the erased state, the resistance characteristic behaves as a semiconductor. Figure 1.7 shows that when the device is bridged, the resistance characteristics match that of metallic Ag; when erased, the resistance characteristic is like a semiconductor with increasing resistance at lower temperatures [9]. The reason the characteristic of the conduction is important is that it reinforces the idea that there is a metallic filament acting as the conductor when the device is written. When the device is erased, the resistive memory layer does not have metallic conduction. In other words, in the erased state, there is no metal conductor.

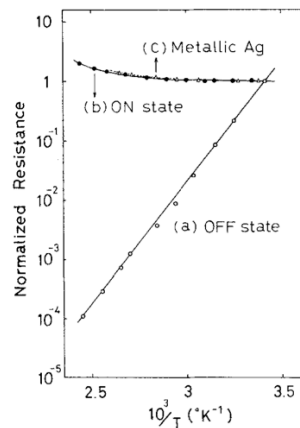


**Figure 1.7** Temperature dependence of device resistance from Hirose and Hirose [9].

## 1.2 Theories of Conduction in Ion-Conducting Bridging Memory

For writing, the process consists of three steps. The first step is the oxidation at the anode. It proceeds according to the reaction in Eqn. 1.1.



Next, silver ions migrate across the memory layer under an electric field. Lastly, the ions reduce at the cathode according to the reaction in Eqn. 1.2.



The kinetics of silver motion are broken into two parts: the Butler-Volmer equation modeling the anode and cathode reaction [15], and the migration of ions through the chalcogenide memory layer modeled by the Mott and Gurney thermally activated ion-hopping mechanism [10].

Additionally, there is electron flow in the chalcogenide memory layer that contributes to conduction during the write and erase. There are several known electron-conduction mechanisms that can occur in high resistance amorphous materials.

The electron-conduction mechanisms that were investigated in this work are:

- Band conduction in the extended states: a process that occurs in amorphous semiconductors that is analogous to conduction band and valence band carrier motion in crystalline semiconductors.
- Mott's  $T^{1/4}$  variable range hopping: a process of electrons hopping between localized states in the forbidden energy band. It is known to dominate at low temperatures in amorphous semiconductors.
- Schottky emission: an electrode process of electrons gaining enough energy to move from the electrode in the conduction band of the insulator.

- Poole-Frenkel emission: In insulators, electrons are stuck in traps. Under high electric fields, the energy barrier of the trap is lowered enough that the electron can jump to the next trap.
- Fowler-Nordheim tunneling: In thin insulators with high electric fields, electrons can quantum mechanically tunnel across a triangular energy barrier into the conduction band of the insulator.

### 1.2.1 Metal Ions: Butler-Volmer Equation for Electrode Redox

The process occurring at the electrodes during the write, before the filament bridges the gap, and during the erase is an electrochemical reaction. During the write process, there is silver oxidation from the anode and deposition onto the cathode. During the erase, there is silver oxidation from the filament and cathode and reduction to the anode. These processes have been characterized with well-known electrochemistry equations that have been used for many electrode applications, such as batteries.

Equation 1.3 is the Butler-Volmer equation, which describes the current when there is anodic oxidation and cathodic reduction [15].

$$I = I_0 \left[ \frac{C_o(0,t)}{C_o^*} \exp\left(\frac{\alpha\eta}{kT/q}\right) - \frac{C_r(0,t)}{C_r^*} \exp\left(-\frac{(1-\alpha)\eta}{kT/q}\right) \right] \quad (1.3)$$

where  $I_0$  is the exchange current, defined as the current from either electrode at equilibrium when the net current flow is zero, and  $\alpha$  is a 0-1.0 fitting parameter called the transfer coefficient.  $\eta$  is the overpotential defined as the potential difference between the zero current equilibrium potential and the applied potential. For a device such as a battery, the zero current equilibrium potential is the voltage of the battery. Since the CBRAM device has no current at zero applied potential, the overpotential is equal to the

applied potential across the device.  $q$  is the charge of the ion. For the case of  $\text{Ag}^+$ , it is the elementary charge multiplied by one.  $\frac{C_o(0,t)}{C_o^*}$  and  $\frac{C_r(0,t)}{C_r^*}$  are the relative surface to bulk concentrations at the anode and cathode at a moment in time. The concentration ratio is especially important for the erase, since the concentration of oxidizable material from the filament and cathode goes to zero over time. The first exponential term is the cathode current. The second exponential term is the anode current. The individual cathode current,  $i_c$ , and the individual anode current,  $-i_a$ , are shown in dotted lines in the typical Butler-Volmer current-overpotential plot in Figure 1.8 [15].

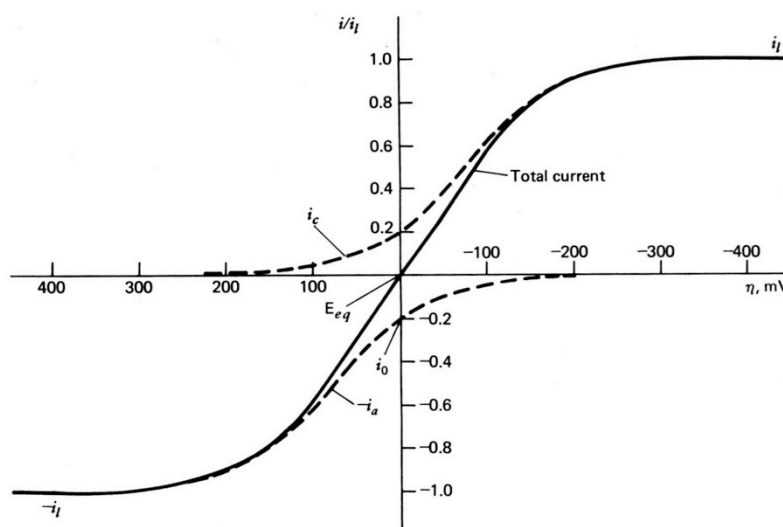


**Figure 1.8** Butler-Volmer current-overpotential curve showing cathode and anode current ( $i_c$  and  $i_a$ ) [15].

Qualitatively, the applied voltage (overpotential) serves as activation to lower the barriers to oxidation and reduction. If the exchange current is low, the kinetics are sluggish and require a higher activation potential.

If the overpotential is large, then the reaction at one of the electrodes dominates, and the equation simplifies to the Tafel equation [15], shown in Eqn. 1.4. Using the Tafel

equation, it is possible to experimentally determine the exchange current  $I_0$  and the transfer coefficient  $\alpha$ .

$$\ln I = \frac{\alpha}{kT/q} \eta + \ln I_0 \quad (1.4)$$

If the overpotential is small, then the Butler-Volmer equation approaches a linear current-potential relationship shown in Eqn. 1.5 [15]. This means that for low applied potential the current response appears ohmic. The temperature response of the low field Butler-Volmer approximation predicts that as temperature is increased, conductance goes down.

$$I = \frac{I_0}{kT/q} \cdot \eta \quad (1.5)$$

### 1.2.2 Metal Ions: Mott-Gurney Hopping

The ion-transfer process is governed by Mott-Gurney hopping [16]. The ion current density-electric field equation for ion hopping is shown in Eqn. 1.6.

$$J = 2qCav \cdot \exp\left(-\frac{W_a^0}{kT/q}\right) \cdot \sinh\left(\frac{aE}{2kT/q}\right) \quad (1.6)$$

The equation consists of the hopping distance  $a$ , the concentration of mobile cations  $C$ , the hopping rate  $v$ , and the energy barrier  $W_a^0$ . At high electric fields, the hyperbolic sine tends to an exponential, as shown in Eqn. 1.7 [10].

$$J = 2qCav \cdot \exp\left(-\frac{W_a^0}{kT/q}\right) \cdot \exp\left(\frac{aE}{2kT/q}\right) \quad (1.7)$$

At low electric fields, the equation simplifies to a linear dependence on the electric field, as shown in Eqn. 1.8 [10].

$$J = \frac{qCa^2v}{kT/q} \cdot E \cdot \exp\left(-\frac{W_a^0}{kT/q}\right) \quad (1.8)$$

### 1.2.3 Alternate Theory to Mott-Gurney Ion Hopping: Electron Tunneling Between Adjacent Impurity Sites

For a system where Au is electrolytically introduced into resistive SiO, a resistive memory effect was demonstrated by Simmons and Verderber in 1967 [17]. To explain conduction in the system of Au/SiO/Al, Simmons and Verderber theorized that electrons are tunneling between adjacent Au impurity sites. For low electric fields in the Au/SiO/Al system, it was found that current obeys the expression shown in Eqn. 1.9, where  $K$  and  $k$  are constants.

$$I = K \sinh kV \quad (1.9)$$

What is immediately noticed is that the equation produced by Simmons and Verderber has the same form as the Mott-Gurney hopping equation, where electric field or voltage is included in a hyperbolic sine term. The analysis performed in this work is not able to distinguish between these two proposed mechanisms.

### 1.2.4 Electrons: Schottky Thermionic Emission

With high electric fields, it is possible for electrons to surpass the energy barrier of the electrode and enter the conduction band of the insulator [18]. Schottky emission is a thermally dependent process.

The Schottky equation for thermionic emission in terms of current density and electric field is shown in Eqn. 1.10.

$$J = A^* T^2 \exp \left[ \frac{-q(\phi_B - \sqrt{qE/4\pi\epsilon_i})}{kT} \right] \quad (1.10)$$

Constants:  $A^*$  is the effective Richardson constant,  $q$  is the elementary charge,  $\epsilon_i$  is the insulator permittivity,  $\phi_B$  is the Schottky barrier height, and  $k$  is the Boltzmann

constant. The effective Richardson constant is a function of the effective electron mass and is given by Eqn. 1.11 below.

$$A^* = \frac{4\pi m^* k^2 q}{h^3} \quad (1.11)$$

Constants from Richardson's constant equation:  $m^*$  is the electron effective mass and  $h$  is Planck's constant.

To determine if the Schottky thermionic emission conduction mechanism is active, Schottky plots ( $\ln I$  vs.  $\sqrt{V}$ ) must be generated for each temperature. If the Schottky plot has a linear region, there is a chance that Schottky thermionic emission is active. In that case, additional calculations are necessary.

Linear equation fitting must be performed on the Schottky plots. Results are in the form  $a + bx$ . Solving the Schottky equation for  $a$  and  $b$  results in Eqns. 1.12 and 1.13.

$$a = -\frac{q\phi_B}{kT} + \ln(A^* \cdot T^2 \cdot area) \quad (1.12)$$

$$b = \frac{q}{kT} \sqrt{\frac{q}{4\pi\epsilon_i \cdot thickness}} \quad (1.13)$$

The slope,  $b$ , enables the determination of the permittivity,  $\epsilon_i$ . Permittivity is known to vary with temperature [19]. By plotting the y-intercept,  $a$ , across temperatures, it may be possible to find the Schottky barrier height  $\phi_B$ . It helps if the electron effective mass is known.

### 1.2.5 Electrons: Band Conduction in the Extended States

For temperatures near room temperature, it is believed that electron conduction in amorphous chalcogenides occurs as band conduction in the extended states [20]. The

energy band diagram in Figure 1.9 shows the difference between the extended states and the localized states [20].

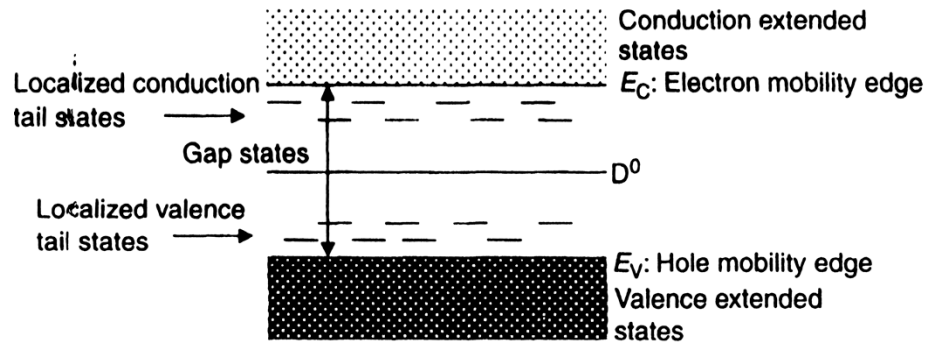


**Figure 1.9** Energy band diagram of an amorphous semiconductor [20].

The equation for band conduction in the extended states has an Arrhenius form. This is shown in Eqn. 1.14, where  $\Delta E$  is the activation energy defined as  $E_C - E_F$ , the separation between the Fermi level and electron mobility edge. The parameter  $\sigma$  is conductivity, and  $\sigma_0$  is a constant.

$$\sigma = \sigma_0 \exp(-\Delta E/kT) \quad (1.14)$$

### 1.2.6 Electrons: Mott's $T^{1/4}$ Variable Range Hopping

At low temperatures, there are fewer carriers in the conduction extended states due to the reduced thermal energy in the system. At that point, hopping conduction between localized states and in gap states may dominate. Hopping means that localized electrons jump quantum mechanically from site to site. The reason the mechanism is called Variable Range Hopping is because there is a hopping distance where the hopping rate is maximized [20]. When this is true, the conductance follows Eqn. 1.15, where  $T_0$  is a constant.

$$\sigma_{DC} = \sigma_0 \exp[-(T_0/T)^{1/4}] \quad (1.15)$$

To determine if Variable Range Hopping (VRH) is occurring, a plot must be generated of  $\ln(\sigma)$  vs  $T^{-1/4}$ . If there is a linear fit, it is likely that the VRH mechanism is occurring.

### 1.2.7 Electrons: Poole-Frenkel Emission

The Poole-Frenkel emission theory was first presented by Frenkel in 1938 [21]. The theory claims that when a high electric field is applied to an insulator, a barrier lowering takes place. The atom containing the trapped electron is ionized, and the electron is free to move. Poole-Frenkel emission follows Eqn. 1.16.

$$J = CE \exp \left[ \frac{-(\phi_B - \sqrt{qE/\pi\epsilon_i})}{kT/q} \right] \quad (1.16)$$

C is a constant. The other variables are the same as mentioned in the Schottky emission section. The Poole-Frenkel equation is very similar to the Schottky emission equation with the exceptions of the pre-exponential factor being proportional to electric field instead of the square of temperature and the multiplier for the permittivity does not have the factor of 4.

To determine if the Poole-Frenkel emission mechanism is in effect, a Poole-Frenkel plot must be constructed. The y-axis is  $\ln(I/V)$  and the x-axis is  $\sqrt{V}$ . If the result is linear, it is possible that the Poole-Frenkel mechanism is in effect.

Next, the fitting coefficients must be investigated. Results are in the form  $a + bx$ . Solving the Poole-Frenkel equation for  $a$  and  $b$  gives Eqns. 1.17 and 1.18.

$$a = \frac{-q\phi_B}{kT} + \ln \left( \frac{C \cdot \text{area}}{\text{thickness}} \right) \quad (1.17)$$

$$b = \frac{q}{kT} \sqrt{\frac{q}{\pi\epsilon_i \cdot \text{thickness}}} \quad (1.18)$$

Similarly to the Schottky emission mechanism, the Poole-Frenkel slope can determine the permittivity. Also similar to the Schottky equation, the Poole-Frenkel y-intercept can determine the barrier height.

### 1.2.8 Electrons: Fowler-Nordheim Tunneling

For thin insulators with applied electric field, carriers can quantum mechanically tunnel across forbidden energy states into the insulator conduction band. The Fowler-Nordheim case is the tunneling across a triangular barrier [22]. The energy band diagram of FNT for a metal-oxide-semiconductor (MOS) structure is shown in Figure 1.10.

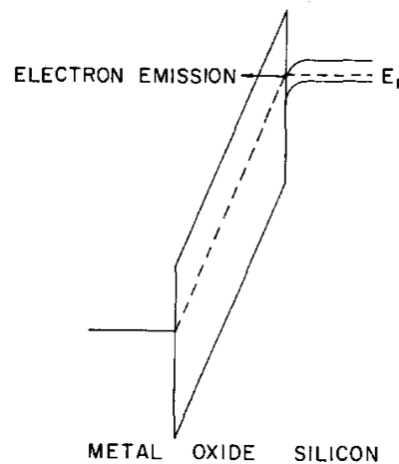


**Figure 1.10** Energy band diagram of a MOS structure with large applied positive voltage showing Fowler-Nordheim Tunneling.

A typical equation used for FNT current is given in Eqn. 1.19. It takes into account the effective mass of electrons in the insulator and allows for a different electron effective mass in the electrode [23]. For this work, the electron mass in the tungsten electrodes is assumed to be at vacuum mass.

$$J = \frac{q^3 m_e}{8\pi h m_{diel}^* \phi_B} E^2 \exp \left[ \frac{4(2m_{diel}^* \phi_B^3)^{1/2}}{3q\hbar E} \right] \quad (1.19)$$

As seen in the FNT equation, Fowler-Nordheim tunneling does not depend on temperature. However, at lower temperatures, there may be fewer electrons incident on the barrier [22]. This reduces the conduction at low temperatures.

To determine if Fowler-Nordheim tunneling is present, a Fowler-Nordheim plot of the I-V traces must be generated. The y-axis is  $\ln(I/V^2)$ , and the x-axis is  $V^{-1}$ . A good linear fit indicates Fowler-Nordheim tunneling may be present.

### 1.3 Device Structure

To investigate the conduction mechanisms in silver ion-conducting devices, devices without silver were tested to understand which mechanisms which electron conduction mechanisms might be occurring in the amorphous chalcogenide memory layer. The electron conduction of the resistive memory layer is especially important when the silver ion-conducting device is in its erased state.

Two types of silver conducting devices were tested. One structure uses silver to form the filament across a  $\text{Ge}_{32}\text{Se}_{68}$  memory layer. The second structure has a silver and a tin selenide layer above the  $\text{Ge}_{32}\text{Se}_{68}$  memory layer.

#### 1.3.1 Structure of Resistive $\text{Ge}_{32}\text{Se}_{68}$ Test Devices

A cross-sectional diagram of the 300 Å device is shown in Figure 1.11. The purpose of this simple device is to form a clear understanding of the electron-conduction mechanisms that are occurring in the chalcogenide memory layer.

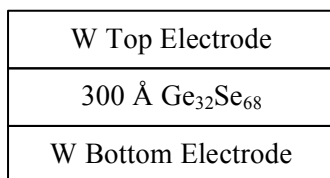


**Figure 1.11** Cross-sectional diagram of resistive memory layer test device with 300 Å  $\text{Ge}_{32}\text{Se}_{68}$ .

### 1.3.2 Structure of Silver Ion-Conducting Devices

Of the two Ag-conducting devices tested, the simpler one uses silver only. The more complex stack device uses Ag and SnSe. The cross-sectional diagram of the simpler Ag-only ion-conducting device is shown in Figure 1.12. It consists of a W top electrode, a 100 Å  $\text{Ge}_{32}\text{Se}_{68}$  metal adhesion layer, 500 Å Ag to provide silver ions for conduction across the memory layer, 300 Å  $\text{Ge}_{32}\text{Se}_{68}$  memory layer, and W bottom electrode.

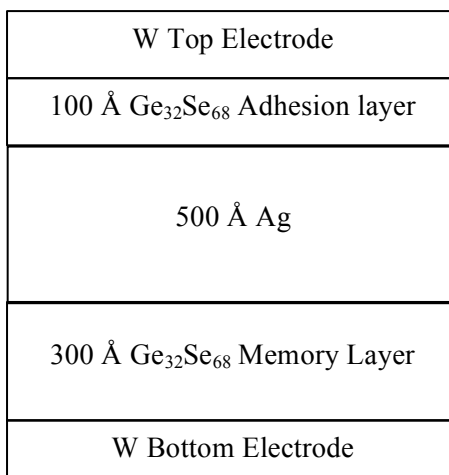


**Figure 1.12** Cross-sectional diagram of silver-only ion-conducting test device.

The second ion-conducting device tested is the Ag+SnSe. Instead of only Ag, the presence of Sn may alter the ion motion. The cross-sectional diagram is shown in Figure 1.13.

W Top Electrode
100 Å $\text{Ge}_{32}\text{Se}_{68}$
500 Å Ag
150 Å $\text{Ge}_{32}\text{Se}_{68}$
700 Å SnSe
300 Å $\text{Ge}_{32}\text{Se}_{68}$ Memory Layer
W Bottom Electrode

**Figure 1.13** Cross-sectional diagram of the Ag and SnSe ion-conducting device.

## CHAPTER 2: EXPERIMENTAL

### 2.1 Introduction

This chapter describes how devices were fabricated and describes the equipment and software that was used to perform testing on the  $\text{Ge}_{32}\text{Se}_{68}$  devices, the Ag-only switching devices, and the Ag+SnSe devices. Also, the procedures used to gather measurements are detailed. The particular IV curve transformations are described for the electron-conduction mechanisms for  $\text{Ge}_{32}\text{Se}_{68}$  and the ion-conduction mechanisms for the Ag-only and Ag+SnSe switching devices.

### 2.2 Device Fabrication

The three devices tested in this work were fabricated in Boise State University's Idaho Microfabrication Laboratory by members of Dr. Kris Campbell's research group. They are: 1) the 300 Å  $\text{Ge}_{32}\text{Se}_{68}$  devices, 2) the Ag on  $\text{Ge}_{32}\text{Se}_{68}$ , and 3) the Ag on SnSe/ $\text{Ge}_{32}\text{Se}_{68}$  devices. This section outlines the processing that was performed.

#### 2.2.1 Device Fabrication

The substrate used was prefabricated with 800 Å  $\text{Si}_3\text{N}_4$  on 600 Å W on 250 Å Cr on Si <100>. The W and Cr underlayers were used for the bottom electrode. All photolithography was performed using the Quintel Q4000 contact aligner.

Processing sequence:

1. To start the process, vias were etched out of the nitride using the reactive ion etcher Oxford Plasmalab 100 RIE.

2. An argon bias clean at 30W for one minute was performed in the AJA RF magnetron sputter tool to clean the bottom electrode prior to chalcogenide deposition.
3. The chalcogenide, Ag, and W were sputtered using the AJA RF magnetron sputter tool. Additional notes and exceptions:
  - a. In the case of the  $\text{Ge}_{32}\text{Se}_{68}$ -only devices, Ag was not used.
  - b. In the case of the Ag+SnSe stack device, after chalcogenide sputtering, SnSe was evaporated. Then, wafers returned to the AJA sputter tool for Ag and W.
4. The chalcogenide/top electrode stack was etched using the Veeco ME 1001 Ion Beam etcher to define the devices.

## **2.3 Test Equipment and Software Used**

### **2.3.1 Low Temperature Probe Station**

Electrical IV measurements were performed using the LakeShore CRX-4K Probe Station, a closed-cycle refrigerator probe station shown in Figure 2.1. It has a vacuum chamber containing a cooled radiation shield that surrounds the cooled sample stage, a Sumitomo SRDK Series cryocooler system, and two LakeShore Model 340 temperature controllers. The chamber is pumped down using a turbomolecular pump from Varian.

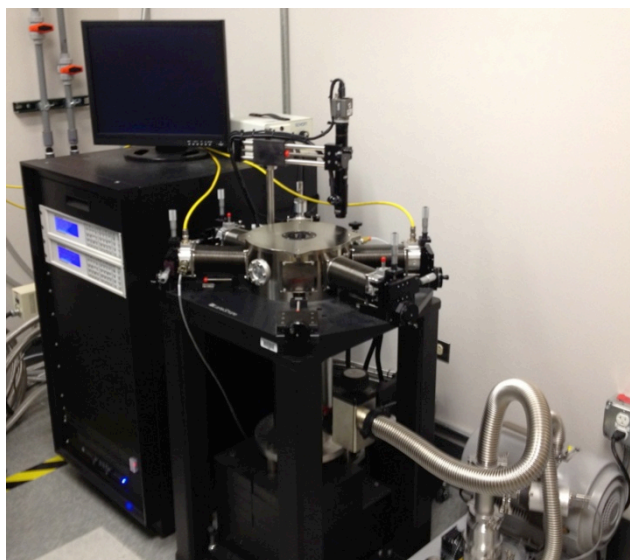


**Figure 2.1 LakeShore CRX-4K Probe Station.**

The sample stage is in the center of the vacuum chamber. There is a resistive heating element under the sample stage for temperature control. A view of the loaded sample stage is shown in Figure 2.2.

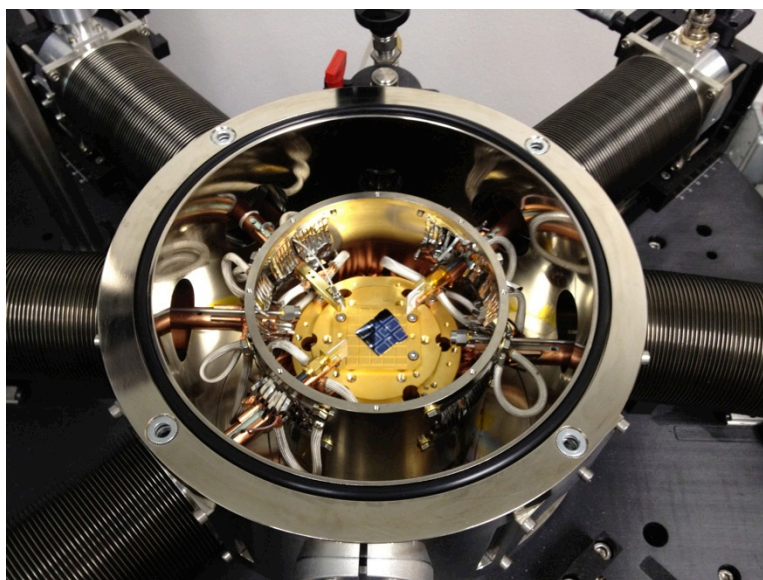


**Figure 2.2 View of interior of vacuum chamber with sample stage exposed.**

The system is capable of controlling temperature from 6.5 K to 350 K. The LakeShore model 340 temperature controllers are shown in Figure 2.3. Each controller

has two control loops. The sample stage, radiation shield, cryocooler first stage, and cryocooler second stage have heaters that can be controlled. In addition, there is a temperature readout for the probe temperature. During measurements, only the sample stage heater is used. All others remain at base temperature.



**Figure 2.3 LakeShore Model 340 temperature controllers.**

The refrigerator is a Sumitomo SRDK Series cryocooler with F-50 Series compressor unit. It operates on the GM (Gifford-McMahon) cycle. It consists of a water-cooled compressor unit, high-pressure helium supply lines, and cold head. The compressor unit is shown in Figure 2.4.



**Figure 2.4 Sumitomo F-50 Cryocooler compressor unit.**

The compressor consists of a compressor capsule, a cooling system, and a lubricating oil mist adsorber. It provides power to the cooling head. The high-pressure helium supply lines are shown in Figure 2.5.

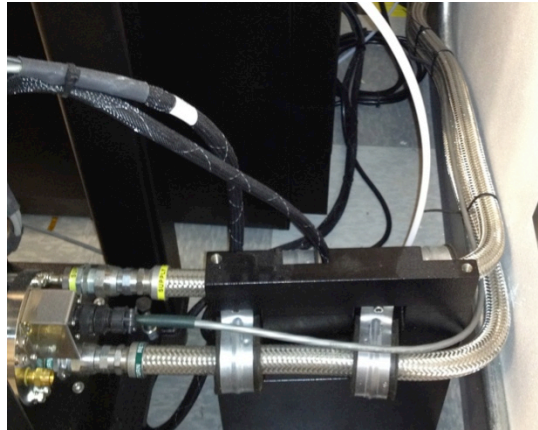


**Figure 2.5 Sumitomo SRDK Series cryocooler system – high-pressure helium supply lines.**

The cold head is shown in Figure 2.6. The cold head consists of a displacer-regenerator assembly and motor housing containing a crankcase. The high-pressure helium gas enters the displacer-regenerator assembly, then into the crankcase, back to the displacer-regenerator assembly and out to the helium return line and the compressor. The helium gas expansion in the displacer-regenerator assembly provides cooling for the system.

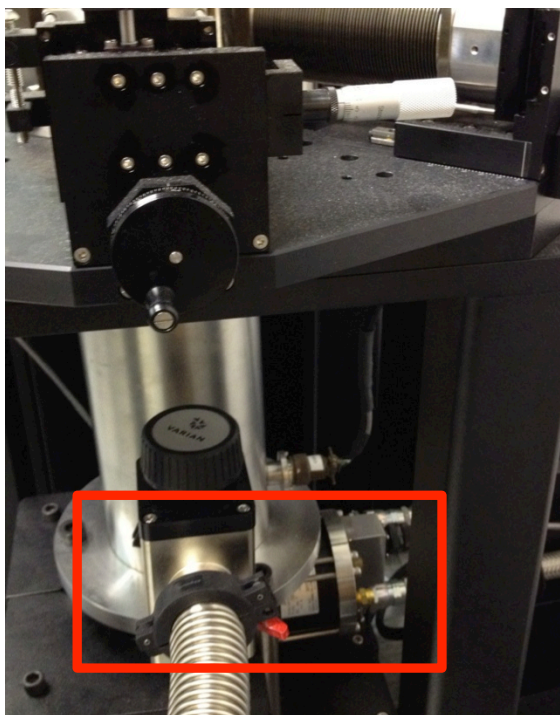


**Figure 2.6** Sumitomo SRDK Series cryocooler system – cold head.

### 2.3.2 Probes

The electrical probes used for device measurement were LakeShore model ZN50R-25-W, shown in Figure 2.7. They have a 25  $\mu\text{m}$  tip radius and are made of tungsten. The ZN50 probe base incorporates a pair of copper braids that anchor to the sample stage to dynamically cool/heat the probe to the sample temperature.

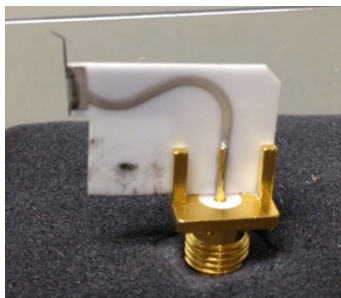


**Figure 2.7** LakeShore ZN50R-25-W probe.

### 2.3.3 HP 4156A Semiconductor Parameter Analyzer

Current-voltage traces were generated using the HP 4156A Semiconductor Parameter Analyzer. The current resolution is 1 fA, and the current offset accuracy is 20 fA. It has 4 built in SMUs (source measurement units) that are capable of simultaneously sourcing and measuring voltage or current [24].

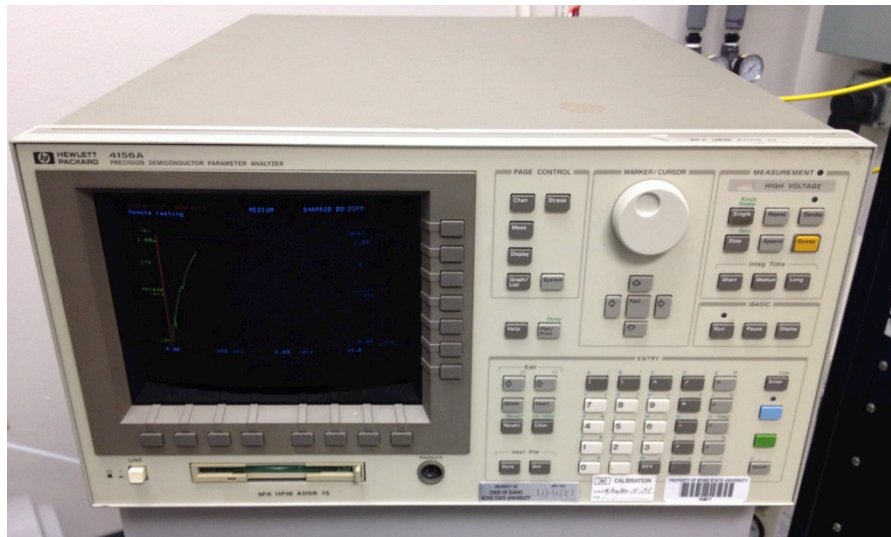


**Figure 2.8 HP 4156A Semiconductor parameter analyzer.**

### 2.3.4 Triaxial Cables

The cabling choice is important. Triaxial cables have an extra layer of shielding compared to coaxial cables. An illustration and graph are shown in Figure 2.9 [25]. The guard and force are kept at the same potential to mitigate RC charging and leakage effects on the force electrode. For measurements of currents below 1 nA, the capacitance of the standard coaxial cable adds significant RC charging current, causing errors in low current measurements [25].

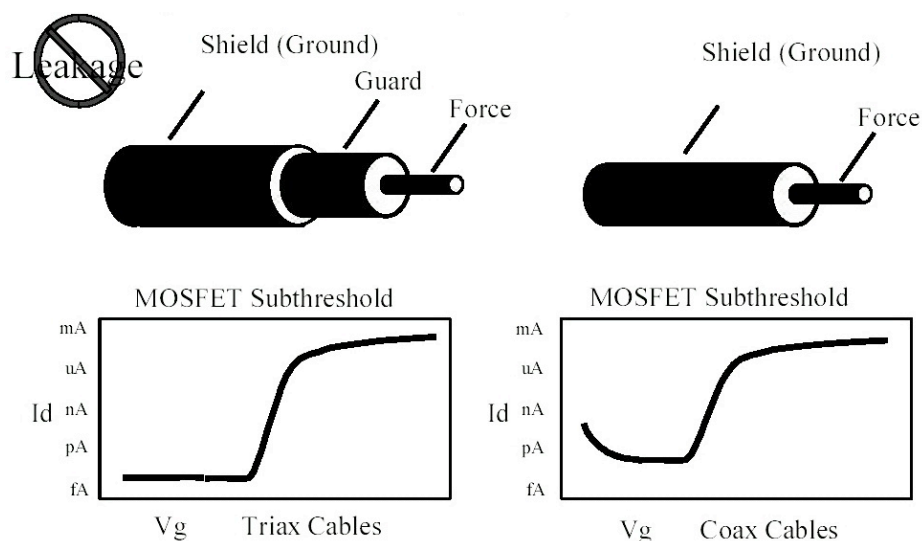


**Figure 2.9 Illustration of importance of triaxial cabling for low current measurements.**

### 2.3.5 Semiconductor Parameter Analyzer Control Software - MCP2

The HP 4156A was controlled using a Labview-based software called MCP2, which was provided by Micron Technology. It communicates with the 4156A with a USB/GPIB interface cable. The software was used to generate voltage sweeps stopping at a compliance current. It saves the data in an Excel file. It is capable of performing multiple measurements in a sequence.

## 2.4 Testing Procedures

### 2.4.1 General Low Temperature Testing Procedure

For the voltage sweeps performed across temperatures in this work, the tests were started at room temperature. The stage heater setpoint was stepped down to the next lowest temperature. Temperatures were allowed to stabilize for at least 30-45 minutes. The reason to start at room temperature was to save time, since the refrigerator takes hours to cool down to base temperature from room temperature.

The procedure to perform the testing is to load wafer pieces onto the stage. Then, open circuit and short circuit tests are performed. The vacuum chamber is sealed, and the turbomolecular vacuum pump is turned on. After the chamber reaches an intermediate pressure of  $1 \times 10^{-3}$  mbar, the refrigerator is turned on. The sample stage heater is set to 300 K, allowing room temperature measurements to start while the refrigerator is cooling. Keeping the stage heater warm during initial cool-down prevents damaging, frozen condensation. Once the radiation shield reaches 100 K, the sample stage heater setpoint can be reduced without the risk of condensation.

#### 2.4.2 Die Layout

The die is organized into columns containing devices of the same size. Rows have different electrode pad sizes. The pad size difference has limited impact to the test since the DC sweeps are very slow. The testing focused on devices sized 3  $\mu\text{m}$  in diameter that were known to have better fabrication consistency. A microscope image of a die is shown in Figure 2.10.

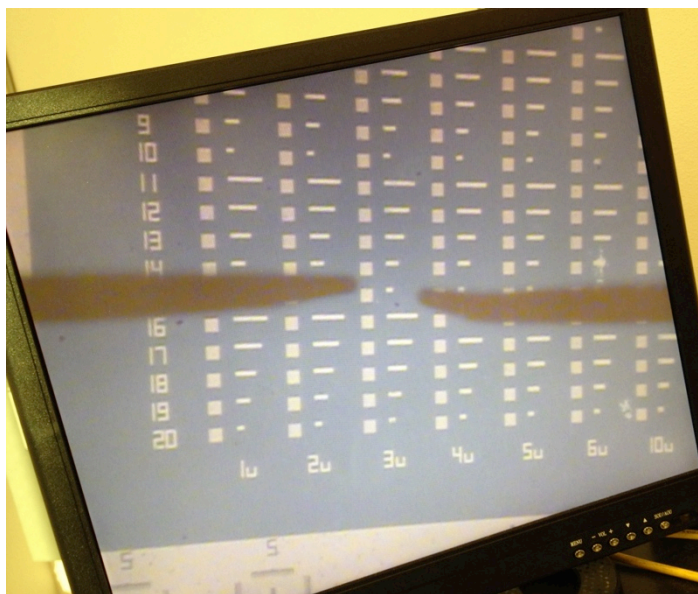


**Figure 2.10 Die layout example showing device arrangement.**

#### 2.4.3 Testing of 300 Å Ge<sub>32</sub>Se<sub>68</sub>

To test the 300 Å Ge<sub>32</sub>Se<sub>68</sub> devices, a compliance current limit of 1 nA was used to prevent device breakdown, which can occur with higher currents. To perform the test, the top electrode was used to force voltage and the bottom electrode was grounded. The top electrode voltage was swept from 0 V to 5 V. If the 1 nA compliance current was reached, the measurement was stopped at the voltage at which compliance was reached.

During testing, it was found that there was a large variation in performance between devices. To help eliminate the variation from consideration, six devices were retested at each temperature. Temperatures ranging from 300 K down to 10 K were used.

#### 2.4.4 Testing of Ag-Only and Ag+SnSe Devices

For each of the device types, three devices were retested at each temperature and three fresh, previously untested devices were used. All devices were sized 3 μm in diameter, programmed with a 50 μA compliance current. The purpose of retesting

devices was to remove process variation from the analysis. Fresh devices were used to help remove repeatability variation from the analysis.

## 2.5 Data Analysis Procedures

Current-voltage traces were gathered for each device variety. The data was then transformed using equations for known electron-conduction mechanisms in the case of  $\text{Ge}_{32}\text{Se}_{68}$  devices and for known ion-conduction mechanisms in the case of the Ag-only and Ag+SnSe switching devices.

The electron-conduction mechanisms tested were: Schottky emission, Poole-Frenkel emission, Fowler-Nordheim tunneling, band conduction in extended states, and Mott's  $T^{1/4}$  variable range hopping.

### 2.5.1 $\text{Ge}_{32}\text{Se}_{68}$ Devices – Electron Conduction

Current-voltage traces from the  $\text{Ge}_{32}\text{Se}_{68}$  devices were gathered and presented. The traces were transformed using the appropriate equation for the electron-conduction mechanism under investigation. The reason for transforming the data is to perform a line fit. If the transformed data appears to fit to the mechanism, then the slope and y-intercept are used to calculate any material or electrical properties from the mechanism equation. Those calculated properties can help to validate if the mechanism is occurring. A summary of the transformations performed is shown in Table 2.1.

**Table 2.1 Summary of Transformations Performed on IV Traces of Resistive 300 Å Ge<sub>32</sub>Se<sub>68</sub> Devices to Determine Conduction Mechanism**

<b>Mechanism</b>	<b>Transformation</b>	<b>Action</b>
Schottky Thermionic Emission	$\ln(I)$ vs $\sqrt{V}$	Fit line. Extract coefficients. Calculate material and electrical properties across multiple temperatures.
Poole-Frenkel Emission	$\ln(I/V)$ vs $\sqrt{V}$	
Fowler-Nordheim Tunneling	$\ln(I/V^2)$ vs $1/V$	
Band conduction in the extended states	$\ln(\sigma)$ vs $1/T$	Calculate conductivity at a specified voltage for each temperature. Fit line.
Mott's $T^{1/4}$ Variable Range Hopping	$\ln(\sigma)$ vs $T^{-1/4}$	

### 2.5.2 Ag-Only and Ag+SnSe Devices.

For the switching devices, several parameters of interest are collected. A summary of which parameters were collected is given in Table 2.2.

**Table 2.2 Summary of Parameters Collected from Ion-Conducting Switching Devices**

<b>Parameter</b>	<b>Method to determine</b>
Pre-write resistance	Linear fit to 20 mV sweep
Write $V_T$	The voltage when writing compliance current is achieved
Write curve: high applied potential (before write threshold)	Capture exponential to perform transformations using the Mott-Gurney ion hopping Arrhenius form and the Tafel electrode redox Arrhenius form.
Post Write Resistance	Linear fit to 20 mV sweep.
Erase Curve	Shows erase performance.
Post Erase Resistance	Verify that the device did erase.

Transformations to the write curves are required to characterize the Mott-Gurney ion hopping and the Butler-Volmer electrode redox current. The transformations for each mechanism are summarized in Table 2.3.

**Table 2.3 Summary of Ion-Conduction Mechanism Transformations Performed on the Write Traces of Ion-Conducting Switching Devices**

<b>Mechanism</b>	<b>Transformation</b>	<b>Action</b>
High Field Mott-Gurney ion hopping	Plot $\ln(I)$ vs $V$	Slope determines hopping distance. Y-intercept can be used to determine activation energy.
High Field Tafel electrode redox	Plot $\ln(I)$ vs $V$	Slope determines transfer coefficient, $\alpha$ .

For Mott-Gurney high field ion hopping, the  $\ln(I)$  vs  $V$  transformation results in hopping distance,  $a$ , shown in Eqn. 2.1.

$$a = 2b \cdot \text{thickness} \cdot kT/q \quad (2.1)$$

$b$  is the slope of the  $\ln(I)$  vs  $V$  linear portion.

The MG high field activation energy can be determined by plotting the y-intercept ( $a$ ) across temperatures and determining the slope, as shown in Eqn. 2.2. The constant,  $C$ , in the equation is equal to  $\ln(\text{area} \cdot 2qCav)$ , containing device area, ion concentration, jump distance, and hopping rate.

$$a = C - \frac{W_a^0}{k/q} \cdot \frac{1}{T} \quad (2.2)$$

For the high field Butler-Volmer electrode redox equation (Tafel) [15], the transformed version is shown in Eqn. 2.3. It is clear that the slope determines the transfer coefficient,  $\alpha$ , and the y-intercept determines the exchange current,  $I_0$ .

$$\ln(I) = \frac{\alpha}{kT/q} V + \ln(I_0) \quad (2.3)$$

## 2.6 Experimental Summary

In this chapter, the equipment, testing procedures, and data analysis methods have been outlined. In the next chapters, analysis results are presented for the resistive chalcogenide  $\text{Ge}_{32}\text{Se}_{68}$  devices, the Ag-only switching devices, and the Ag+SnSe devices.

## CHAPTER 3: CONDUCTION MECHANISMS OF 300 Å Ge<sub>32</sub>Se<sub>68</sub>

### 3.1 Introduction

Current-voltage sweeps were performed on six adjacent devices sized 3 μm in diameter with 300 Å Ge<sub>32</sub>Se<sub>68</sub> sandwiched between W electrodes across temperatures. To limit the impact of process variations, the same devices were retested rather than using separate devices for each temperature measurement. It was imperative not to induce breakdown during the test, so current was capped at 1 nA compliance with a maximum voltage of 5 V. For each measurement, the temperature was allowed to stabilize for at least 45 minutes.

To verify if device performance is repeatable enough to measure the same device over and over, one device was cycled 20 times at room temp (300 K). The result is shown in Figure 3.1. While there appears to be some variation in the magnitude of the current at a given voltage, there isn't a trend in magnitude based on measurement number. The exponential slope of the curves appears to be approximately the same. Based on this result, it was concluded that measuring the same device multiple times is a reasonable way to trend device performance across temperatures.

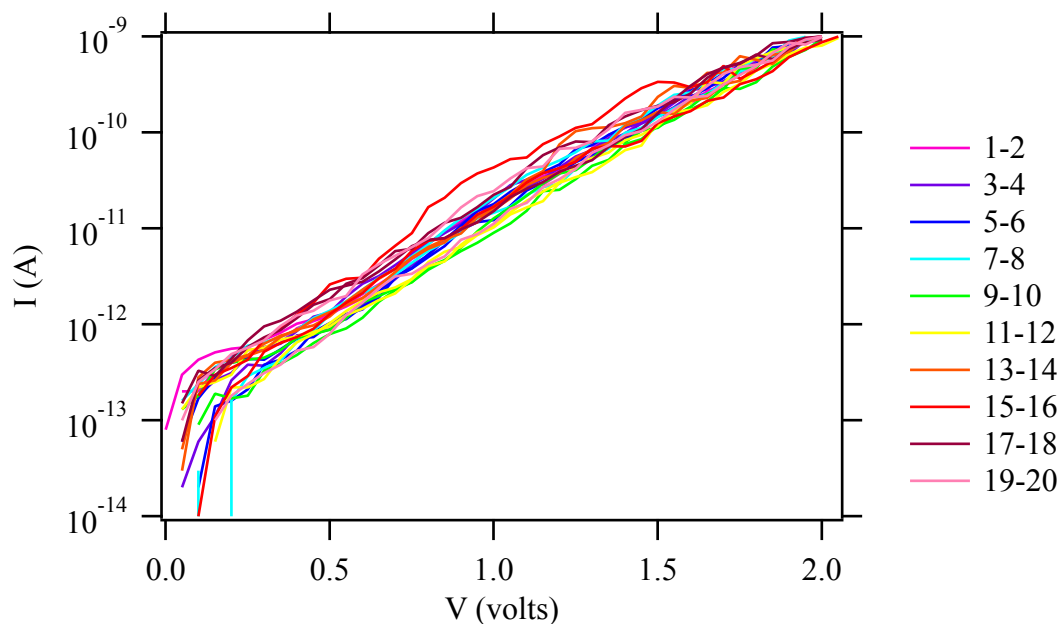


**Figure 3.1** Current-voltage traces of 300 Å  $\text{Ge}_{32}\text{Se}_{68}$  resistive memory layer device cycled 20 times.

### 3.2 IV Traces

To illustrate how the devices perform across temperatures and to get a qualitative view of the process variation, the IV traces from each of the six devices are shown and described in this section. The voltage was swept from 0 V to 5 V. The measurement was stopped at the voltage reached when the 1 nA compliance current was achieved.

#### 3.2.1 IV Traces – 1<sup>st</sup> Device

In Figure 3.2, the IV traces for the first device are shown. The general trend is that for higher temperatures, the conduction is higher, which is a common feature to all conduction mechanisms under investigation.

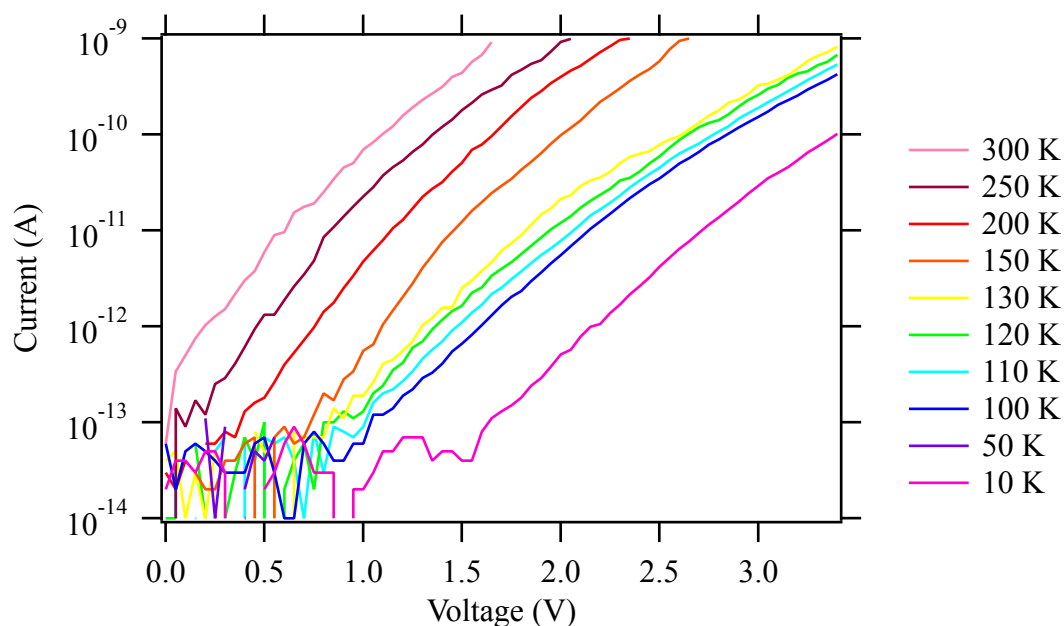


**Figure 3.2** IV Traces of first 300 Å  $\text{Ge}_{32}\text{Se}_{68}$  device from 10 K to 300 K.

### 3.2.2 IV Traces – 2<sup>nd</sup> Device

In Figure 3.3, current-voltage traces are shown for the second 300 Å  $\text{Ge}_{32}\text{Se}_{68}$  device for temperatures from 10 K to 300 K. The expected general trend of higher conduction for higher temperatures is present. Qualitatively, the temperatures between 300 K and 150 K have consistent changes in conduction. Below 150 K, the consistent performance ends. The conduction at 100 K appears to be similar to the conduction at 150 K. This suggests a shift in the conduction mechanism below 150 K.

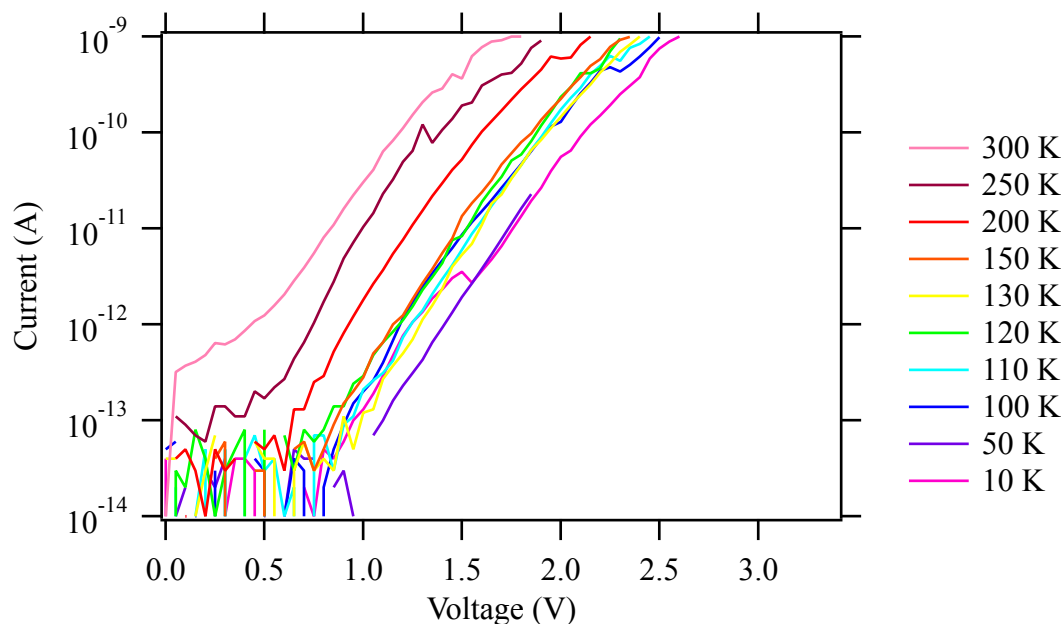


**Figure 3.3** IV Traces of second 300 Å Ge<sub>32</sub>Se<sub>68</sub> device from 10 K to 300 K.

### 3.2.3 IV Traces – 3<sup>rd</sup> Device

The current-voltage traces for the third 300 Å Ge<sub>32</sub>Se<sub>68</sub> device are shown in Figure 3.4. As in the first two devices, there is a general trend in conductivity reduction with decreasing temperature. Traces appear to be spaced closer than the previous devices, suggesting a smaller dependence on temperature. Many of the traces overlap each other. There is more noise compared to the first two devices.

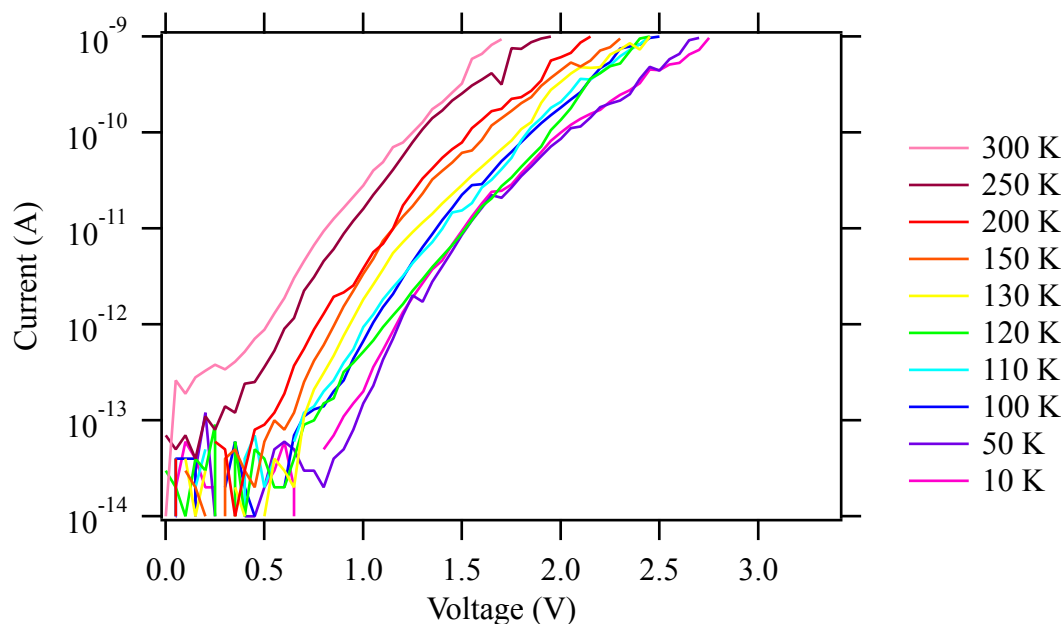


**Figure 3.4** IV Traces of third 300 Å  $\text{Ge}_{32}\text{Se}_{68}$  device from 10 K to 300 K.

#### 3.2.4 IV Traces – 4<sup>th</sup> Device

Current-voltage traces from 10 K to 300 K for the fourth 300 Å  $\text{Ge}_{32}\text{Se}_{68}$  device are shown in Figure 3.5. Again, the general trend of higher conduction for higher temperatures is present. There are overlapping traces below 200 K for this device. From 200 K to 120 K, the traces are very close to each other, overlapping in some cases.

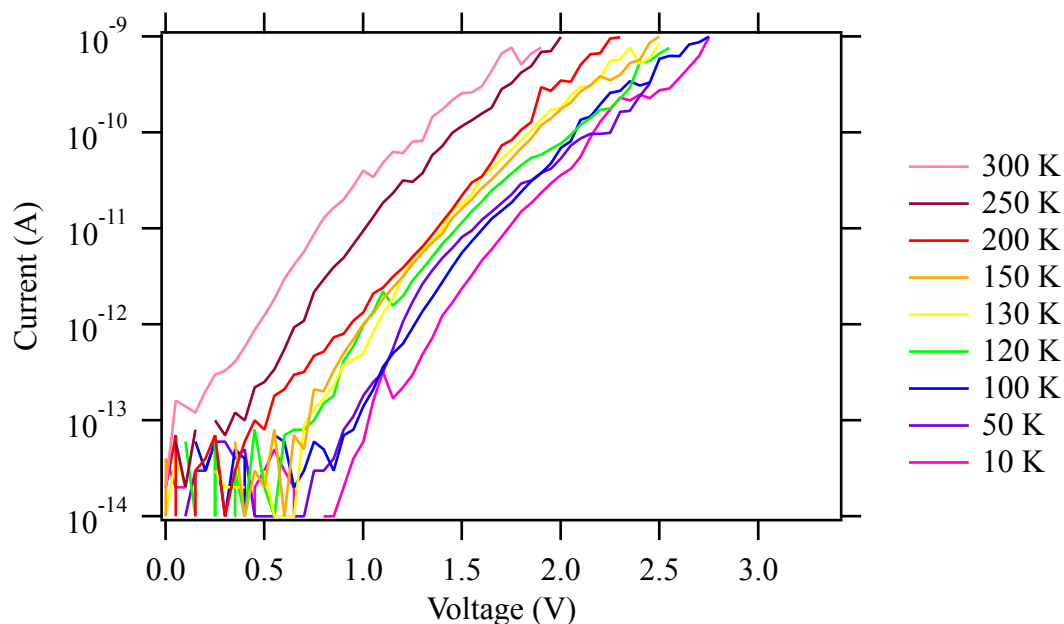


**Figure 3.5** IV Traces of fourth 300 Å  $\text{Ge}_{32}\text{Se}_{68}$  device from 10 K to 300 K.

### 3.2.5 IV Traces – 5<sup>th</sup> Device

Current-voltage traces from 10 K to 300 K are shown in Figure 3.6. The general trend of higher conduction for higher temperatures is present for this device. To qualitatively compare the performance of this device with the others – the slopes are very consistent. There aren't any overlapping traces. The noise level appears to be lower. The slope did not have a large shift below 150 K as occurred in the first device.

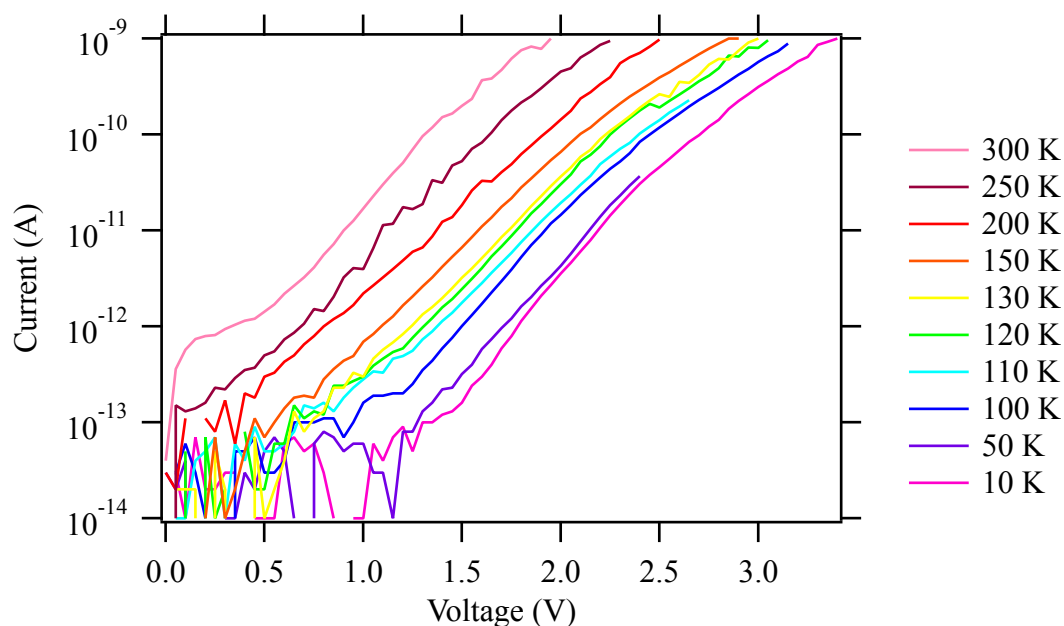


**Figure 3.6** IV Traces of fifth 300 Å  $\text{Ge}_{32}\text{Se}_{68}$  device from 10 K to 300 K.

### 3.2.6 IV Traces – 6<sup>th</sup> Device

Current-voltage traces of the 6<sup>th</sup> and final device that was tested at temperatures from 10 K to 300 K are shown in Figure 3.7. These traces are smooth with little noise. The same general trend of lower conduction with lower temperatures is present. This device has very distinct performance compared to the others. There appears to be a consistent reduction in conduction from 300 K to 150 K. From 150 K to 100 K, the conduction is very similar at low electric fields, then diverges at higher fields.

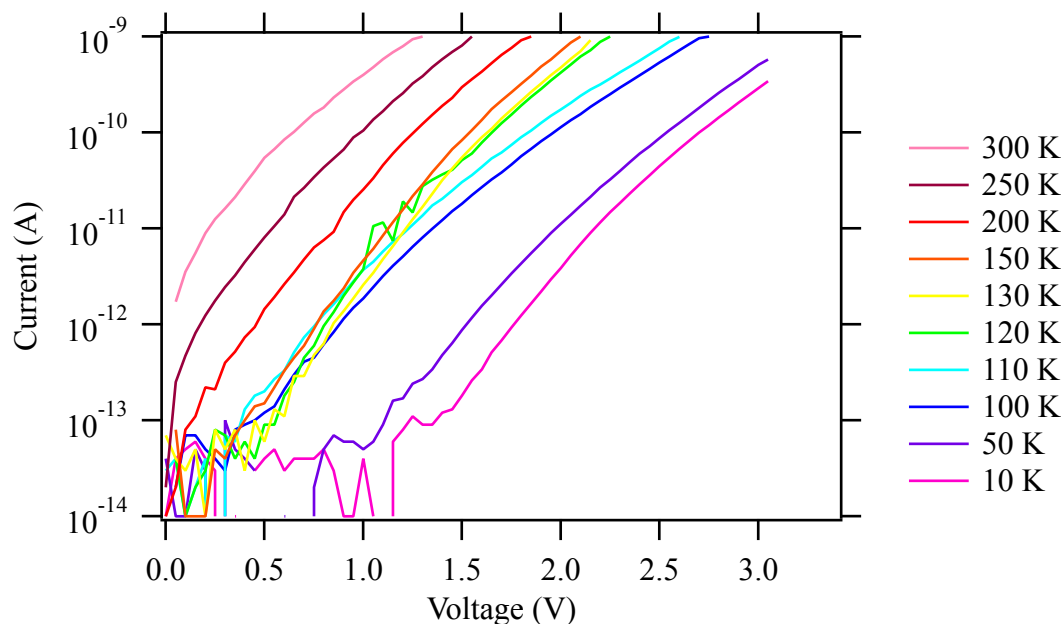


**Figure 3.7** IV Traces of sixth 300 Å  $\text{Ge}_{32}\text{Se}_{68}$  device from 10 K to 300 K.

### 3.2.7 Layout of Six $\text{Ge}_{32}\text{Se}_{68}$ Devices by Temperature

To see more clearly the impact of process variation on device performance, the IV traces of the six  $\text{Ge}_{32}\text{Se}_{68}$  devices are presented in a layout broken apart by temperature in Figure 3.8. The variation in conductance between devices within any temperature is about one to two orders of magnitude. The large performance variation between devices is one reason to investigate individual devices remeasured at each temperature for conduction mechanisms.

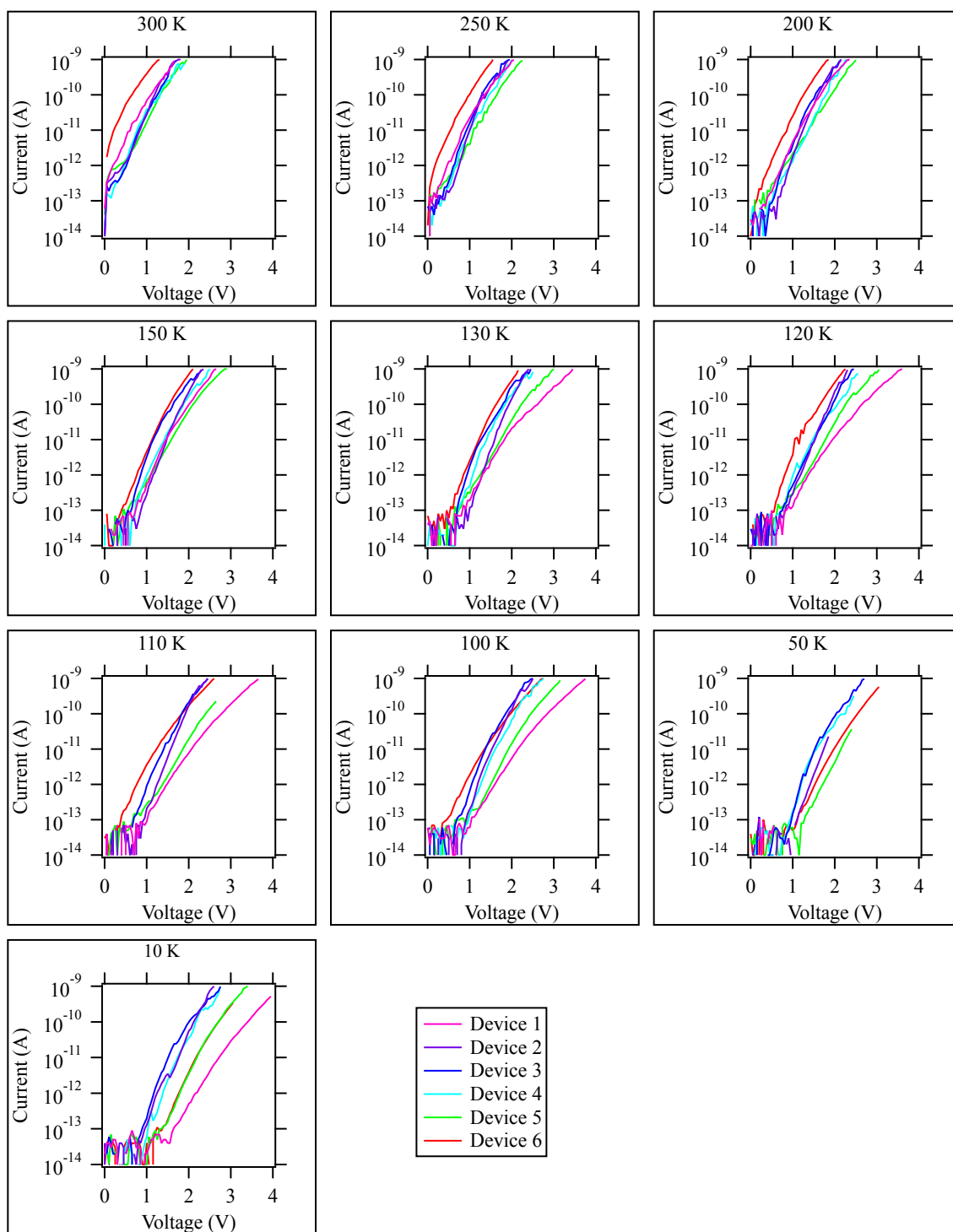
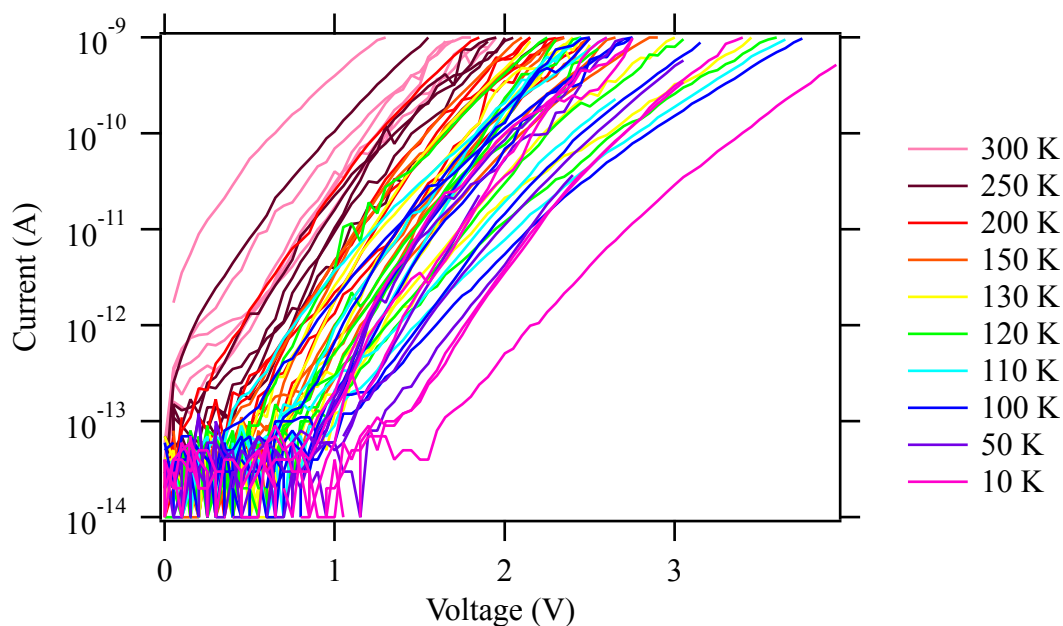


Figure 3.8 Layout plot of IV traces of six  $\text{Ge}_{32}\text{Se}_{68}$  Devices

### 3.2.8 Overlay of Six Ge<sub>32</sub>Se<sub>68</sub> Devices by Temperature

There are significant differences between the devices in terms of the impact of temperature and overall conduction magnitude. This difference is well-illustrated in Figure 3.9. It is apparent that for the sample under investigation, Ge<sub>32</sub>Se<sub>68</sub> conduction mechanisms cannot be determined by comparing different devices across temperatures. Possible sources of variation between these adjacent devices are film interface variation, film thickness variation, and variation of defects. In addition to device-related issues, there are likely variations related to probe contact resistance and top electrode damage from the probes.



**Figure 3.9** Overlay of IV traces of the six devices, 300 Å Ge<sub>32</sub>Se<sub>68</sub>, that were retested at each temperature from 10 K to 300 K.

### 3.2.9 Summary of Qualitative Assessment of IV Traces

In general, all six devices that were tested from 10 K to 300 K showed higher conduction with higher temperatures, which is expected. There were varying amounts of noise present in the traces. Certain devices had very distinct conduction differences

between temperatures, while others had trace overlap between temperatures. The magnitude of conduction differed between the devices.

To determine conduction mechanisms, the devices with the least noise and most distinct changes with temperature were chosen to model with known mechanisms. Those were the first and fifth devices.

### 3.3 Conduction Mechanisms of 300 Å Ge<sub>32</sub>Se<sub>68</sub>

The two devices with the least noise and most distinct performance across temperatures were modeled using known conduction mechanisms in amorphous resistive materials. The performance was modeled to band conduction in extended states, Mott's Variable Range Hopping ( $T^{1/4}$ ), Schottky Thermionic Emission, Poole-Frenkel Emission, and Fowler-Nordheim Tunneling.

#### 3.3.1 Band Conduction in the Extended States

The expectation for higher temperatures is that conduction occurs in the extended states because carriers will have more thermal energy. The equation for band conduction in the extended states has an Arrhenius form. This is shown in Eqn. 3.1, where  $\Delta E$  is the activation energy defined as  $E_C - E_F$ , the separation between the Fermi level and electron mobility edge.

$$\sigma = \sigma_0 \exp(-\Delta E/kT) \quad (3.1)$$

For the first device, conductance was determined for each temperature at 1.65 V. For the fifth device, conductance was determined for each temperature at 1.75 V. These voltages were chosen so that the conductance value could be shown for the entire temperature range. The plot of  $\ln(\sigma)$  vs  $1/T$  is shown in Figure 3.10. The slope of the

graph is  $-\Delta E/k$ , which allows calculation of the activation energy. The y-intercept is  $\ln(\sigma_0)$ . It is expected to see a linear plot if extended states conduction is occurring. The plot is not linear across all temperature ranges. It is clear that extended states conduction is not dominating for all temperatures. Visually, it appears extended states conduction may be happening for temperatures in the range of 200 K to 300 K.

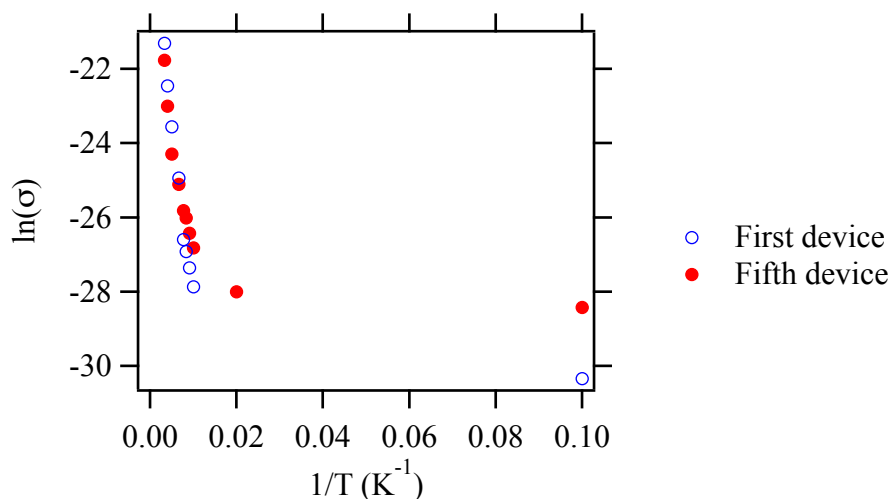


**Figure 3.10** Arrhenius extended states band conduction plot from 10 K to 300 K of first and fifth 300 Å  $\text{Ge}_{32}\text{Se}_{68}$  devices.

The possibility of extended states conduction from 200 K to 300 K was tested by performing a linear equation fit. The resultant fit is shown in Figure 3.11. For the fit quality, the resultant  $r^2$  was 0.985 for the first device and 0.990 for the fifth device. Solving the Arrhenius equation yields activation energies of 0.12 eV for the first device and 0.13 eV for the fifth device.

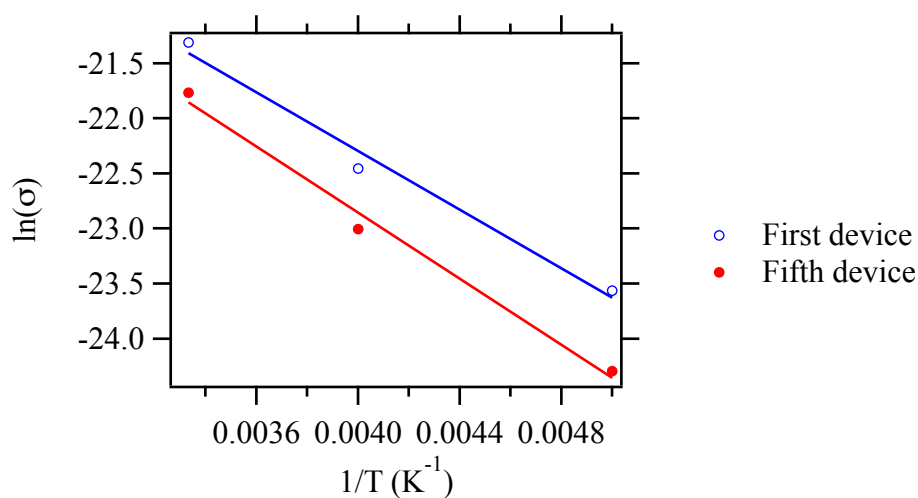


**Figure 3.11** Arrhenius extended states fit for 200 K to 300 K of first and fifth 300 Å  $\text{Ge}_{32}\text{Se}_{68}$  devices.

Equation fitting was performed for a larger temperature range, from 100 K to 300 K. The result is shown in Figure 3.12. The  $r^2$  value is worse compared to the 200 K to 300 K range. For the first device, the  $r^2$  value is 0.981, while for the fifth device, the  $r^2$  value is 0.945. Visually, it is clear that the data is not linear over the entire temperature range. There appear to be two regions of linearity – in higher temperatures ranging from 300 K to 200 K and in lower temperatures below 150 K.

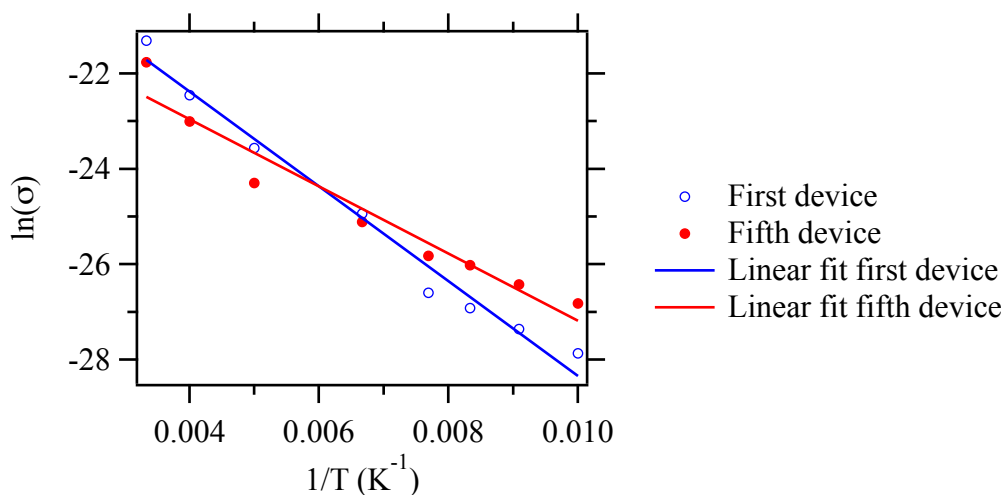


**Figure 3.12** Extended states conduction plot from 100 K to 300 K for first and fifth 300 Å  $\text{Ge}_{32}\text{Se}_{68}$  devices.

### 3.3.2 Mott's $T^{1/4}$ Variable Range Hopping

Mott's Variable Range Hopping is expected to occur at low temperatures because carriers may be jumping from localized states. The equation for Variable Range Hopping is shown in Eqn. 3.2.

$$\sigma_{DC} = \sigma_0 \exp[-(T_0/T)^{1/4}] \quad (3.2)$$

The plot needed is  $\ln(\sigma)$  vs  $T^{-1/4}$ . If the transformed plot is linear, then Variable Range Hopping may be occurring. The plot is shown in Figure 3.13. The overall trend is very similar to the extended states plot, with a region that appears to be linear from 300 K to 200 K, while fitting down to 100 K may be possible. It is clear that at the lowest temperatures, the response is no longer linear.

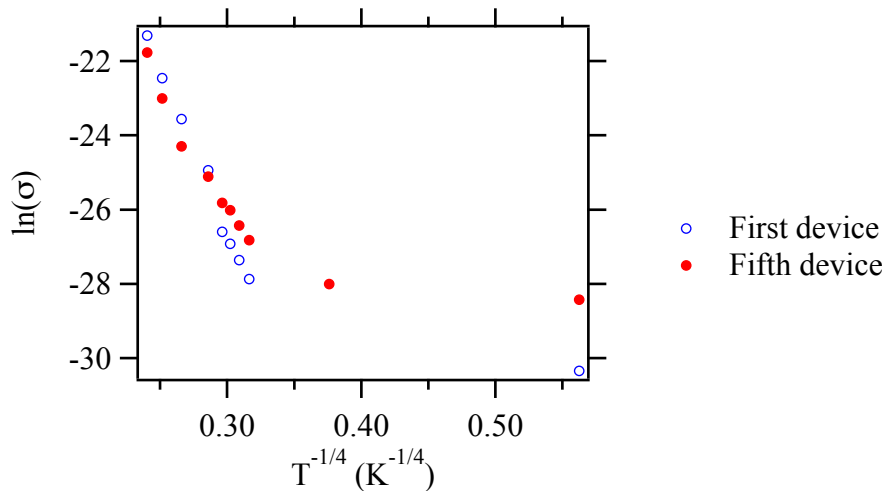


**Figure 3.13** Mott's Variable Range Hopping Plot of first and fifth 300 Å  $\text{Ge}_{32}\text{Se}_{68}$  devices.

To investigate the possibility of VRH occurring from 200 K to 300 K, a line was fit to the Mott's  $T^{1/4}$  plot in that region, which is shown in Figure 3.14. In terms of fit quality, the  $r^2$  value for the first device is 0.993. The extended states fit value was 0.985. For the fifth device, the VRH  $r^2$  is 0.996 compared to 0.990 with the extended states

conduction. Since both the band conduction in extended states plots and the Mott's VRH plots have linear regions for higher temperatures, they may be occurring simultaneously.

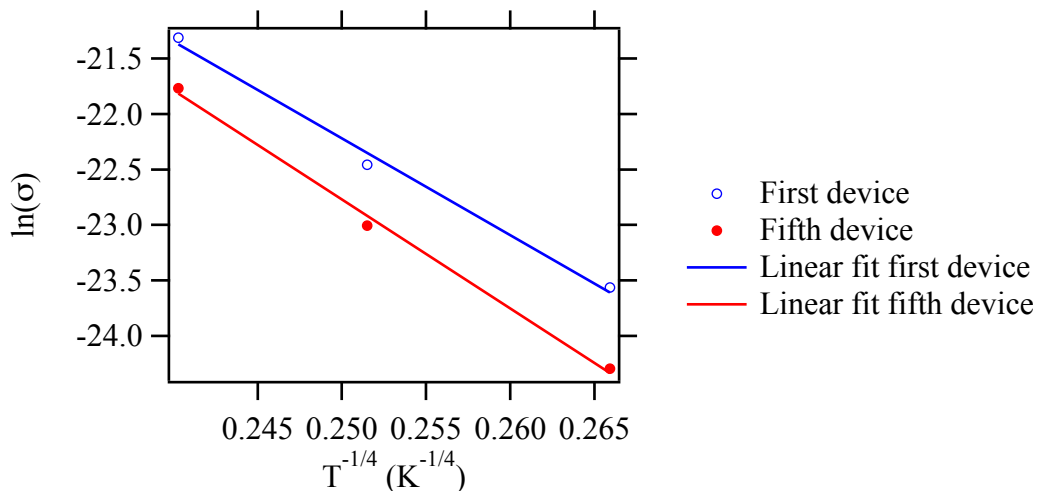


**Figure 3.14** Mott's Variable Range Hopping fit for 200 K to 300 K for first and fifth 300 Å  $\text{Ge}_{32}\text{Se}_{68}$  devices.

For VRH, linear equation fitting was performed from 300 K to 100 K because the range is closer to linearity than if the lowest temperatures are included. The result is shown in Figure 3.15. There are a few temperatures that clearly do not fit VRH, possibly due to noise, while others seem to fit. For the first device, the  $r^2$  value is 0.992. For the fifth device, the  $r^2$  value is 0.978.

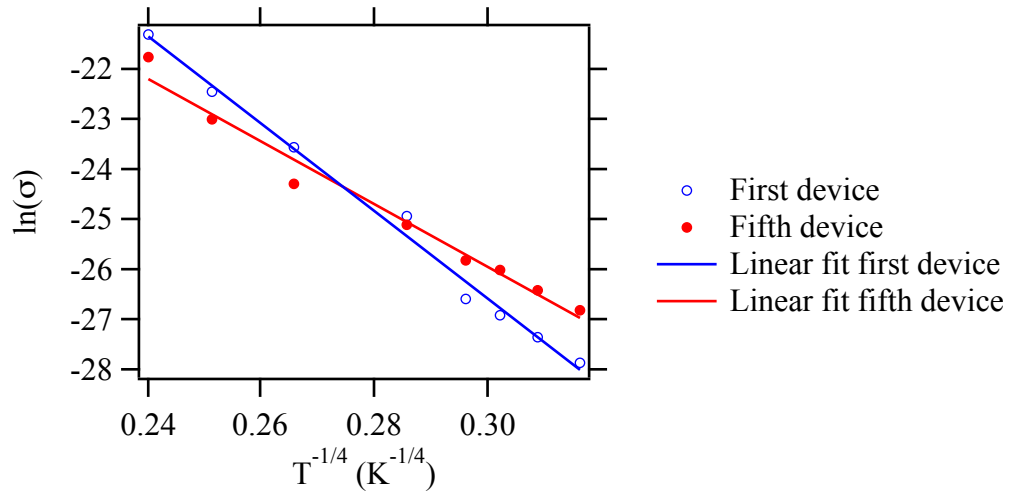


**Figure 3.15** Mott VRH plot from 300 K to 100 K for first and fifth 300 Å  $\text{Ge}_{32}\text{Se}_{68}$  devices.

### 3.3.3 Schottky Emission

Schottky emission is an electrode process of applied potential giving electrons the chance to surpass the energy barrier and move from the metal electrode into the conduction band of the insulator. The equation for Schottky emission is shown in Eqn.

3.3.

$$J = A^*T^2 \exp \left[ \frac{-q(\phi_B - \sqrt{qE/4\pi\epsilon_i})}{kT} \right] \quad (3.3)$$

For the two devices being modeled, the current-voltage traces were transformed to determine if Schottky emission is occurring. To determine this mechanism, a plot is generated of  $\ln(I)$  vs  $\sqrt{V}$  for each temperature. If the data is linear, the Schottky mechanism may be occurring. Then, the Schottky equations must be used to determine if the slopes and y-intercepts make sense and are valid.

### 3.3.3.1 Schottky Emission Results – First Ge<sub>32</sub>Se<sub>68</sub> Device

For the first device, the Schottky transformations are shown in Figure 3.16. It is clear that there is at least one linear region for each temperature. In some cases, there appear to be multiple regions. Such duality appears to be the case for temperatures below 150 K, where there is a larger slope at lower electric fields and a smaller slope at higher electric fields.

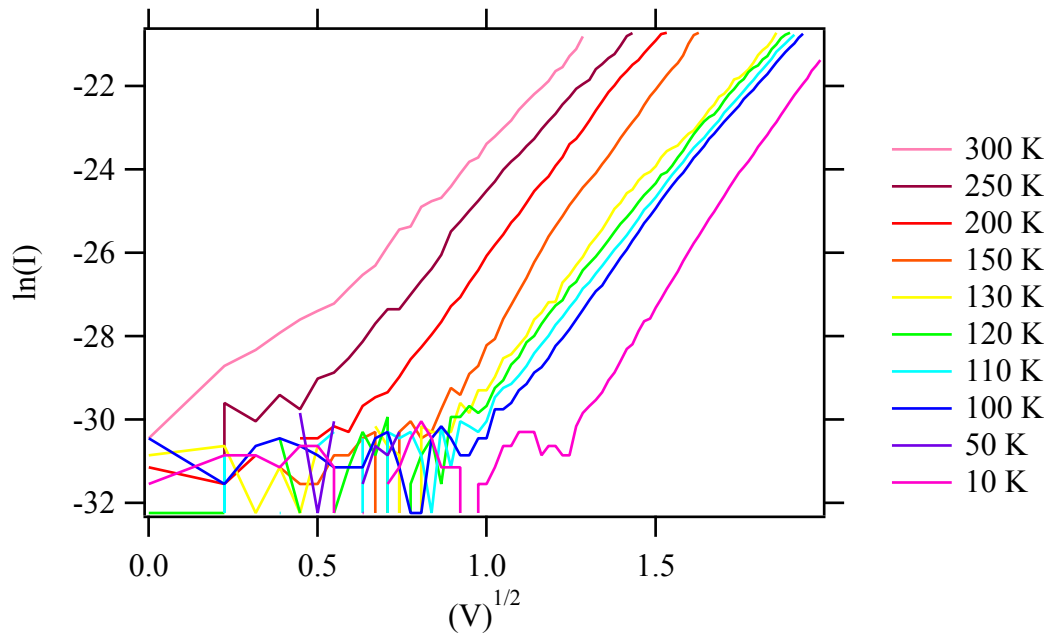


**Figure 3.16** Schottky transformations of first 300 Å Ge<sub>32</sub>Se<sub>68</sub> device.

To determine if the Schottky mechanism makes sense in light of the discovered linear regions, we solve for the slope and y-intercept. The y-intercept  $a$  and the slope  $b$  are shown in Eqns. 3.4 and 3.5.

$$a = -\frac{q\phi_B}{kT} + \ln(A^* \cdot T^2 \cdot \text{area}) \quad (3.4)$$

$$b = \frac{q}{kT} \sqrt{\frac{q}{4\pi\epsilon_i \text{thickness}}} \quad (3.5)$$

Investigating the temperature dependency of the slope is one way to validate the mechanism. From [19], it was shown that relative permittivity increases with temperature, especially prevalent at very high temperatures. The result is a slope trend that goes with  $1/T$ .

The slopes are plotted against  $1/T$  in Figure 3.17. The Schottky mechanism seems to fit for temperatures 300 K, 250 K, 200 K, and low field 150 K. For high field 150 K and the multiple slope results at lower temperatures, there doesn't appear to be any linear fit. The slopes seem to lose temperature dependency below 150 K. Using the linear region of slope, assuming permittivity doesn't change with temperature, the relative permittivity value (dielectric constant) is 1.89 with an uncertainty standard deviation of  $\sigma=0.31$ . The  $r^2$  value of the fit was 0.987. The dielectric constant of  $\text{Ge}_{32}\text{Se}_{68}$  has been shown to be about 7-8 [26].

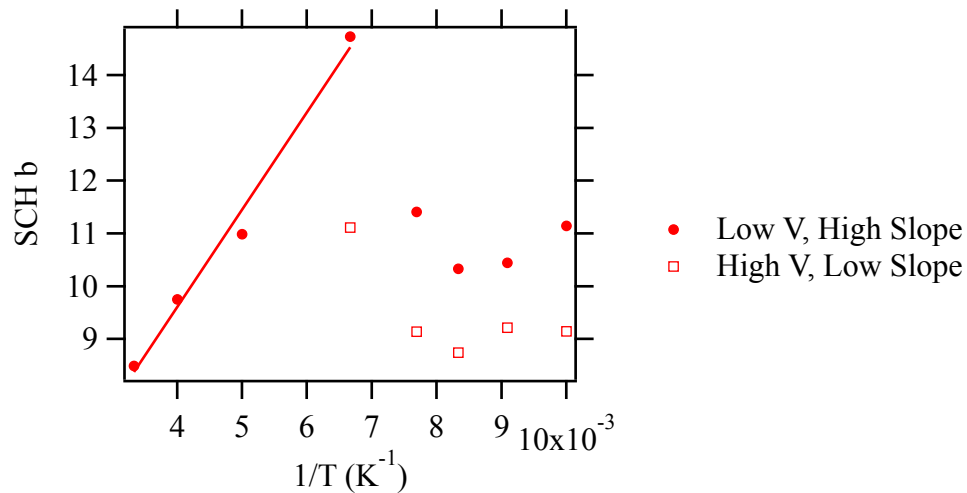


**Figure 3.17** Slopes of Schottky transformations for first 300 Å  $\text{Ge}_{32}\text{Se}_{68}$  device against inverse temperature.

### 3.3.3.2 Schottky Emission Results – Fifth $\text{Ge}_{32}\text{Se}_{68}$ Device

The Schottky transformations for the fifth 300 Å  $\text{Ge}_{32}\text{Se}_{68}$  device are shown in Figure 3.18. Similar to the first device, there appears to be at least one linear region. Also similar to the first device, for temperatures 150 K and below, there appear to be two linear regions – one of low field and higher slope and one of higher field and lower slope.

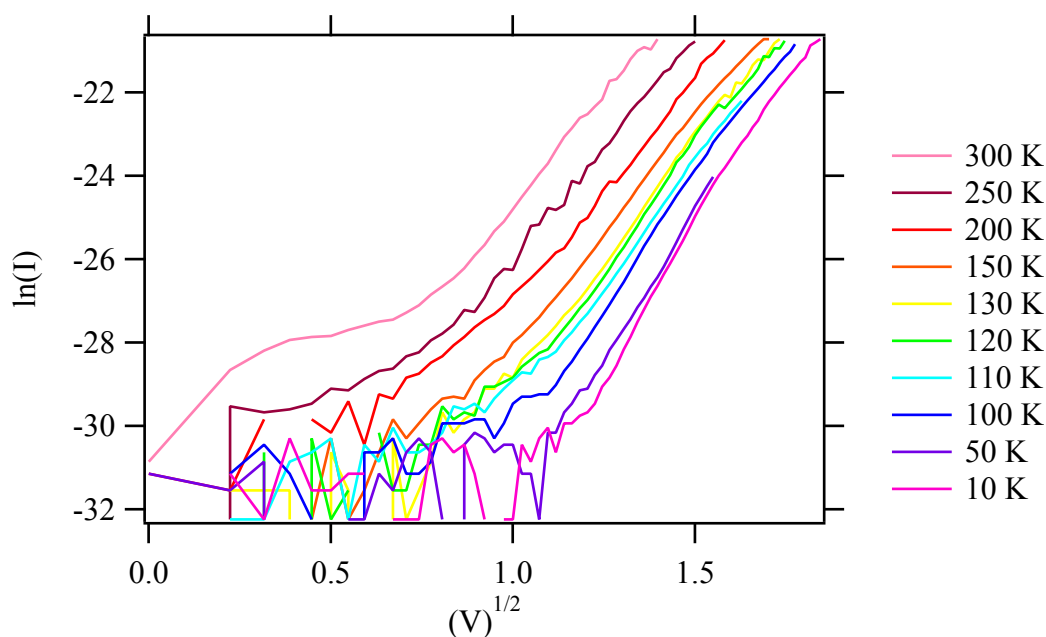


**Figure 3.18** Schottky transformations of fifth 300 Å  $\text{Ge}_{32}\text{Se}_{68}$  device.

In a similar way to the first device, the slopes were extracted from the Schottky transformations of the fifth device. The  $1/T$  slope plot is shown in Figure 3.19. The same slopes as the first device were linear equation fitted. The result is a relative permittivity,  $\epsilon_R = 38$ , with uncertainty standard deviation  $\sigma = 10$ . The standard deviation uncertainty is very large. Even at the low end of the statistical likelihood, the result is higher than the Feltz value of 7-8.

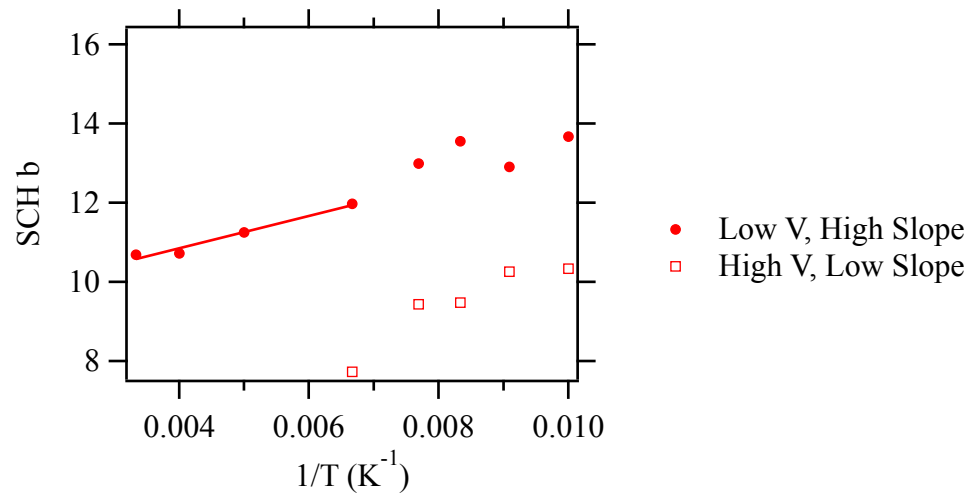


**Figure 3.19 Slopes of Schottky transformations for fifth 300 Å Ge<sub>32</sub>Se<sub>68</sub> device against inverse temperature.**

### 3.3.3.3 Schottky Emission Conclusion

Schottky transformations showed the possibility of Schottky emission occurring from 150 K to 300 K due to linear fitting of the Schottky model equation slopes over temperatures. When investigating more closely, the calculated permittivity values are not near to the literature values, with the first device having a much lower calculated permittivity than the literature, while the fifth device had a much higher calculated permittivity than the literature. Based on the result, it is unlikely that Schottky emission is occurring.

### 3.3.4 Poole-Frenkel Emission

To determine if the Poole-Frenkel emission mechanism is occurring in the two devices under investigation, the current-voltage traces were transformed and plotted. The y-axis was plotted as  $\ln(I/V)$ , and the x-axis was plotted as  $V^{1/2}$ . If the response is linear, there is a chance that Poole-Frenkel emission is occurring. The equation for Poole-Frenkel emission is shown in Eqn. 3.6.

$$J = CE \exp \left[ \frac{-(\phi_B - \sqrt{qE/\pi\epsilon_i})}{kT/q} \right] \quad (3.6)$$

Then, the slope and y-intercept coefficients are extracted and compared to the Poole-Frenkel equations. The solution for y-intercept,  $a$ , and slope,  $b$ , are shown in Eqns. 3.7 and 3.8. To determine the barrier height,  $\phi_B$ , the y-intercepts are plotted against  $1/T$ . A line fit of the trend will allow PF barrier height to be calculated. To determine the permittivity,  $\epsilon_i$ , the slopes are plotted against  $1/T$ .

$$a = \frac{-q\phi_B}{kT} + \ln \left( \frac{C \cdot \text{area}}{\text{thickness}} \right) \quad (3.7)$$

$$b = \frac{q}{kT} \sqrt{\frac{q}{\pi\epsilon_i \cdot \text{thickness}}} \quad (3.8)$$

#### 3.3.4.1 Poole-Frenkel Results - First Ge<sub>32</sub>Se<sub>68</sub> Device

The Poole-Frenkel transformed current-voltage traces for the first device are shown in Figure 3.20. There are linear regions. The result appears similar to the Schottky transformations. The traces for 300 K, 250 K, and 200 K have one slope, while temperatures 150 K and lower have two slopes. The overall trends in slope and y-intercept appear very similar to the Schottky case.

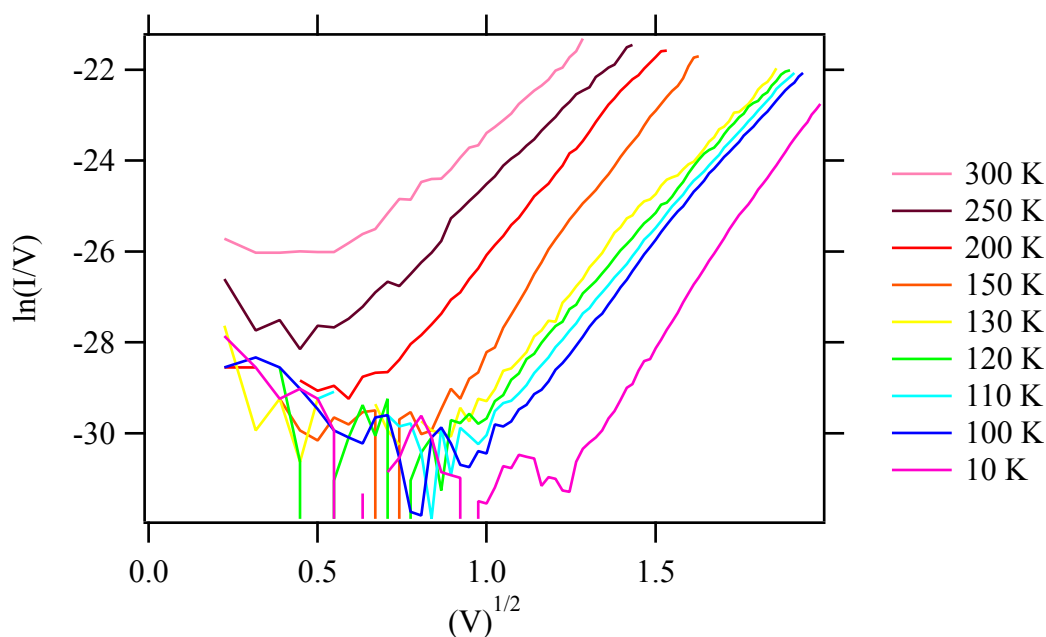


**Figure 3.20 Poole-Frenkel current-voltage transformations of first 300 Å  $\text{Ge}_{32}\text{Se}_{68}$  device.**

The slope for Poole-Frenkel is related to temperature and permittivity much as Schottky, but the Schottky slope includes a  $\frac{1}{4}$  term in the radical. By plotting slope versus  $1/T$  looking for linearity, the mechanism can be validated. As previously mentioned, the permittivity should increase with increasing temperature, which may cause the trend to slightly deviate from linearity.

The slopes of the Poole-Frenkel transformations plotted against  $1/T$  are shown in Figure 3.21. It appears that there is a linear fit from 300 K to 150 K as was also the case for the Schottky slopes. The permittivity result calculated is  $\epsilon_r=6.81$ , with a 1-sigma uncertainty of  $\sigma=0.78$ . The  $r^2$  of the fit was 0.994 compared to 0.987 with the Schottky slopes. Compared with the literature value of 7-8, the calculated permittivity with Poole-Frenkel is reasonable. As germanium content is reduced, the permittivity goes down [26].

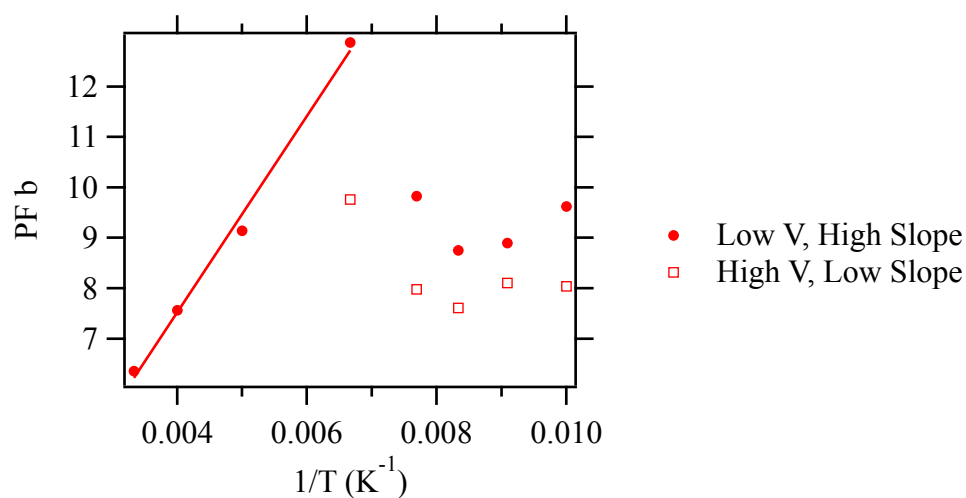


**Figure 3.21** Slopes of Poole-Frenkel transformations for first 300 Å Ge<sub>32</sub>Se<sub>68</sub> device against 1/T.

Investigating the y-intercept of the Poole-Frenkel transformations, which can determine the barrier height, is shown in Figure 3.22. There is a very nice linear portion from 300 K to 150 K. The  $r^2$  value is 0.9994. Using the Poole-Frenkel equation, from 300 K to 150 K, the barrier height is determined to be 0.295 eV, with an uncertainty of  $\sigma=0.005$  eV.

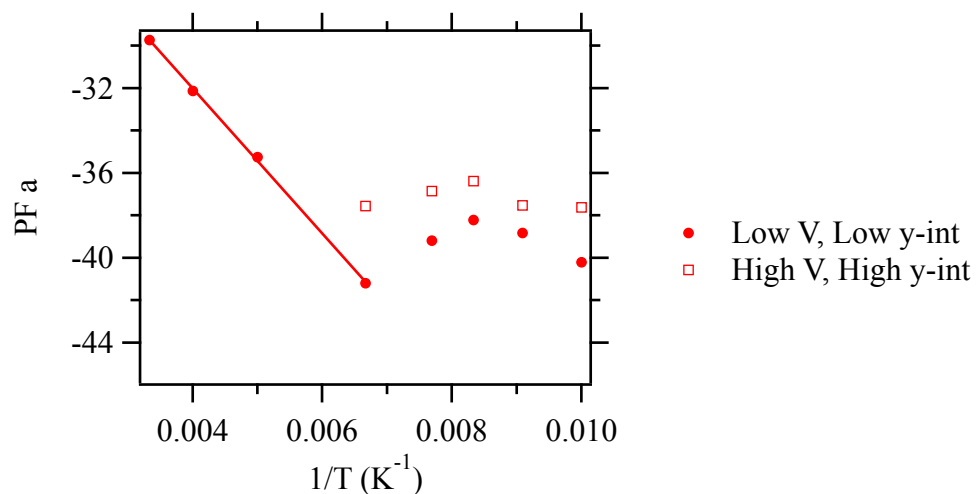


**Figure 3.22** Y-intercept of Poole-Frenkel transformations for the first 300 Å Ge<sub>32</sub>Se<sub>68</sub> device.

### 3.3.4.2 Poole-Frenkel Results – Fifth $\text{Ge}_{32}\text{Se}_{68}$ Device

The Poole-Frenkel transformations for the fifth device are shown in Figure 3.23.

Like with the first device, the Poole-Frenkel transformations have very similar characteristics to the Schottky transformations. There is a similar trend with temperature, and there is a bimodal slope for 150 K and colder.

Next, the slope and y-intercept of the linear regions are plotted in a similar way to the first device.

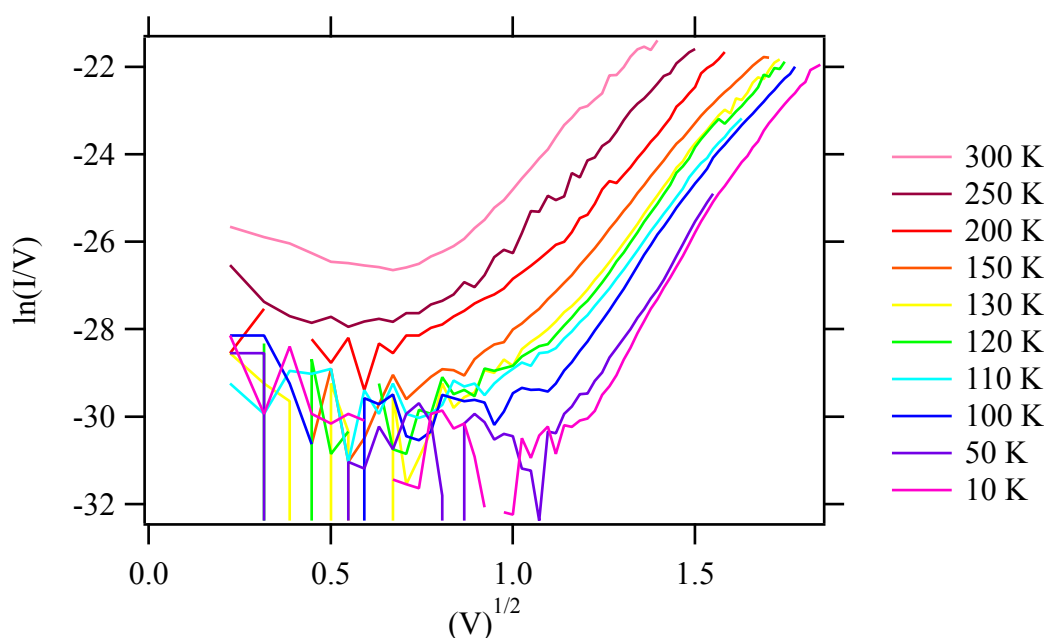


**Figure 3.23** Poole-Frenkel current-voltage transformations of fifth 300 Å  $\text{Ge}_{32}\text{Se}_{68}$  device.

Since the Poole-Frenkel y-intercept has a  $1/T$  dependency, it has been plotted versus  $1/T$  in Figure 3.24. Temperatures 300 K, 250 K, and 200 K have an excellent linear fit. The  $r^2$  value of the fit is 0.9998. Using the Poole-Frenkel equation, the calculated barrier height is 0.18 eV, with an uncertainty of  $\sigma=0.0026$ . For 150 K and

below, there isn't as good of a linear fit, and the barrier is reduced near to zero with large uncertainty. This is coupled with the addition of multiple slopes.

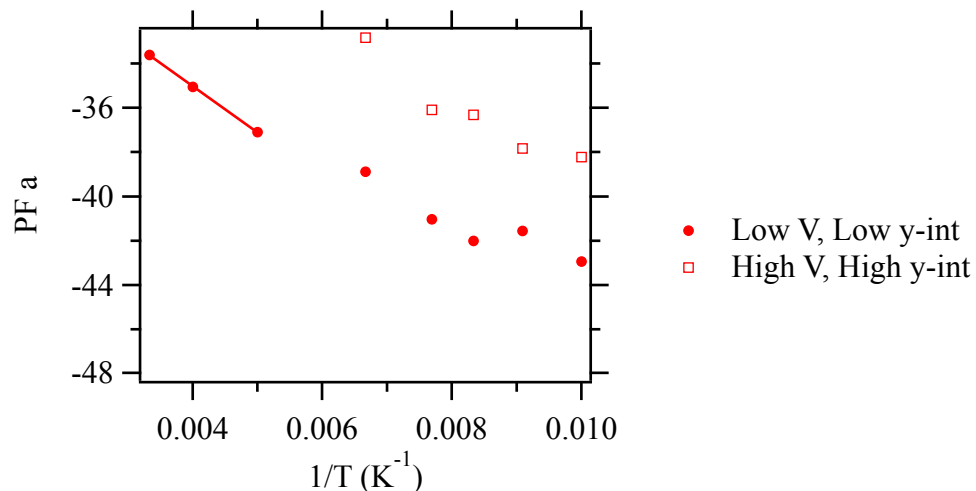


**Figure 3.24** Poole-Frenkel y-intercept of fifth 300 Å  $\text{Ge}_{32}\text{Se}_{68}$  device against  $1/T$ .

Next, the Poole-Frenkel slopes were plotted against  $1/T$  to see if there is a linear fit and to determine the permittivity. The result is shown in Figure 3.25. The fit was made from 300 K down to 120 K. The  $r^2$  value is 0.972. The calculated relative permittivity  $\epsilon_r=64$  with an uncertainty  $\sigma=11$ . Below 120 K, the mechanism did not fit.

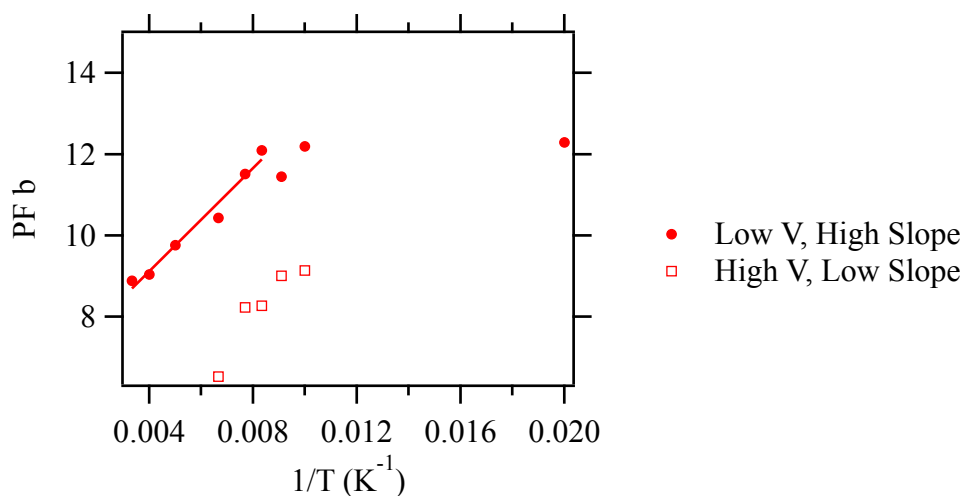


**Figure 3.25** Slopes of Poole-Frenkel transformations for fifth 300 Å  $\text{Ge}_{32}\text{Se}_{68}$  device plotted against  $1/T$ .

### 3.3.4.3 Poole-Frenkel Emission Conclusion

The y-intercept plots across temperature, used to determine barrier height, had good linearity for both devices down to 150 K in the case of the first device and down to 200 K in the case of the fifth device. The barrier height of the first device was calculated to be 0.295 eV, while the fifth device had a barrier height of 0.180. For the Poole-Frenkel slopes that determine permittivity, the fit for the first device was good down to 150 K, resulting in a calculated relative permittivity of 6.81, which is close to the literature value of 7-8. The fifth device did not have as good of a fit for the Poole-Frenkel slopes, but the fit went from 300 K down to 120 K. The relative permittivity was calculated to be 64, a much larger value than the first device. One possible explanation for the discrepancy might be film thickness uncertainty. If the film was in reality much thicker than 300 Å, the relative permittivity number could be inflated.

### 3.3.5 Fowler-Nordheim Tunneling

The Fowler-Nordheim Tunneling mechanism is most likely to occur for very thin films with sufficiently high electric field such that there is carrier tunneling across a triangular barrier into the conduction band of the insulator. To transform the I-V data, a Fowler-Nordheim plot must be created of  $\ln(I/V^2)$  versus  $1/V$ . If the data has a linear region, Fowler-Nordheim tunneling may be occurring.

#### 3.3.5.1 Fowler-Nordheim Tunneling Results – First Ge<sub>32</sub>Se<sub>68</sub> Device

The Fowler-Nordheim plot for the first device is shown in Figure 3.26. There does not appear to be a linear region. Fowler-Nordheim tunneling does not appear to be occurring in the first device.

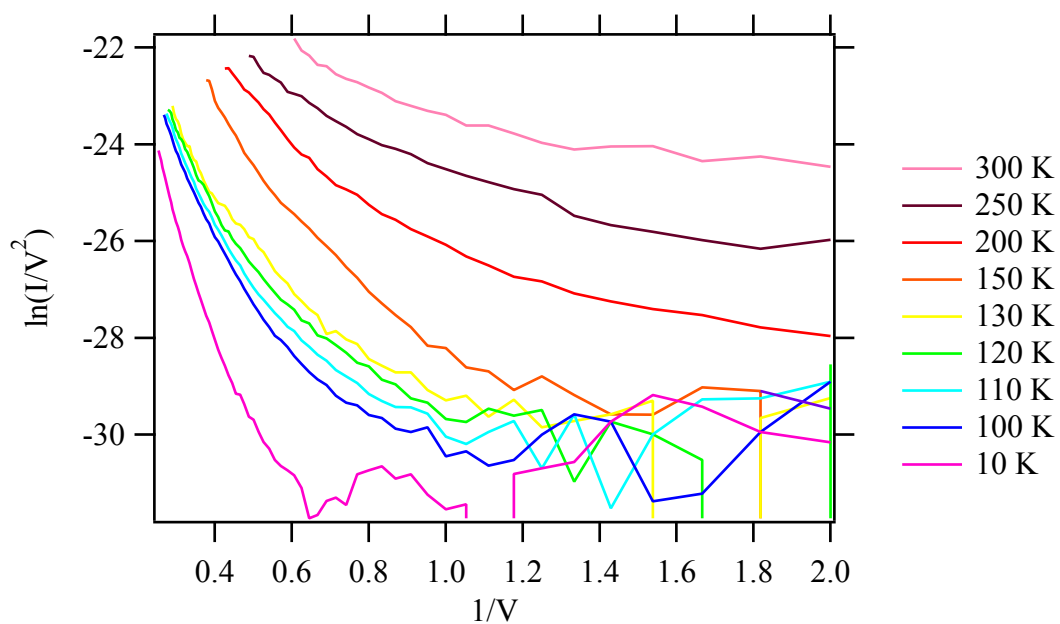


**Figure 3.26** Fowler-Nordheim tunneling current-voltage transformations for first 300 Å  $\text{Ge}_{32}\text{Se}_{68}$  device.

### 3.3.5.2 Fowler-Nordheim Tunneling Results – Fifth $\text{Ge}_{32}\text{Se}_{68}$ Device

The Fowler-Nordheim plots for the fifth device are shown in Figure 3.27. Again, there does not appear to be a linear region.

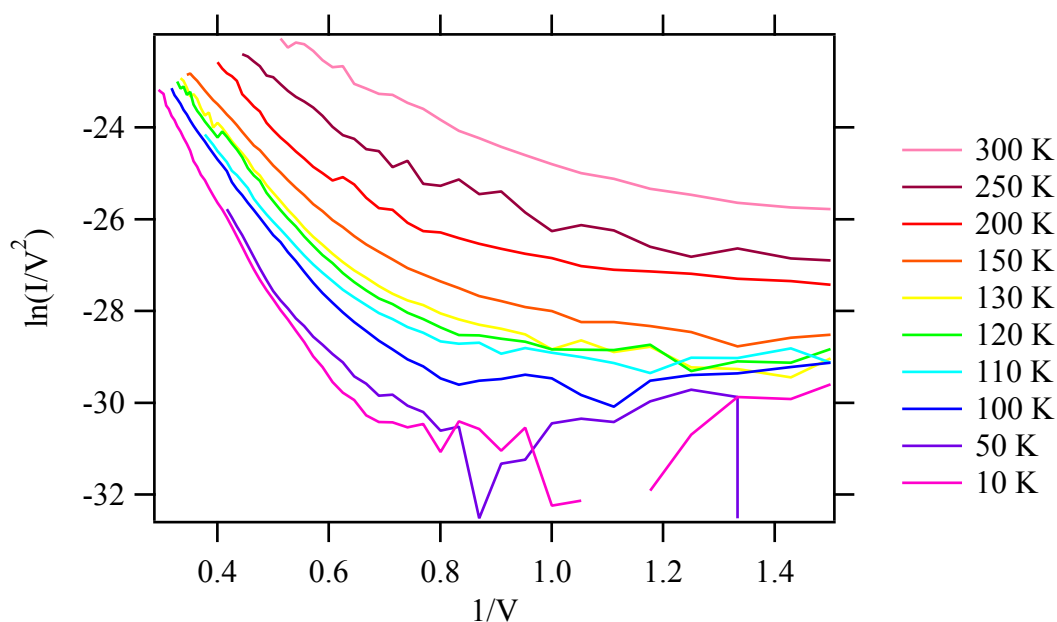


**Figure 3.27** Fowler-Nordheim tunneling current-voltage transformations for fifth 300 Å  $\text{Ge}_{32}\text{Se}_{68}$  device.

### 3.3.5.3 Fowler-Nordheim Tunneling Conclusion

Based on lack of linear fit to the  $\ln(I/V^2)$  vs  $1/V$ , Fowler-Nordheim tunneling is probably not occurring in this system.

### 3.3.6 Conclusion of Conduction Mechanisms in 300 Å $\text{Ge}_{32}\text{Se}_{68}$

Current-voltage sweeps were performed on six adjacent devices, stopping at a compliance current of 1 nA for 10 temperatures ranging from 10 K to 300 K. The commonality between the devices is the general trend of higher conduction at higher temperatures.

Two of the devices with smoother traces were selected to fit to five known conduction mechanisms of resistive amorphous materials: band conduction in the extended states, Mott's Variable Range Hopping, Schottky emission, Poole-Frenkel

emission, and Fowler-Nordheim Tunneling. The summary of results is shown in Table 3.1.

**Table 3.1 Summary of Electron Conduction Mechanism Results for 300 Å Ge<sub>32</sub>Se<sub>68</sub>**

Mechanism	Device	Temp Range	r <sup>2</sup>	Calculated properties	Viable Mechanism?
Extended States	1 <sup>st</sup>	200-300 K	0.985	E <sub>a</sub> =0.12 eV	Yes
	5 <sup>th</sup>	200-300 K	0.990	E <sub>a</sub> =0.13 eV	Yes
Variable Range Hopping	1 <sup>st</sup>	200-300 K	0.992		Yes
	5 <sup>th</sup>	200-300 K	0.978		Yes
Schottky emission	1 <sup>st</sup>	150-300 K	0.987	ε <sub>r</sub> =1.89 ± 0.31	No
	5 <sup>th</sup>	150-300 K	0.972	ε <sub>r</sub> =39 ± 10	No
Poole-Frenkel emission	1 <sup>st</sup>	150-300 K	0.9994	φ=0.295 ± 0.005 eV	Yes
			0.994	ε <sub>r</sub> =6.81 ± 0.78	
	5 <sup>th</sup>	200-300 K	0.9998	φ=0.180 ± 0.003 eV	No
			0.942	ε <sub>r</sub> =88, ±1σ from 56-156	
		120-300 K	0.972	ε <sub>r</sub> =64 ± 11	
Fowler-Nordheim Tunneling	1 <sup>st</sup>	No fit	No fit	No fit	No
	5 <sup>th</sup>	No fit	No fit	No fit	No

None of the mechanisms investigated fit well for temperatures below 150 K.

There was a general reduction of conductivity for T < 150 K, but it was not enough reduction to fit it to the known conduction mechanisms.

The mechanisms that were ruled out were Schottky emission based on unreasonable permittivity values and Fowler-Nordheim tunneling due to lack of fit.

Mechanism transformations had good linearity for the remaining three mechanisms of Extended States conduction, Variable Range Hopping, and Poole Frenkel emission. For the first device, the best fitting mechanism is Poole-Frenkel from 150 K to 300 K. The calculated permittivity was reasonable compared to the literature. For the

fifth device, Poole-Frenkel has the best fit for the slopes that determine barrier height from 200-300 K. The Poole-Frenkel permittivity for the fifth device was not reasonable. Extended states conduction transformations had good linearity from 200-300 K. The calculated extended states activation energy of 0.12 eV was consistent between the two devices. Additionally, both transformations for variable range hopping showed good linearity.

Based on the mechanism fitting, it appears that the three mechanisms of band conduction in the extended states, Mott's variable range hopping, and Poole-Frenkel emission may be occurring in 300 Å  $\text{Ge}_{32}\text{Se}_{68}$  conduction. The first device had a higher likelihood of Poole-Frenkel conduction compared to the fifth device. For temperatures below 150 K, more work needs to be done to understand why the mechanisms break down, whether it is an impact from experimental apparatus, or if there is a fundamental shift in properties below 150 K.

## CHAPTER 4: WRITE CHARACTERISTICS OF ION-CONDUCTING SWITCHING DEVICES

### 4.1 Experimental Summary

Two types of ion-conducting devices were electrically tested: both using Ag as the mobile ion. The first is shown in Figure 4.1, and the second structure uses a metal chalcogenide layer (SnSe) above the  $\text{Ge}_{32}\text{Se}_{68}$  layer as shown in Figure 4.2.

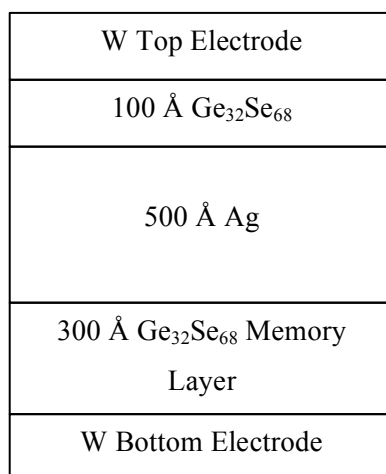


**Figure 4.1** Cross-sectional diagram of Ag-only ion-conducting test device.

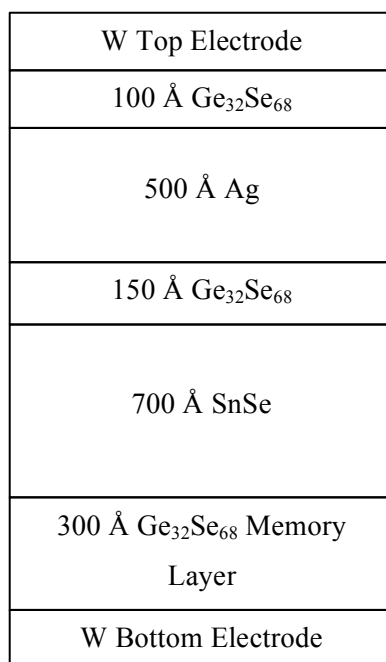


**Figure 4.2** Cross-sectional diagram of the Ag+SnSe ion-conducting device.

#### 4.1.1 Experimental Procedure – Devices Tested

Since eliminating avoidable variation was of utmost importance, two methods were used in testing both types of devices. The first method was to retest each device at each temperature, referred to as ‘devices that were retested.’ The intent was to model the performance of an individual device across temperatures. Three Ag-only devices and three Ag+SnSe devices were tested in this way. The second method was to test an unused device at a single temperature. Each of those devices can be considered “fresh” for each test. Three Ag-only devices and three Ag+SnSe devices were tested “fresh” at each temperature.

Devices from each of the two testing methods contained unwanted variation. The devices that were retested at each temperature include effects such as rewrite instability,

electrode damage from multiple probe landings, and material structure change from multiple write-erase cycles. The devices that were tested “fresh” at each temperature include effects such as process variation from device to device and probe contact resistance variations. By considering both groups of devices, a more complete picture of performance may emerge.

#### 4.1.2 Electrical Testing Sequences

For the “fresh” devices, the sequence of testing is shown in Table 4.1. It consists of reading the initial state of the device, an initial forming write, an erase, and a second write. Reading the device is also performed between write and erase. The write sweep is set to stop at the compliance current of 50  $\mu\text{A}$ , which is a measurement option for the HP 4156A. It has been demonstrated that multiple resistance states are possible by adjusting the compliance current [11], but for the purposes of this study, keeping the compliance current consistent takes out a variable that could confound the conduction mechanism study. The read is performed with maximum voltage of 20 mV to test the device at a low enough potential to prevent the resistance state from changing. The current is limited to 50  $\mu\text{A}$ , which is the same as the write compliance current. The erase is performed with a negative top electrode voltage sweep. Since it is desired to stop the erase after the device turns off, it was necessary to stop the sweep manually. When plotting current on a log scale, it is apparent when the device turns off, as the current decreases several orders of magnitude in a step function. When that occurs, the sweep is manually stopped. See Figure 1.3 for an example of the IV curve.

**Table 4.1 Sequence of Testing for Fresh Switching Devices.**

<b>Function</b>	<b>Notes</b>
1. Read 1	20 mV max voltage in steps of 1 mV, 50 $\mu$ A compliance current.
2. Write 1	Max limit of 50 $\mu$ A compliance current. 10 mV steps.
3. Read 2	20 mV max voltage in steps of 1 mV, 50 $\mu$ A compliance current.
4. Erase	Negative voltage sweep. 10 mV steps. Manually stop after device switches off.
5. Read 3	20 mV max voltage in steps of 1 mV, 50 $\mu$ A compliance current.
6. Write 2	Max limit of 50 $\mu$ A compliance current. 10 mV steps.
7. Read 4	20 mV max voltage in steps of 1 mV, 50 $\mu$ A compliance current.

For the second method of testing (“retested devices”), the devices were retested at each temperature. For the first device cycle at 300 K, the “fresh” sequence was used. Subsequent cycles use the electrical testing sequence shown in Table 4.2. The electrical test sequence starts with an erase. In previous testing that is not reported on in this work, it was noticed that sometimes devices that were erased at a previous temperature had low resistance during the write at the next temperature. Erase 1 ensures that the device is not written. There is one write and a second erase. The device is read between the write and erase sequences.

**Table 4.2 Sequence of Testing for Switching Devices Retested at Each Temperature**

<b>Function</b>	<b>Notes</b>
1. Erase 1	Negative voltage sweep. 10 mV steps. Manually stop after device switches off.
2. Read 1	20 mV max voltage in steps of 1 mV, 50 $\mu$ A compliance current.
3. Write	Max limit of 50 $\mu$ A compliance current. 10 mV steps.
4. Read 2	20 mV max voltage in steps of 1 mV, 50 $\mu$ A compliance current.
5. Erase 2	Negative voltage sweep. 10 mV steps. Manually stop after device switches off.

#### 4.1.3 Experimental Procedure – Temperature Measurements

The devices were tested at 300 K, and then the temperature was reduced in steps down to 10 K. For each temperature tested, at least 45 minutes of stabilization time was given to ensure temperature stability. At temperatures 50 K and 10 K, there was significant top electrode breakage. In many cases, devices were shorted due to the breakage.

#### 4.1.4 Conduction Mechanisms

To test the conduction mechanisms during writing, the write IV curves were transformed using all mechanisms, both ion and electron. During writing, both ion conduction and electron conduction are happening.

For ion conduction, two mechanisms were investigated: Butler-Volmer electrode redox and Mott-Gurney ion hopping. The transformations performed are shown in Table 4.3.

The Butler-Volmer electrode redox equation is shown in Eqn. 4.1 [15]. For the analysis performed in this work, the high-field approximation was used.

$$I = I_0 \left[ \frac{c_o(0,t)}{c_o^*} \exp\left(\frac{\alpha\eta}{kT/q}\right) - \frac{c_r(0,t)}{c_r^*} \exp\left(-\frac{(1-\alpha)\eta}{kT/q}\right) \right] \quad (4.1)$$

The Butler-Volmer high-field approximation is shown in Eqn. 4.2 [15].

Overpotential  $\eta$  is equal to the applied potential.

$$\ln I = \frac{\alpha}{kT/q} \eta + \ln I_0 \quad (4.2)$$

The Mott-Gurney hopping equation is shown in Eqn. 4.3 [16].

$$J = 2qCav \cdot \exp\left(-\frac{W_a^0}{kT/q}\right) \cdot \sinh\left(\frac{aE}{2kT/q}\right) \quad (4.3)$$

The equation consists of the hopping distance  $a$ , the concentration of mobile cations  $C$ , the hopping rate  $\nu$ , and the energy barrier  $W_a^0$ . At high electric fields, the hyperbolic sine tends to an exponential as shown in Eqn. 4.4 [10].

$$J = 2qCav \cdot \exp\left(-\frac{W_a^0}{kT/q}\right) \cdot \exp\left(\frac{aE}{2kT/q}\right) \quad (4.4)$$

The write traces were transformed using the MG and BV high-field approximations and investigated for linearity, which may indicate that the conduction mechanism is dominating.

**Table 4.3 Transformations Performed on Write Traces to Determine Ion-Conduction Mechanism**

<b>Mechanism</b>	<b>Transformation</b>	<b>Action</b>
High Field Mott-Gurney ion hopping	Plot $\ln(I)$ vs $V$	Slope determines hopping distance. Y-intercept can be used to determine activation energy.
High Field Tafel electrode redox	Plot $\ln(I)$ vs $V$	Slope determines transfer coefficient, $\alpha$ .

#### 4.1.5 Notes on Potential Experimental Error

For the temperatures 50 K and 10 K, the tungsten probe tip damaged the top electrode metal. There may be thermal expansion effects or possibly material fracture strength impacts at low temperatures. In some cases, there was shorting from the top electrode to the bottom electrode. This damage is why some devices are missing the lowest temperature data. An image of the damage is shown in Figure 4.3.



**Figure 4.3** Image of top electrode damage at 50 K of fresh Ag+SnSe device.

#### **4.2 Electron Conduction During Write Process**

All write IV traces were transformed using the equations for all electron conduction mechanisms that were tested in Chapter 3 on the  $\text{Ge}_{32}\text{Se}_{68}$  material. It was found that none of the electron-conduction mechanisms fit the write traces. This is likely due to the interaction effect of both electron and ion conduction during the write. Additionally, the incorporation of Ag into the  $\text{Ge}_{32}\text{Se}_{68}$  memory layer, even before the filament bridges the gap, may change the conduction properties of the material.

#### **4.3 Ag-Only Switching Device Write Characteristics – Devices Retested Across Temperatures**

In this section, the current-voltage traces of the devices that were retested across temperatures and the current-voltage traces of the fresh devices are presented. Tests started at 300 K and were stepped down. The devices were tested in the same order at each temperature. The curves are transformed using the ion-conduction mechanisms of Butler-Volmer electrode redox and Mott-Gurney ion hopping. Transformed graphs with linear characteristics may fit the mechanism. Additionally, in this section, the write threshold voltage characteristics are modeled.

#### 4.3.1 IV Traces of Ag-Only Ion-Conducting $\text{Ge}_{32}\text{Se}_{68}$ Devices

The IV traces as a function of temperature of Ag-only device 1 are shown in Figure 4.4. The write sweeps were stopped at a compliance current  $50\ \mu\text{A}$ .

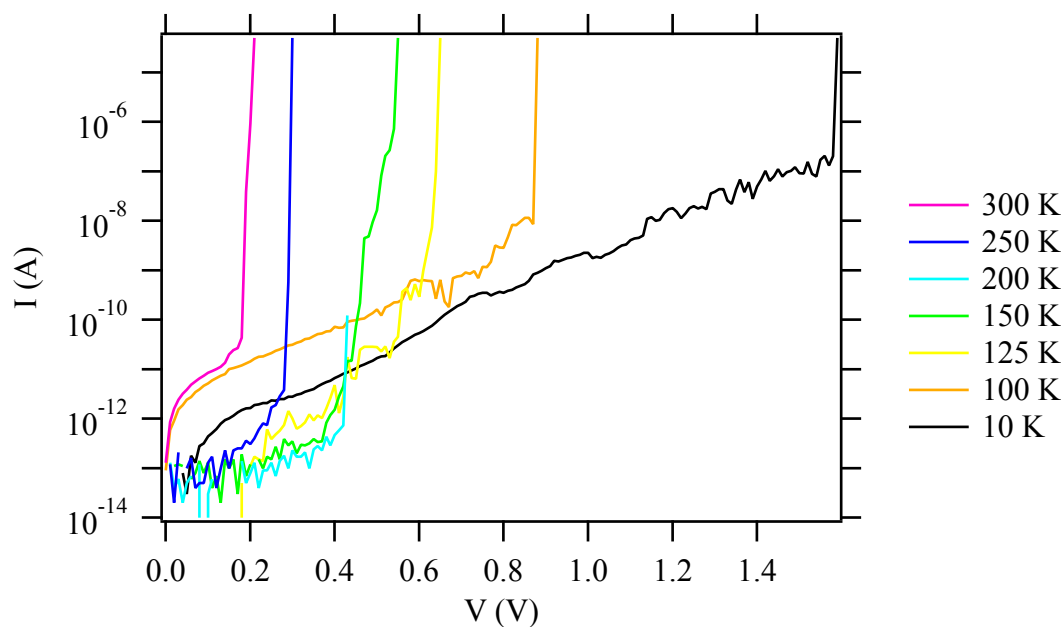


**Figure 4.4** IV traces of  $50\ \mu\text{A}$  write for Ag-only switching device #1 retested across temperatures.

Write traces for Device 2 are shown in Figure 4.5. Traces for 50 K and 10 K are not shown due to device shorting, which was probably a result of top electrode damage.

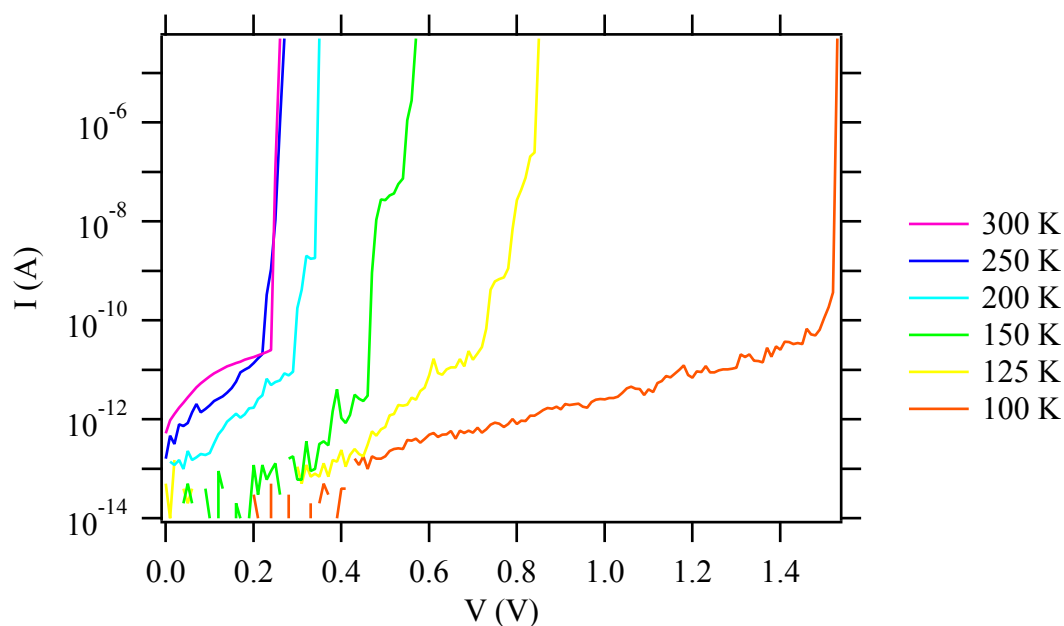


**Figure 4.5** IV traces of 50  $\mu\text{A}$  write for Ag-only switching device #2 retested across temperatures.

Write traces for Ag-only device 3 retested across temperature are shown in Figure

4.6.

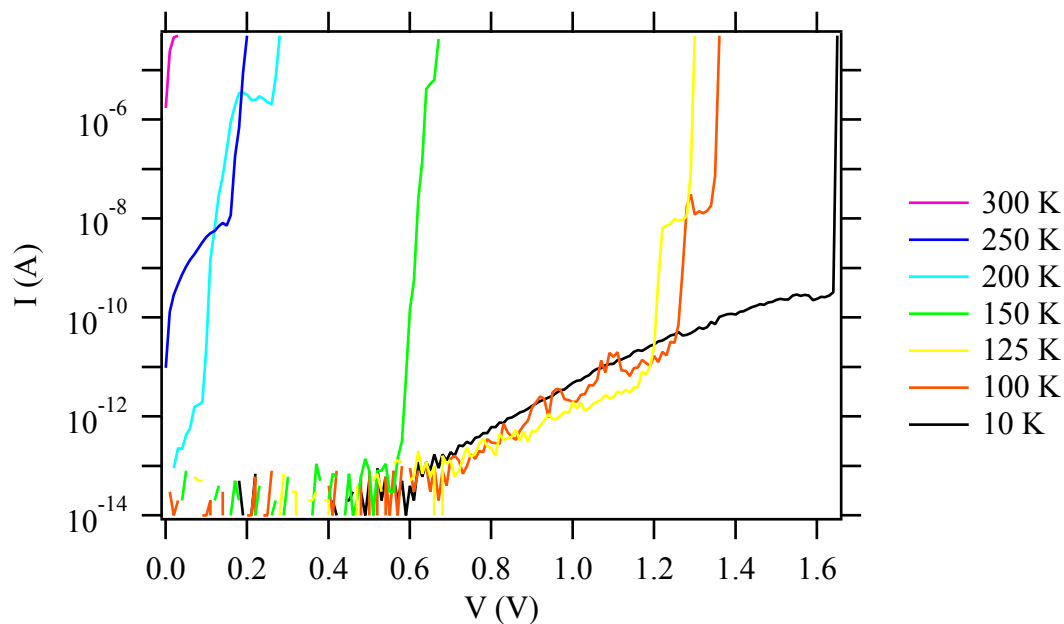


**Figure 4.6** IV traces of 50  $\mu\text{A}$  write for Ag-only switching device #3 retested across temperatures.

#### 4.3.2 Layout Plot of IV Write Traces of Ag-Only Devices Retested at Each Temperature

To visually characterize the variations between devices, a layout plot showing the write traces of all three Ag-only devices at each temperature is given in Figure 4.7.

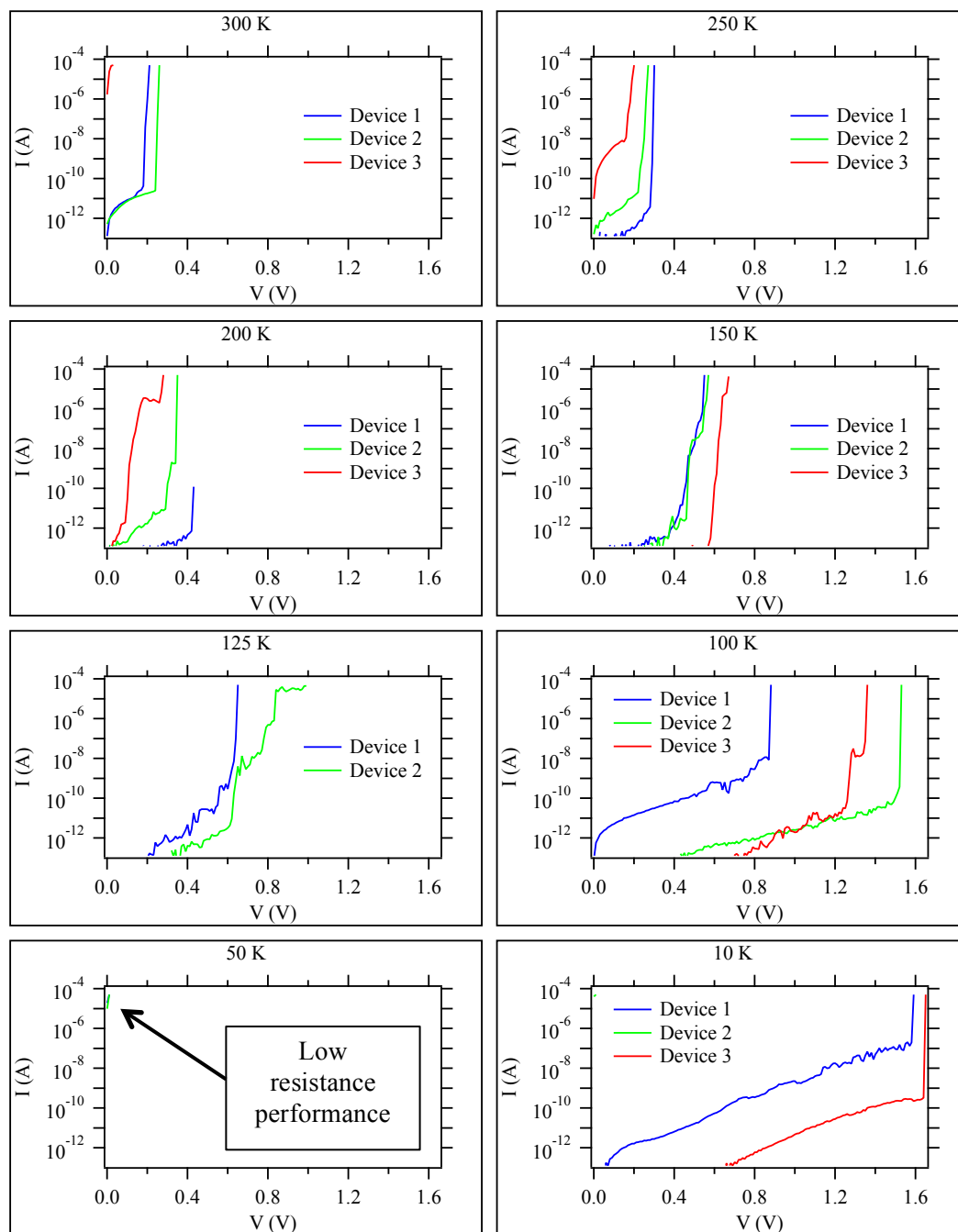


**Figure 4.7** Layout plot of IV write traces of Ag-only Devices Retested Across Temperatures

#### 4.3.3 Ion-Conduction Mechanisms Comments

To analyze the ion-conduction mechanisms for Ag-only devices, the write traces were investigated using the Butler-Volmer equation and the Mott-Gurney hopping equation. The high-field simplification was used for both. At low electric fields, traces did not show linearity. For the high field MG and BV mechanisms, a plot of  $\ln(I)$  vs  $V$  is linear.

The current-voltage traces for the Ag-only devices retested at each temperature were visually inspected for likelihood of MG hopping or BV electrode redox. There were few traces that fit to the mechanisms. The conclusion is that neither of the mechanisms fit in a reliable way for the Ag – 300 Å  $\text{Ge}_{32}\text{Se}_{68}$  system.

#### 4.3.4 Threshold Voltage Characteristics

For this test, threshold voltage is defined as the voltage at which the current reaches a compliance level of 50  $\mu\text{A}$ . The conduction increases very rapidly at currents lower than 50  $\mu\text{A}$ , so threshold voltage is similar for currents within a few orders of magnitude. The threshold voltage can be thought of as a measure of the ion conduction, since the metal ions have to move and deposit to form the filament. High threshold voltage means low ion conduction.

The threshold voltage is plotted against temperature for the three Ag-only devices that were retested at each temperature, shown in Figure 4.8. As expected, there is a general trend of higher threshold voltage at lower temperatures. The differences in performance between devices become larger at lower temperatures. There may be a thermally activated Arrhenius-type dependency for the threshold voltage with lower

temperatures. In response, the conductance at threshold ( $50 \mu\text{A} / V_{\text{TH}}$ ) was plotted against  $1/T$ .

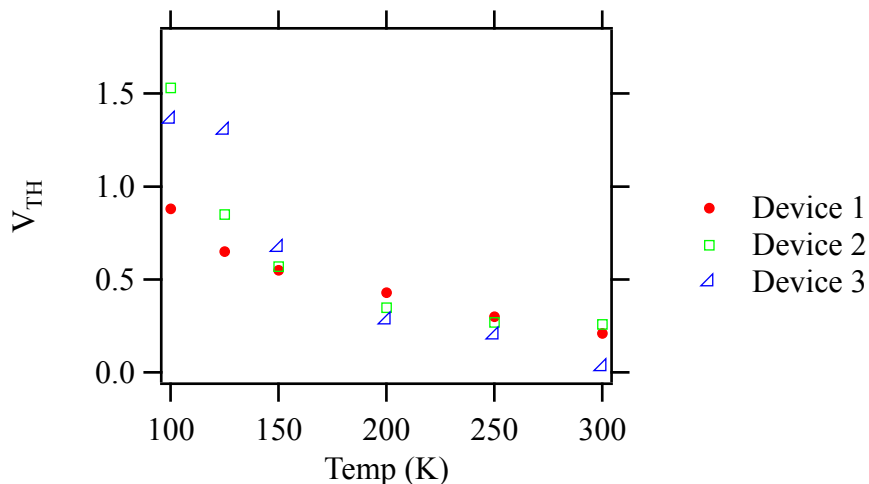


**Figure 4.8** Threshold voltage of Ag-only devices retested across temperatures.

The conductance at threshold vs  $1/T$  traces are shown in Figure 4.9. There is Arrhenius activation for Device 1 from 300 K to 200 K; then the activation energy (slope) changes from 200 K to 100 K. For Device 2, the Arrhenius plot is linear from 250 K down to 100 K. For Device 3, the performance was unstable and did not fit well to the Arrhenius form.

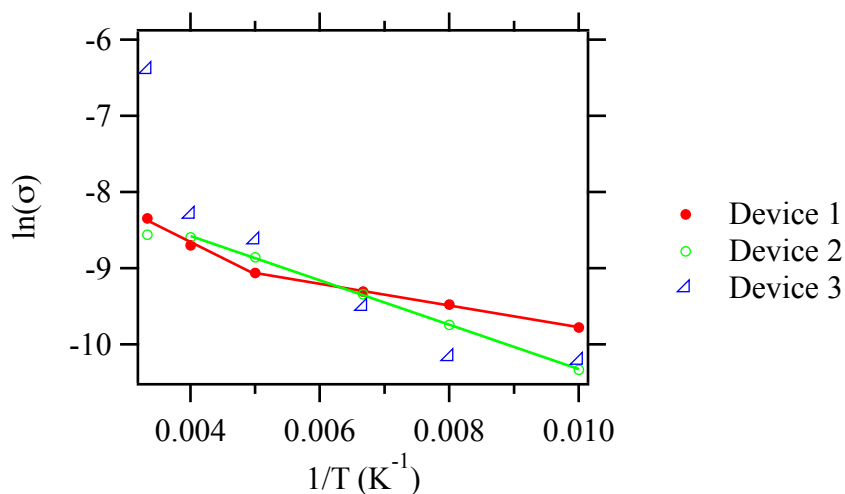


**Figure 4.9** Arrhenius plot of conductance at threshold for Ag-only devices retested across temperatures.

The activation energy results are shown in Table 4.4. The results are within the same order of magnitude when comparing the two regions of device 1 and device 2.

Differences may be due to noise.

**Table 4.4 Conductance at Threshold Activation Energies for Ag-Only Devices Retested Across Temperatures**

Device	Temperature Range	Activation Energy
1	100-200 K	0.012 eV
	200-300 K	0.037 eV
2	100-250 K	0.025 eV

#### **4.4 Ag-Only Switching Device Write Characteristics – Fresh Devices at Each Temperature**

Three untested “fresh” devices were probed at each temperature. As was mentioned previously, two writes were performed on the devices. The first write may have more variation due to the initial electroforming process.

##### **4.4.1 Write Traces of Ag-Only Fresh Devices**

For the Ag-only devices, the initial write traces are shown in Figure 4.10. The writes were stopped at compliance current 50  $\mu$ A. There is a large amount of variation between devices and between temperatures. The threshold voltage increases with decreasing temperature until below 150 K, when the threshold voltage variation becomes very large. Many devices have similar low field traces. There is no temperature trend for the magnitude of conduction, but the threshold voltage has a temperature trend. For devices tested at the same temperature, the threshold voltage was similar for temperatures ranging 300 K to 150 K.

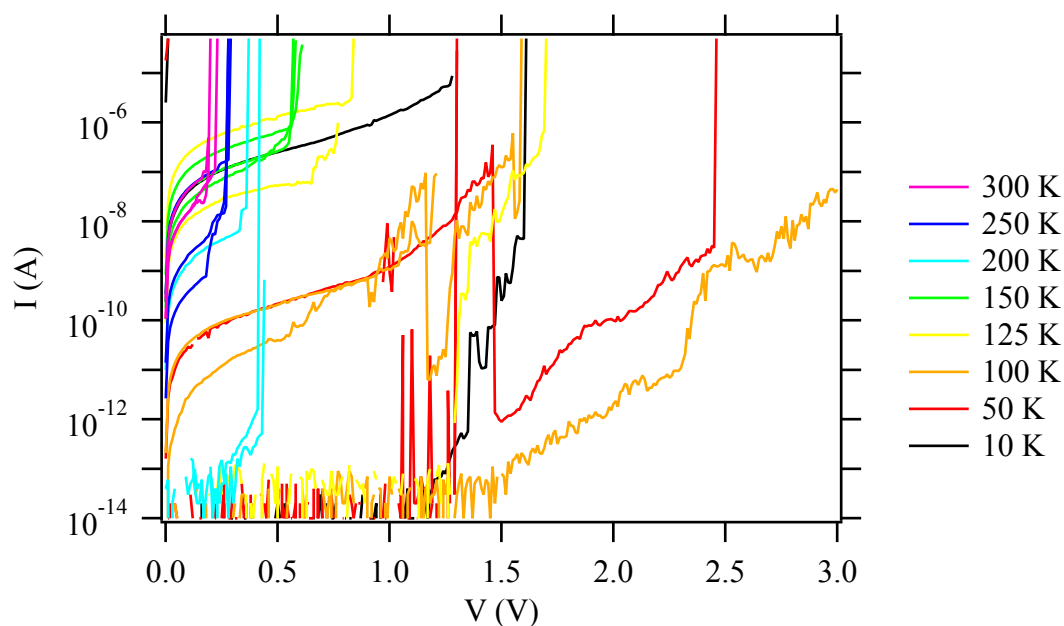


**Figure 4.10** First write traces for fresh Ag-only devices from 300 K to 10 K.

The Ag-only devices were written a second time, which may be more indicative of the repeat performance of the device. The writes were stopped at compliance current 50  $\mu\text{A}$ . The second write traces are shown in Figure 4.11. The threshold voltage of the 300 K devices is more consistent than the first write. The trend of increased threshold voltage with reduced temperatures continues down to 125 K. Threshold voltage was consistent between devices measured at the same temperature from 300 K to 200 K. At 150 K and lower, the threshold voltages of devices measured at the same temperature do not match.

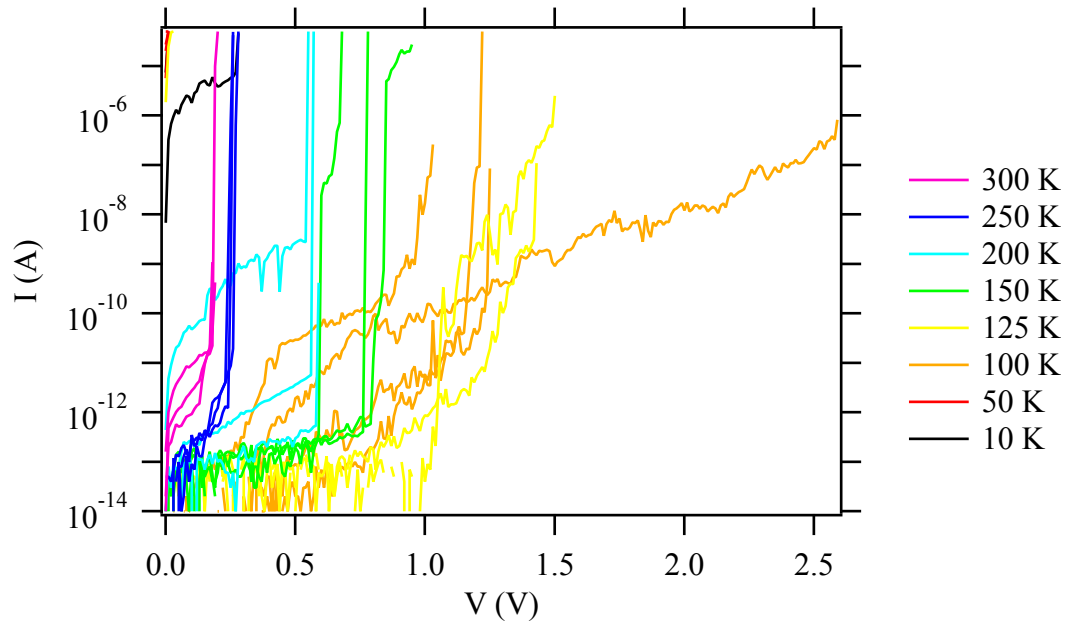


**Figure 4.11** Second write traces for fresh Ag-only devices from 300 K to 10 K.

#### 4.4.2 Threshold Voltage Characteristics of Ag-Only Write Traces for Fresh Devices

The threshold voltages of first and second write traces were gathered and analyzed. Figure 4.12 shows the threshold voltages of the first and second writes of Ag-only devices from 10 K to 300 K. At 300 K and 250 K, the first and second write threshold voltages match. At 200 K and 150 K, the second write threshold voltage is higher than the first write threshold voltage. At 125 K and below, there was large variation in threshold voltage and the presence of device shorting.

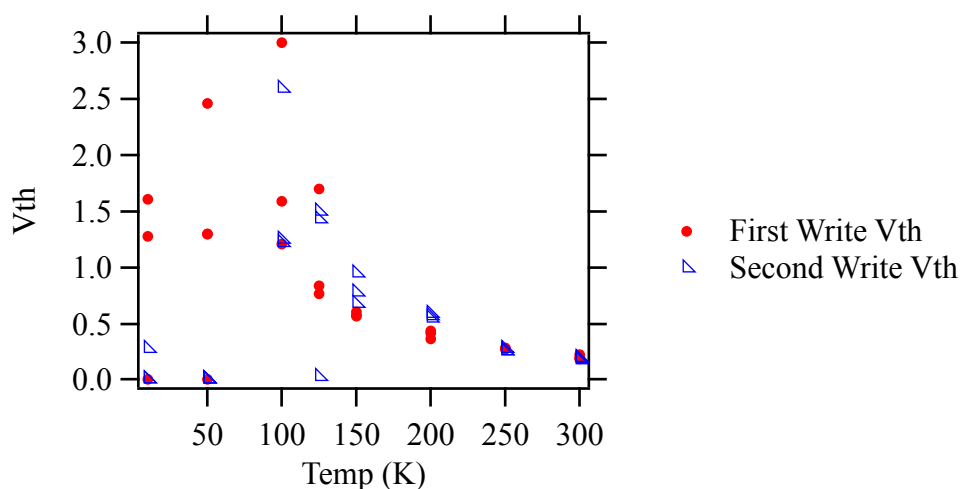


**Figure 4.12** Threshold voltages of fresh Ag-only first and second writes.

To determine if the Ag-only fresh device threshold voltage has Arrhenius thermally activated performance, the natural log of conductance at threshold was graphed against  $1/T$ , shown in Figure 4.13. Conductance at threshold is defined as  $50 \mu\text{A} / V_{\text{th}}$ . The results are linear from 300 K to 200 K. Below 200 K, the result was not linear.

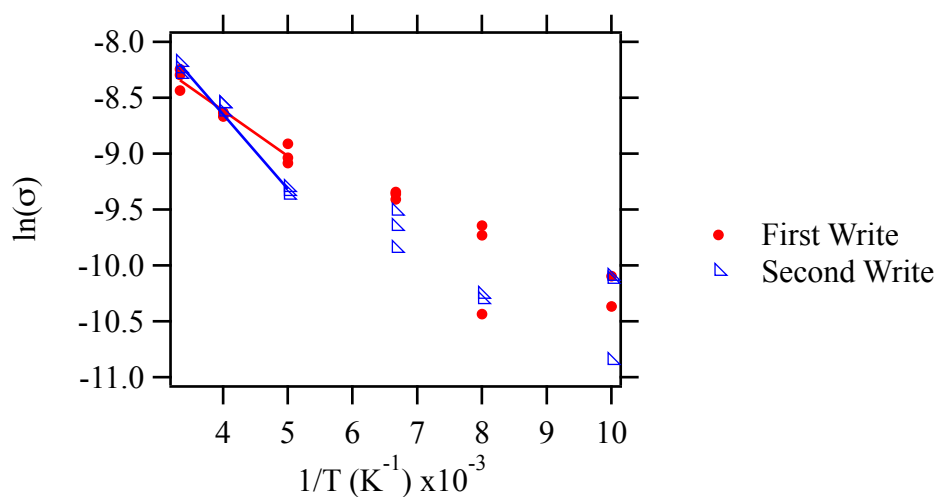


**Figure 4.13** Arrhenius plot of conductance at threshold for Ag-only fresh devices.

The calculated Arrhenius activation energy for the first write from 300 K to 200 K is  $0.035 \text{ eV} \pm 0.003 \text{ eV}$ . The second write calculated Arrhenius activation energy is  $0.057 \text{ eV} \pm 0.003 \text{ eV}$ .

#### 4.5 Ag+SnSe Switching Device Write Characteristics – Devices Retested Across Temperatures

In this section, the current-voltage traces of Ag+SnSe devices that were retested across temperatures and the fresh devices are presented. The IV characteristics are transformed using the known ion-conduction mechanisms of Butler-Volmer electrode redox and of Mott-Gurney ion hopping. Additionally, the write threshold voltage characteristics are modeled.

##### 4.5.1 IV Traces of Ag+SnSe Ion-Conducting Ge<sub>32</sub>Se<sub>68</sub> Devices

The write IV traces of Ag+SnSe device #1 are shown in Figure 4.14. The writes were stopped at compliance current 50  $\mu$ A. The magnitude of the conduction goes down with reduced temperature from 300 K down to 200 K. At 150 K, the magnitude becomes uncertain. The threshold voltage trends up as temperature is reduced from 300 K to 125 K. Traces are not shown below 100 K because the device shorted.

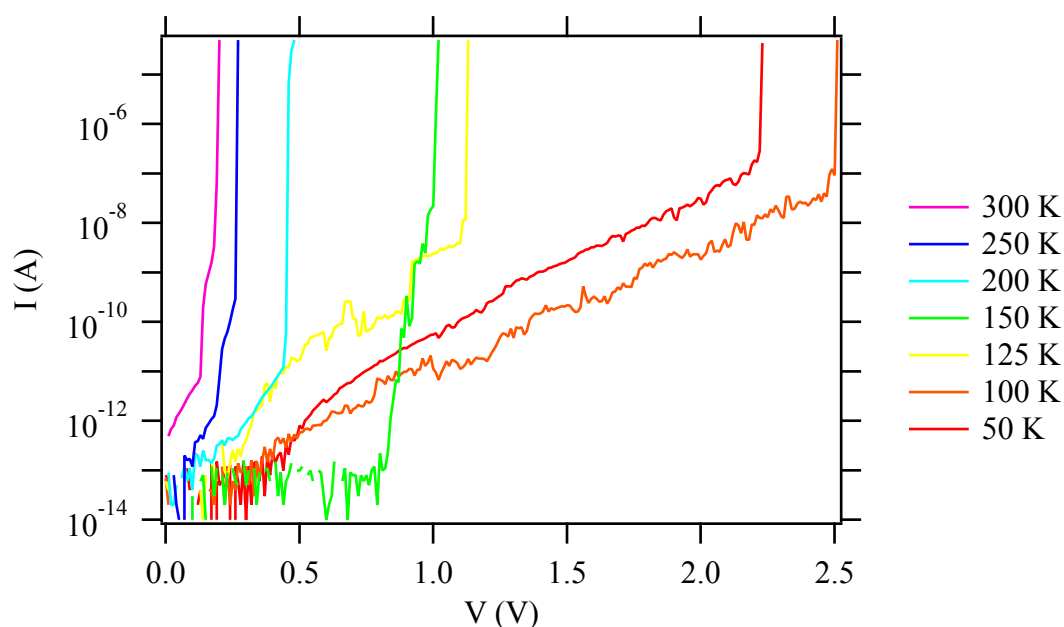


**Figure 4.14** IV traces of 50  $\mu$ A write for Ag+SnSe switching device #1 retested across temperatures.

The Ag+SnSe device #2 write traces are shown in Figure 4.15. The device was shorted below 100 K.

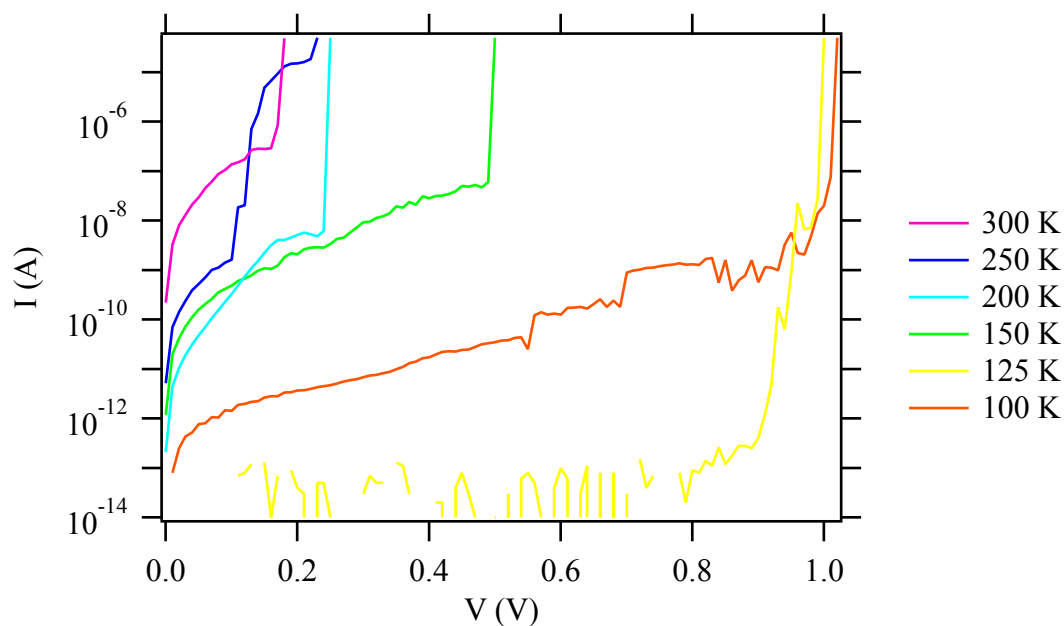


**Figure 4.15** IV traces of 50  $\mu$ A write for Ag+SnSe switching device #2 retested across temperatures.

The write traces for Ag+SnSe device #3 are shown in Figure 4.16. The device was shorted below 100 K.

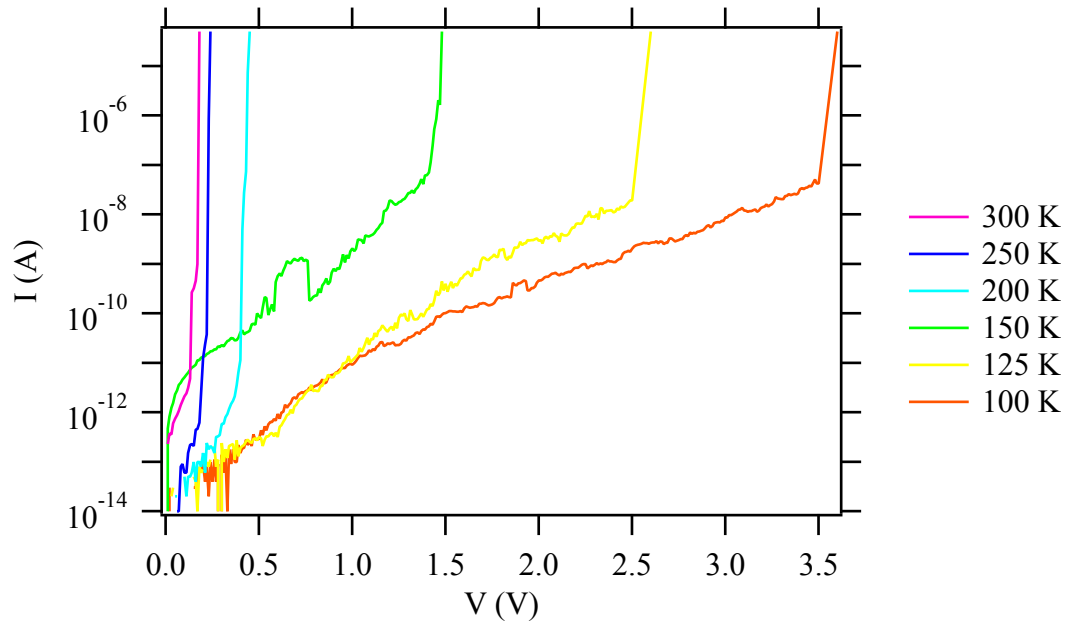


**Figure 4.16** IV traces of 50  $\mu$ A write for Ag+SnSe switching device #3 retested across temperatures.

#### 4.5.2 Layout Plot of IV Write Traces of Ag+SnSe Devices Retested at Each Temperature

To visually characterize the variations between devices, a layout plot showing the write traces of all three Ag+SnSe devices at each temperature is given in Figure 4.17.

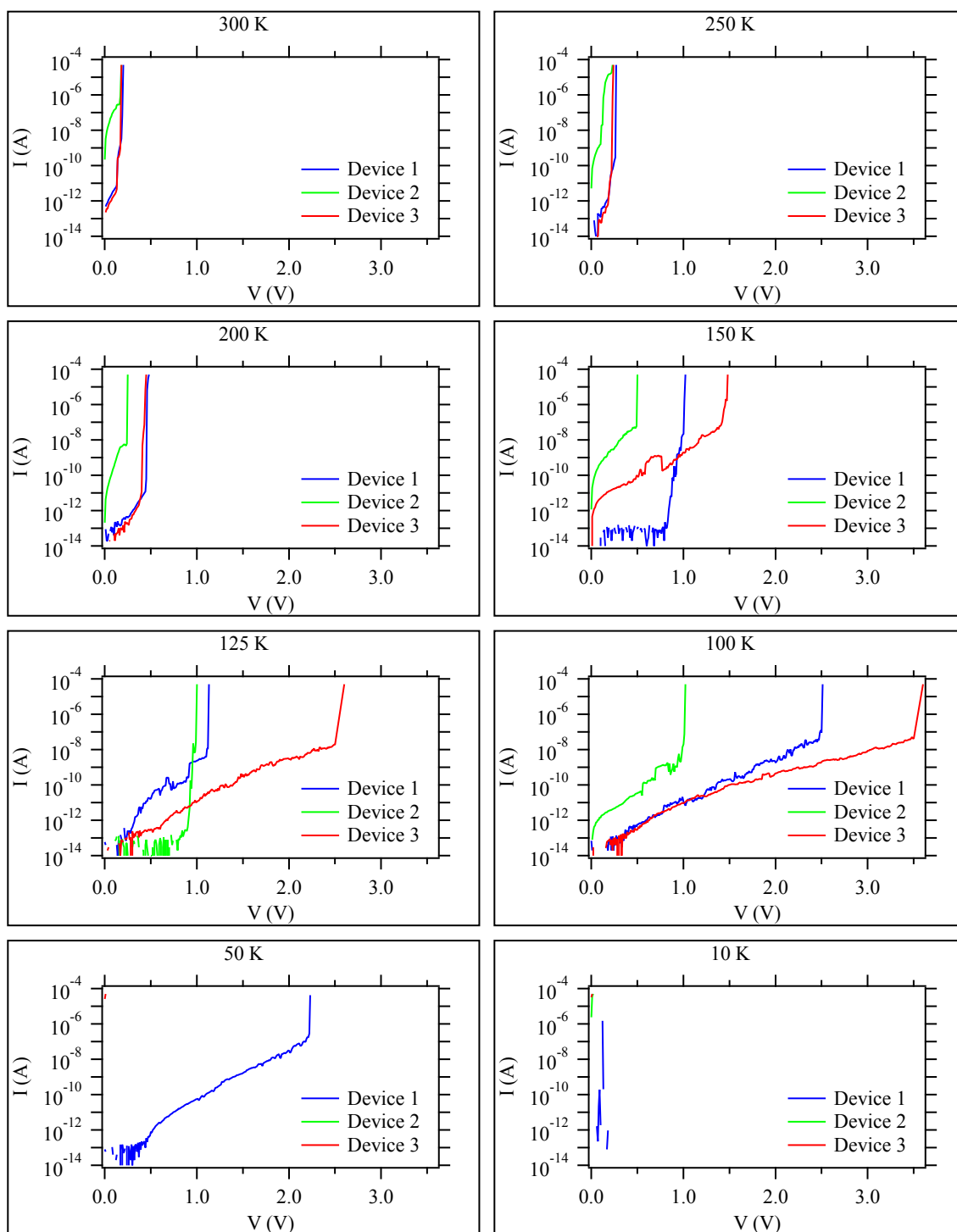


**Figure 4.17** Layout Plot of IV Write Traces of Ag+SnSe Devices Retested at Each Temperature

#### 4.5.3 Ion-Conduction Mechanisms of Ag+SnSe Devices Retested at Each Temperature

The I-V traces of the Ag+SnSe devices retested at each temperature were investigated to determine if there is linear performance at low fields and exponential performance at high fields. The result is that none of the traces were linear at low fields, while several temperatures had exponential performance at high fields. Table 4.5 lists the devices and temperatures that had high field exponential performance.

**Table 4.5**      **Temperatures where Ag+SnSe Devices Retested at Each Temperature Had Exponential Performance**

Device	Temperature
1	300 K
	200 K
	100 K
2	200 K
	150 K
	100 K
3	300 K
	200 K
	150 K
	125 K
	100 K

Linear equation fitting was performed to the  $\ln(I)$  vs  $V$  transformations. The equation to determine Mott-Gurney hopping distance is shown in Eqn. 4.5. The hopping distance,  $a$ , uses the slope of the  $\ln(I)$  vs  $V$  line,  $b$ .

$$a = 2b \cdot \text{thickness} \cdot kT/q \quad (4.5)$$

The calculated hopping distances for each trace are shown in Figure 4.18. The general trend is that hopping distance is increasing with temperature. Realistically, the values, especially at the higher temperatures do not seem to make sense. For example, the device 2 at 200 K has ions that hop about 400 Å, which is farther than the 300 Å

memory layer. While the hopping distances may not be true to reality, they serve to illustrate the decreasing ion mobility with reduced temperature.

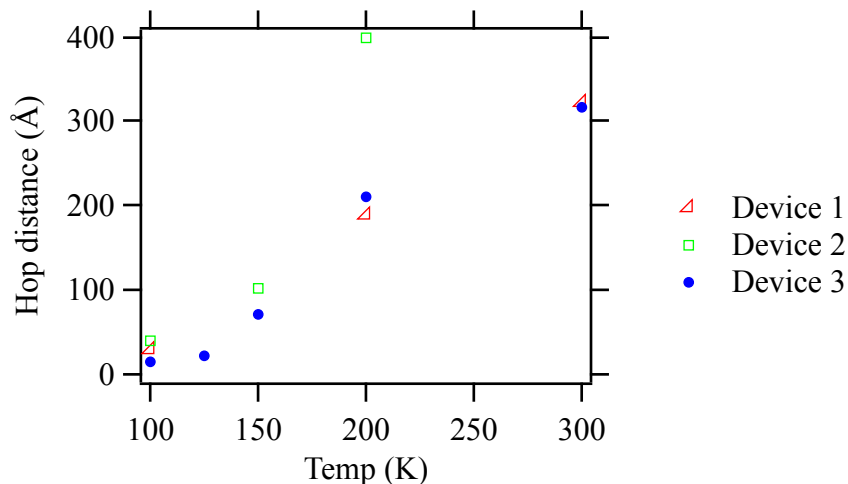


**Figure 4.18** Calculated MG ion hopping distance for Ag+SnSe devices retested at each temperature.

#### 4.5.4 Threshold Voltage Characteristics of Ag+SnSe Devices Retested at Each Temperature

The threshold voltage (voltage when current is 50  $\mu$ A) results for the three Ag+SnSe devices that were retested across temperatures are shown in Figure 4.19. Variation between devices is very low for 300 K and 250 K. There is a divergence at 200 K and below.

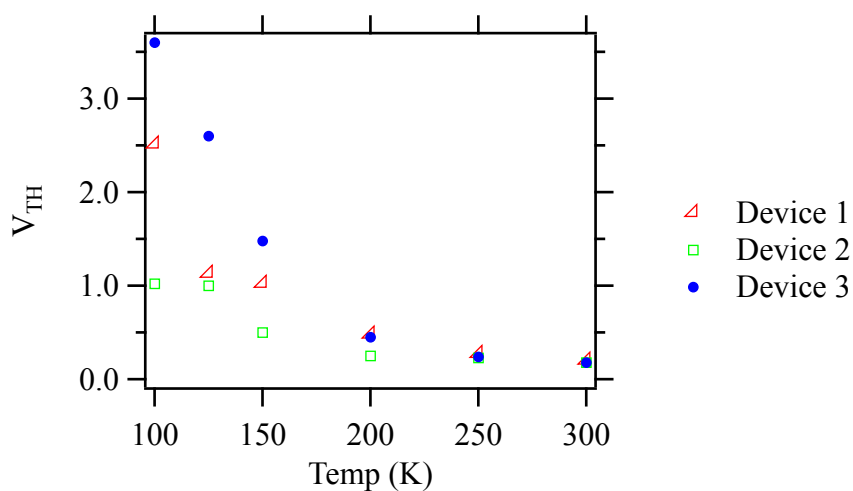


**Figure 4.19** Threshold voltages of Ag+SnSe devices retested across temperatures.

To calculate the activation energy at threshold voltage, the natural log of conductance at threshold was plotted versus inverse temperature as shown in Figure 4.20. For temperatures 300 K down to 150 K, the result was linear, indicating Arrhenius-type activation. Below 150 K, results were randomly distributed. Devices 1 and 3 had similar activation slopes, while Device 2 had a lower slope, indicating lower activation energy.

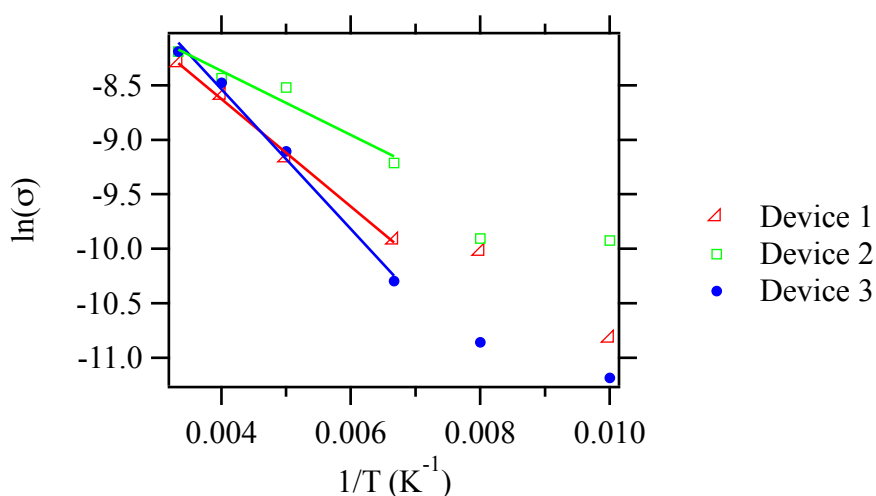


**Figure 4.20** Arrhenius plot of conductance at threshold for Ag+SnSe devices retested across temperatures.

Activation energies from 150 K to 300 K of the three Ag+SnSe devices retested across temperatures are shown in Table 4.6. The variation between devices is quite large, possibly due to process defectivity or interface issues.

**Table 4.6 Activation energy for conductance at threshold for Ag+SnSe devices retested across temperatures**

Device	Temperature Range	Activation Energy
1	150-300 K	0.043 eV
2	150-300 K	0.025 eV
3	150-300 K	0.055 eV

#### **4.6 Ag+SnSe Switching Device Write Characteristics – Fresh Devices at Each Temperature**

Three devices were reserved at each temperature to be tested for the first time. As previously mentioned, these devices were written, erased, and then rewritten. Write traces are presented for the first write and the second write. The threshold voltages are gathered and analyzed for Arrhenius thermal activation dependency.

##### 4.6.1 Write Traces of Ag+SnSe Fresh Devices

In Figure 4.21, the first write traces for the untested devices are shown from 300 K down to 10 K. The writes were stopped at compliance current 50  $\mu$ A. Similar to the Ag-only devices, there was a huge variation in magnitude of conduction during write. Also, there appears to be a similar smooth low field response compared to the Ag-only devices, though not all devices had this performance. The threshold voltage increases with decreasing temperature for the entire range, although there were a couple of instances when this was not true.

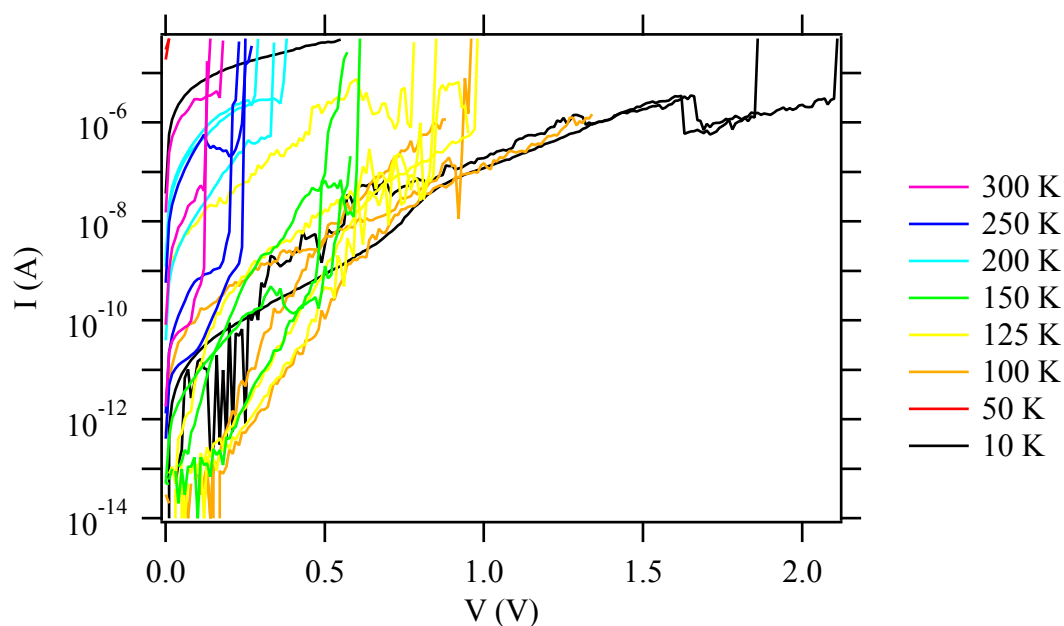


**Figure 4.21** First write traces for fresh Ag+SnSe devices from 300 K to 10 K.

The second write traces for the Ag+SnSe devices are shown in Figure 4.22. The writes were stopped at compliance current  $50 \mu\text{A}$ . Many of the devices retained the smooth low field performance on the second write, while most of the Ag-only devices became noisy after the first write. The variation in the threshold voltage between devices is much larger on the second write than the first. The difference in conduction is orders of magnitude between devices.

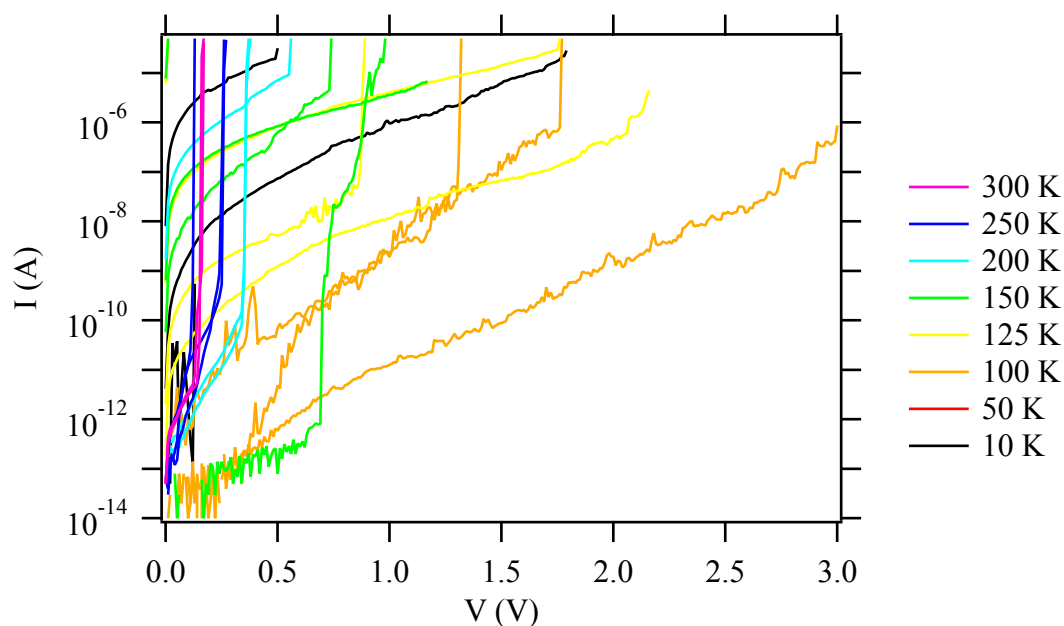


**Figure 4.22** Second write traces for fresh Ag+SnSe devices from 300 K to 10 K.

#### 4.6.2 Threshold Voltage Characteristics of Ag+SnSe Write Traces for Fresh Devices

The threshold voltages of first and second write traces were gathered and analyzed. Figure 4.23 shows the threshold voltages of the first and second writes of Ag-only devices from 10 K to 300 K. At 150 K and below, there was large variation in threshold voltage and the presence of device shorting.

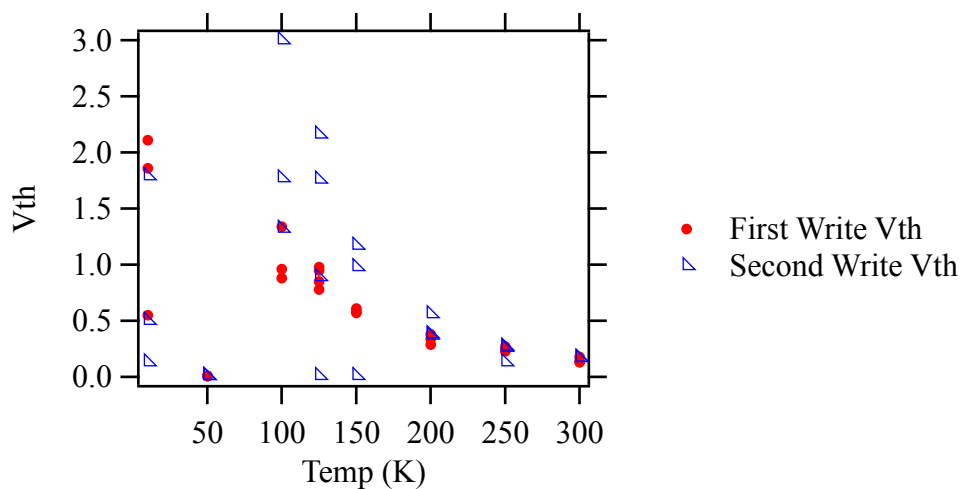


**Figure 4.23** Threshold voltages of fresh Ag+SnSe first and second writes.

To determine if the Ag-only fresh device threshold voltage has Arrhenius thermally activated performance, the natural log of conductance at threshold was graphed against  $1/T$ , shown in Figure 4.24. Conductance at threshold is defined as  $50 \mu\text{A} / V_{\text{th}}$ . A linear fit was performed from 300 K to 200 K, as was done with the Ag-only fresh devices. There was more device-to-device variation in the threshold voltages of Ag+SnSe devices compared to the Ag-only devices. The calculated activation energies reflect the variation with two to four times more uncertainty.

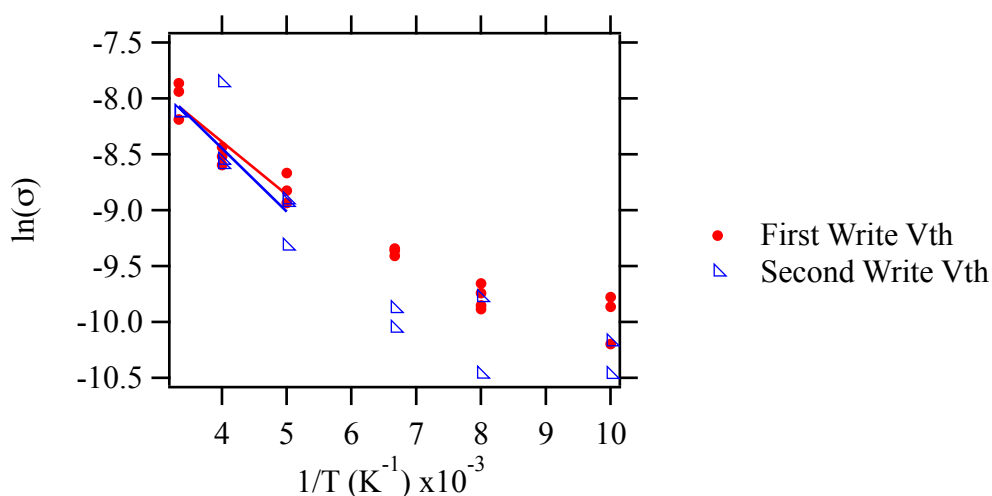


**Figure 4.24** Arrhenius plot of conductance at threshold for Ag+SnSe fresh devices.

The calculated Arrhenius activation energy for the first write from 300 K to 200 K is  $0.040 \text{ eV} \pm 0.007 \text{ eV}$ . The second write calculated Arrhenius activation energy is  $0.049 \text{ eV} \pm 0.011 \text{ eV}$ .

#### 4.7 Post Write Resistance Characteristics

Resistance was measured after each write by sweeping the voltage from 0 to 20 mV in steps of 1 mV. If the current reached  $50 \mu\text{A}$  before 20 mV was reached, the read was stopped at compliance to limit the chance of altering the resistance state. Resistance

was determined by taking the inverse of the slope of the 20 mV IV trace. The post write resistance and post erase resistance results for the devices that were retested across temperatures are shown in Figure 4.25. Three Ag-only devices and three Ag+SnSe devices were retested at each temperature. Written resistance ranges from a few hundred ohms to a several thousand ohms. Low temperatures had generally lower resistance, possibly because of top electrode breakage that causes shorting and failure to erase.

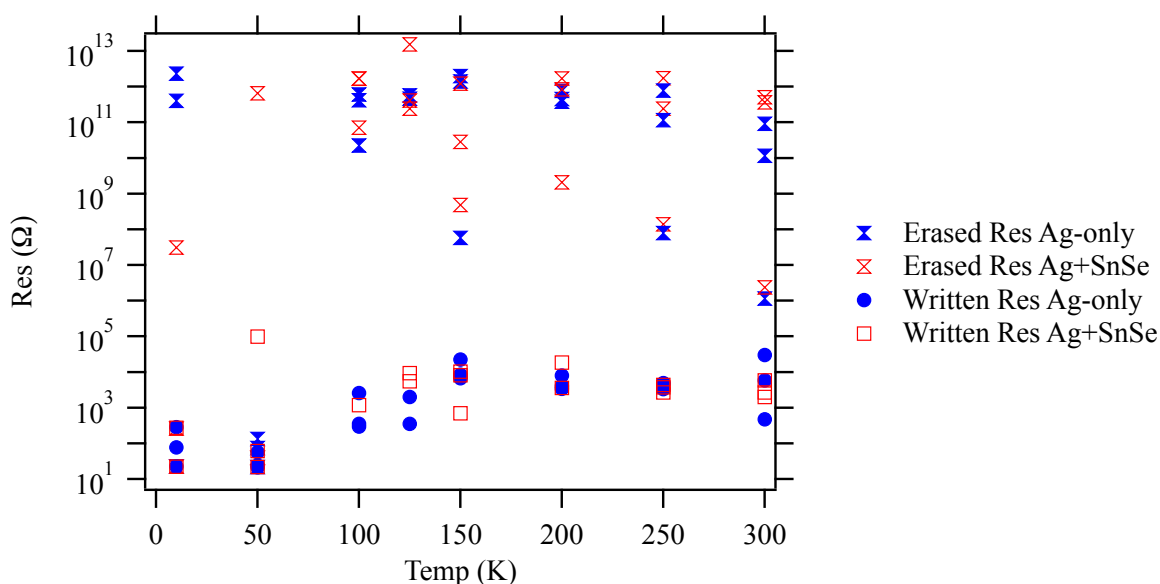


**Figure 4.25 Post write and erased resistance of devices retested across temperatures**

For devices tested fresh, an initial forming write was performed to 50  $\mu\text{A}$  compliance; a resistance readout (20 mV sweep), an erase, then a second write and readout were performed. The resistances of the Ag-only devices are shown in Figure 4.26. The resistances did not have a temperature trend. Erase did not occur at 50 K and 10 K, possibly due to top electrode breakage and shorting. Additionally, the low mobility of ions at very low temperatures could be to blame.

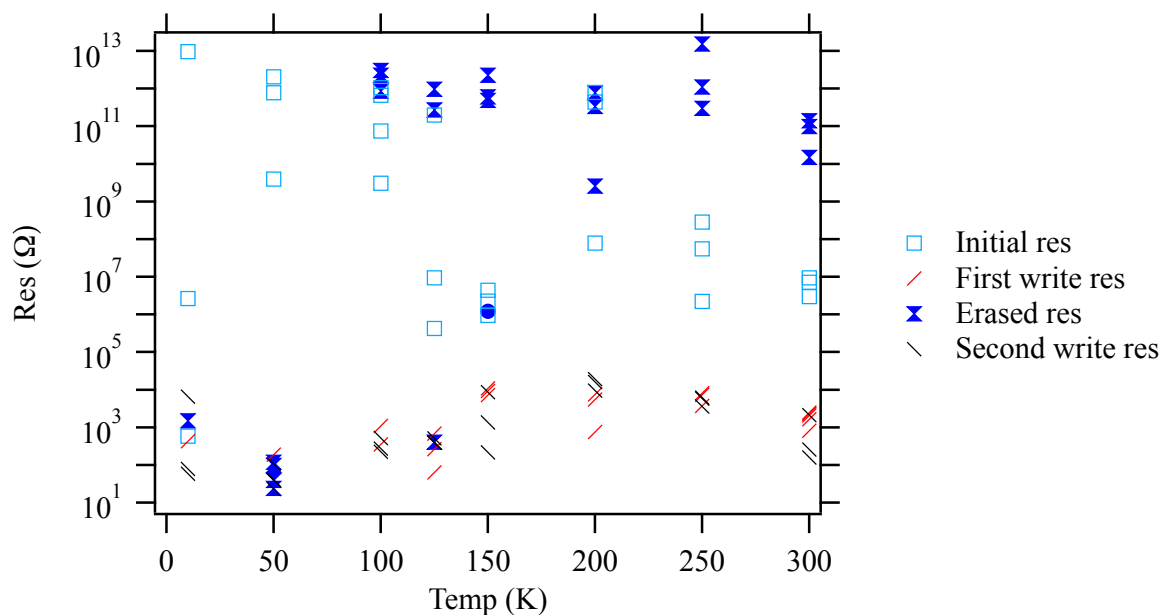


**Figure 4.26** Post write and erase resistances for “fresh” Ag-only devices.

The resistances of the fresh Ag+SnSe devices are shown in Figure 4.27. The same testing procedures were used on Ag+SnSe devices as those used for Ag-only devices. There was not a clear temperature trend in the written resistances. Erase was less reliable at 150 K and below.

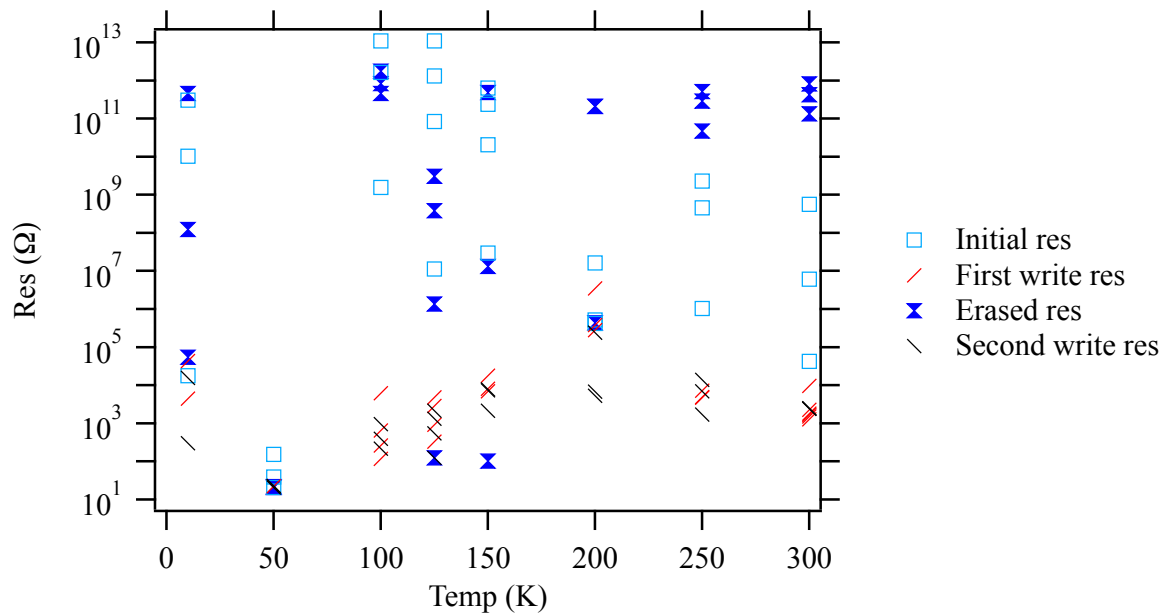


**Figure 4.27** Post write and erased resistances for “fresh” Ag+SnSe devices

## 4.8 Conclusion of Writing Characteristics

To conclude this chapter on writing characteristics, it has been shown that both Ag-only and Ag+SnSe ion-conducting devices with  $\text{Ge}_{32}\text{Se}_{68}$  memory layer are capable of ion conduction and sudden writing that is attributed to metal bridging the memory layer gap. Devices were tested both “fresh” at each temperature and retested at each temperature. Write traces were analyzed for both electron and ion-conduction mechanisms. Additionally, the threshold voltage and resistance characteristics were investigated.

### 4.8.1 Conduction Mechanisms

None of the electron-conduction mechanisms fit to the write traces. For the Ag-only devices, the Butler-Volmer and Mott-Gurney ion-hopping mechanisms did not fit to the write traces consistently. However, for the Ag+SnSe devices, many measurements had exponential current traces that fit to the high-field approximations for BV and MG.

### 4.8.2 Threshold Voltage Characteristics

The threshold voltages were compared for Ag-only and Ag+SnSe devices retested at each temperature and for devices tested fresh. Threshold voltage is defined at the voltage when compliance current is achieved. In the case of these experiments, the compliance current is  $50\ \mu\text{A}$ . The threshold voltage was investigated for Arrhenius activation by graphing the natural log of the conductance at threshold against  $1/T$ . Conductance at threshold is defined as  $50\ \mu\text{A} / V_{\text{th}}$ .

#### 4.8.2.1 Devices Retested at Each Temperature

Figure 4.28 overlays the threshold voltages of both devices. As temperature is reduced, variation between device threshold voltages increases.

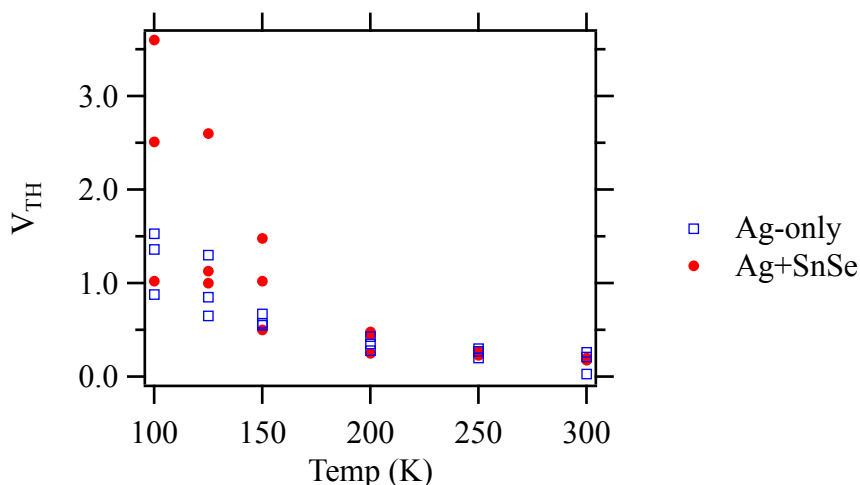


**Figure 4.28** Overlay of threshold voltage for Ag-only and Ag+SnSe devices retested across temperatures.

The activation energies of conductance at threshold for Ag-only and Ag+SnSe devices are summarized in Table 4.7.

**Table 4.7** Summary of Arrhenius Activation Energy of Conductance at Threshold for Devices Retested Across Temperatures.

Device Type	Device No.	Temperature Range	Activation Energy
Ag+SnSe	1	150-300 K	0.043 eV
	2	150-300 K	0.025 eV
	3	150-300 K	0.055 eV
Ag-only	1	100-200 K	0.012 eV
		200-300 K	0.037 eV
	2	100-250 K	0.025 eV

#### 4.8.2.2 Devices Tested Fresh at Each Temperature

Threshold voltages of all fresh devices are shown in Figure 4.29.

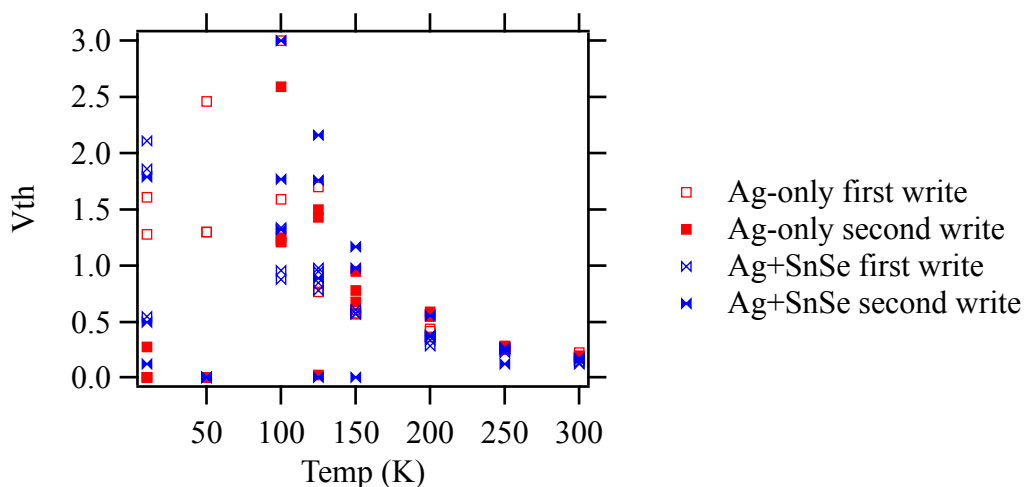


**Figure 4.29** Overlay of threshold voltages for all devices tested fresh at each temperature.

The activation energies of the fresh devices are summarized in Table 4.8. Due to the variation, it is not possible to conclude that Ag-only and Ag+SnSe devices have different activation energies for conductance at threshold. Since the activation energies are in the same order of magnitude, it can be concluded that adding the SnSe layer did not strongly impact the operation of devices.

**Table 4.8** Summary of Arrhenius Activation Energy of Conductance at Threshold for Devices Tested Fresh at Each Temperature Calculated from 200 K to 300 K.

Device Type	Write	Activation Energy
Ag-only	First	0.035 eV $\pm$ 0.003 eV
	Second	0.057 eV $\pm$ 0.003 eV
Ag+SnSe	First	0.040 eV $\pm$ 0.007 eV
	Second	0.049 eV $\pm$ 0.011 eV

At temperatures below 200 K, the slope of the Arrhenius plots flattened out, which effectively means that activation energy is reducing for lower temperatures. If the Arrhenius activation energy was constant down to low temperatures, then the threshold voltage would have been higher than it was.

#### 4.8.3 Resistance Characteristics

There was no temperature trend for resistances of the devices retested at each temperature or the fresh devices. There was large variation between written resistance within a given temperature. Temperatures below 150 K did not have reliable erases.

## CHAPTER 5: ERASE CHARACTERISTICS

### 5.1 Summary

In the previous chapter, the write characteristics of ion-conducting devices with the two configurations of Ag-only and Ag+SnSe with  $\text{Ge}_{32}\text{Se}_{68}$  memory layer were modeled to known ion-conducting mechanisms. In this chapter, the erase characteristics are investigated.

### 5.2 Experimental Procedure for Erase

To erase a device in low resistance state, a voltage sweep was performed in reverse polarity, with negative voltage on the top electrode. The sweep was performed in 10 mV steps. Typically, current increases up to a maximum, then there is a sudden decrease of several orders of magnitude. Once that decrease occurs, the erase is manually stopped. The reason for performing this manual operation is due to inconsistencies in erase voltage and current between devices. For some devices, very high current or high voltage was needed to erase, whereas other devices would break down under those conditions. By charting erase current on a logarithmic plot, it is visible when the erase takes place due to the sudden step function decrease in current. The measurement is manually stopped once that occurs.

#### 5.2.1 Procedure for Devices Retested at Each Temperature

For devices retested at each temperature, an initial channel forming write and erase was performed first at temperature 300 K. Next, the device was subjected to the

electrical sequence shown in Table 5.1. Then, the temperature was lowered to the next level. The purpose of Erase 1 is to confirm and force the device off. There were cases in the past that devices appeared to return to low resistance after temperature change. It is possible that the previous erase was not effective, or there may be issues with the measurement system. Erase 1 ensures that the device is fully erased before writing. For this chapter, the Erase 2 is investigated.

**Table 5.1 Electrical Sequence for Devices Retested at Each Temperature**

<b>Function</b>	<b>Notes</b>
1. Erase 1	Negative voltage sweep. 10 mV steps. Manually stop after device switches off or confirmation that device is already erased.
2. Read 1	20 mV max voltage in steps of 1 mV, 50 $\mu$ A compliance current.
3. Write	Max limit of 50 $\mu$ A compliance current. 10 mV steps.
4. Read 2	20 mV max voltage in steps of 1 mV, 50 $\mu$ A compliance current.
5. Erase 2	Negative voltage sweep. 10 mV steps. Manually stop after device switches off.

### 5.2.2 Procedure for Devices Tested for the First Time at Each Temperature

For devices that were tested ‘fresh’ at each temperature, a forming write was performed, then erase, and then a second write. The single erase is investigated for these devices. Table 5.2 shows the electrical sequence performed on devices that are tested for the first time at each temperature.

**Table 5.2 Sequence of Testing for Fresh Switching Devices**

<b>Function</b>	<b>Notes</b>
1. Read 1	20 mV max voltage in steps of 1 mV, 50 $\mu$ A compliance current.
2. Write 1	Max limit of 50 $\mu$ A compliance current. 10 mV steps.
3. Read 2	20 mV max voltage in steps of 1 mV, 50 $\mu$ A compliance current.
4. Erase	Negative voltage sweep. 10 mV steps. Manually stop after device switches off.
5. Read 3	20 mV max voltage in steps of 1 mV, 50 $\mu$ A compliance current.
6. Write 2	Max limit of 50 $\mu$ A compliance current. 10 mV steps.
7. Read 4	20 mV max voltage in steps of 1 mV, 50 $\mu$ A compliance current.

### 5.3 Erase Traces for Devices Retested at Each Temperature

The erase traces for devices retested across temperatures are shown in this section. The purpose of retested devices across temperatures is to eliminate device-to-device variation from the analysis.

#### 5.3.1 Erase Traces for Ag-Only Devices

Three Ag-only ion-conducting, switching devices were tested across temperatures. The erase traces for the first device are shown in Figure 5.1. Even though a negative voltage was applied to the top electrode, the graph shows positive values for the purpose of plotting on a log scale. The first temperature tested was 300 K, then temperatures were stepped down.

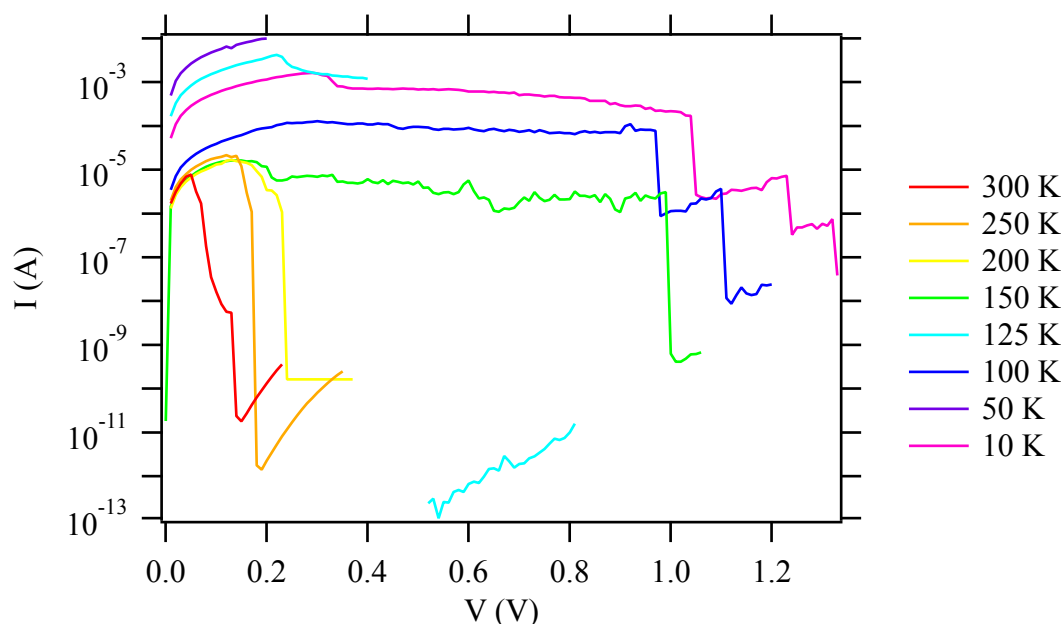


**Figure 5.1 Erase traces for Ag-only device 1 retested across temperatures.**

One trend noticeable from the plot is that the erase voltage is increasing as the temperature is reduced for temperatures 300 K to 200 K. Below that, there is less certainty. The 150 K trace has a higher erase voltage than the 125 K, which is unexpected due to lower ion mobilities at lower temperatures. At temperatures 100 K and 50 K, there is the possibility of multiple filaments, as the current steps down a few times.

One notable feature for 150 K and below is nearly constant current as voltage is continually increased. One idea for why is that silver ion mobility is low, so resistance is increasing gradually with increased voltage.

The resistance of Ag-only device 1 at low fields before completion of the erase looks comparable for temperatures 300 to 150 K. Below 150 K, the conduction is higher. The higher conduction at low temperatures may be due to top electrode breakage causing shorts from top electrode to bottom electrode or possibly low Ag-ion mobility.

The erase traces for Ag-only device 2 are shown in Figure 5.2. Similarly to device 1, the low temperatures have very high conduction. In the cases of 10 K and 50 K, the erase did not occur. The voltage where the erase occurred did not trend with temperature for device 2. The 300 K measurement did have the lowest erase voltage, but 200 K erased at a lower voltage than 250 K. Erase voltages were much higher for 150 K and below.

Similarly to device 1, at 150 K and below, there is a region of stable then decreasing current with increased voltage. For device 2, the current decreases with increased voltage at a higher rate compared to device 1.

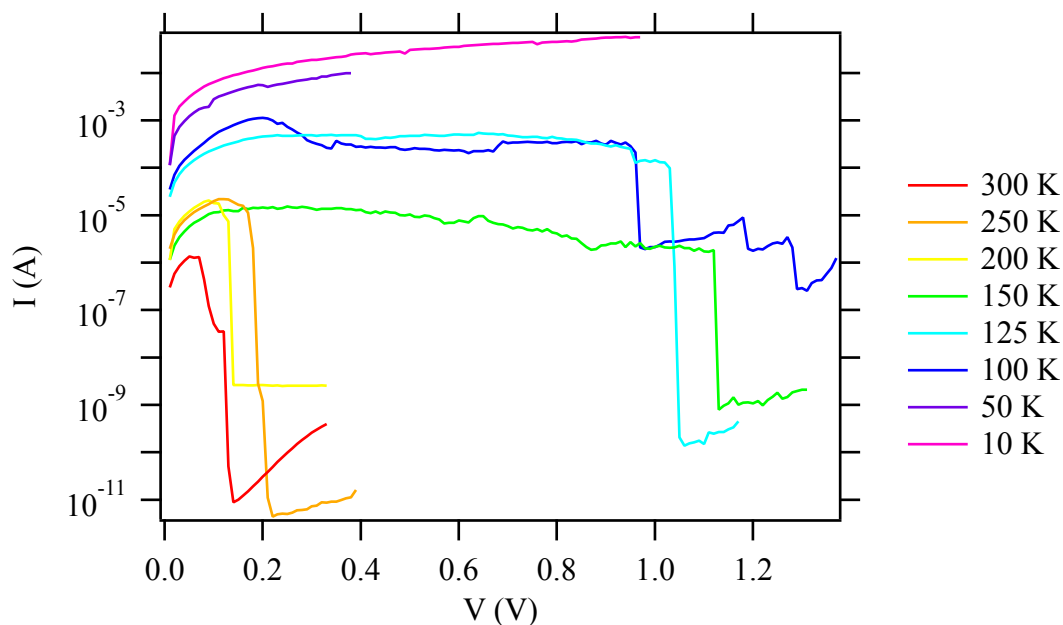


**Figure 5.2 Erase traces for Ag-only device 2 retested across temperatures.**

In Figure 5.3, the erase traces for Ag-only device 3 are shown. The device is erasing at higher voltage than devices 1 and 2. In addition, the conduction is higher than the other two devices. There is no temperature trend in erase voltage or in conduction.

There is the possibility of multiple filaments for several temperatures, as there are multiple steps down.

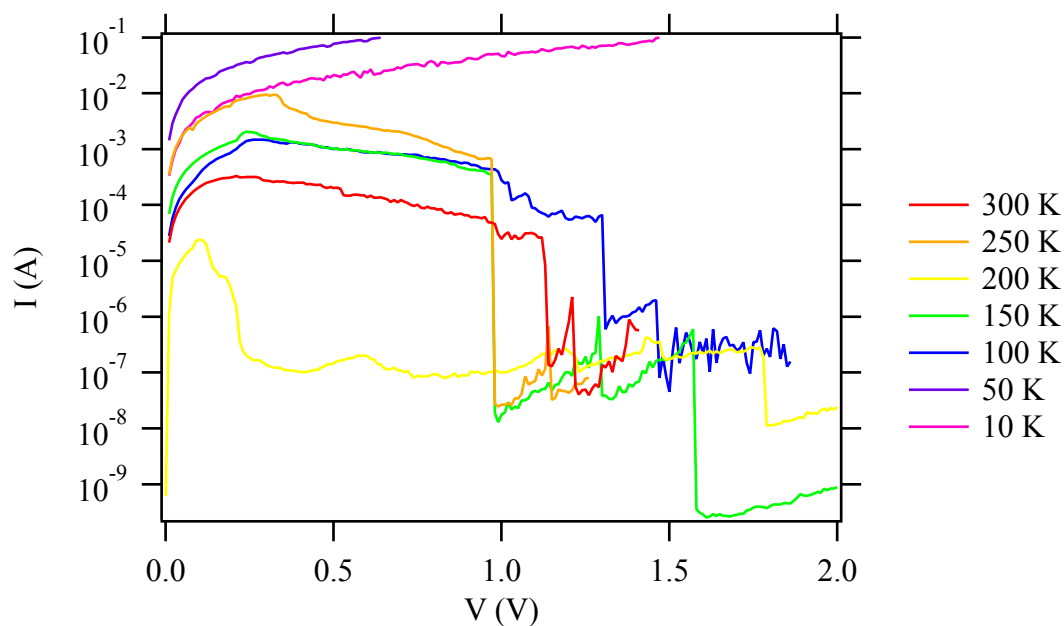


**Figure 5.3 Erase traces for Ag-only device 3 retested across temperatures.**

### 5.3.2 Erase Traces for Ag+SnSe Devices

For Ag+SnSe device 1, the erase traces are shown in Figure 5.4. There is not a temperature trend for conduction or erase voltage, other than that erase voltages are lower for 300 K to 150 K and higher below 150 K.

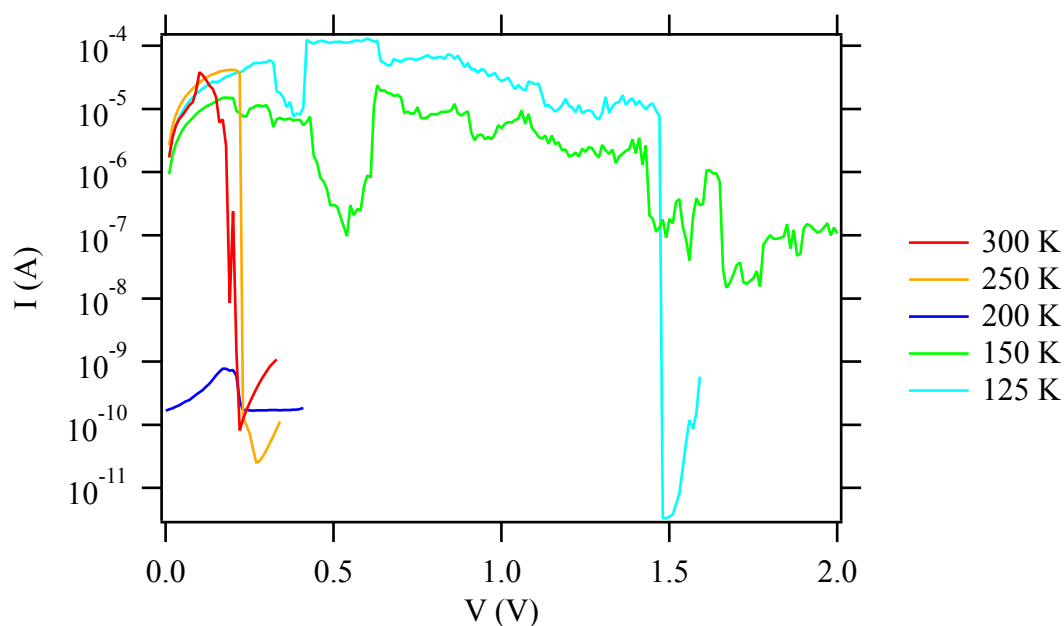


**Figure 5.4 Erase traces for Ag+SnSe device 1 retested across temperatures.**

Erase traces for Ag+SnSe device 2 are shown in Figure 5.5. Again, the erase voltage and conduction did not trend with temperature other than 100 K and lower have the highest conduction, and the erase voltage is higher for 150 K and below compared to above. For 300 K to 200 K, erase voltages are below 0.5 V. For below 200 K, erase voltages are above 1 V.

Similar to the Ag-only devices, there are regions of increasing voltage where the current either remains stable or decreases. For device 1, this occurs at 150 K and below. Erase did not occur for 50 K and 10 K.

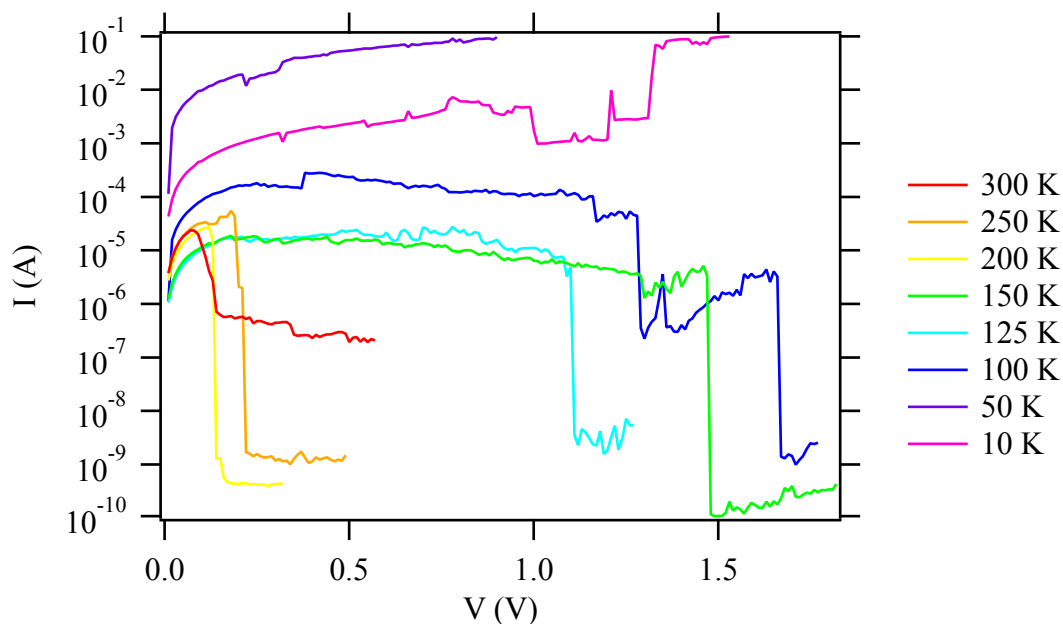


**Figure 5.5 Erase traces for Ag+SnSe device 2 retested across temperatures.**

Lastly, erase traces for Ag+SnSe device 3 are shown in Figure 5.6. There are fewer traces available than devices 1 and 2 due to shorting. The device was unable to be erased at 50 K and 10 K.

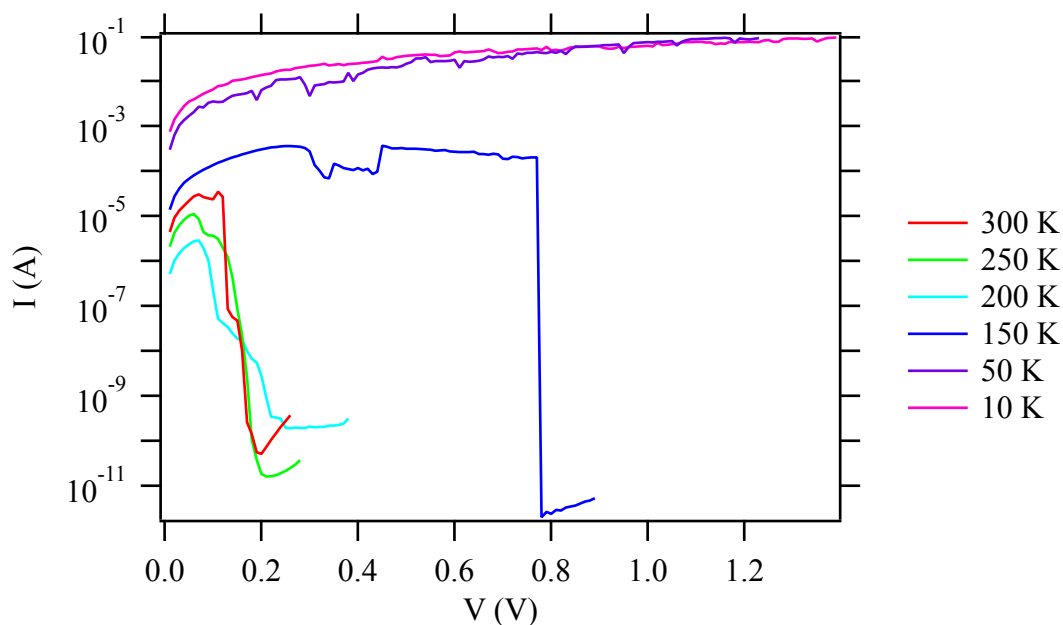


**Figure 5.6 Erase traces for Ag+SnSe device 3 retested across temperatures.**

### 5.4 Erase Traces of Devices Tested Fresh at Each Temperature

In this section, the erase traces of devices tested for the first time at each temperature are shown. The test eliminates variation introduced from cycling devices multiple times, but includes process/material variation between devices.

#### 5.4.1 Ag-Only Erase Traces

An overlay of all erases for Ag-only devices tested for the first time at each temperature is shown in Figure 5.7. There is quite a bit of device-to-device variation, but it is notable that the trends seen with the devices tested multiple times are still present. Higher temperatures have lower erase voltages in general, though there isn't a clear trend. Conduction was generally higher for lower temperatures, ending with shorting at the lowest temperatures. There are a few examples of possible multiple filaments erased, as evidenced by traces that had discrete steps down.

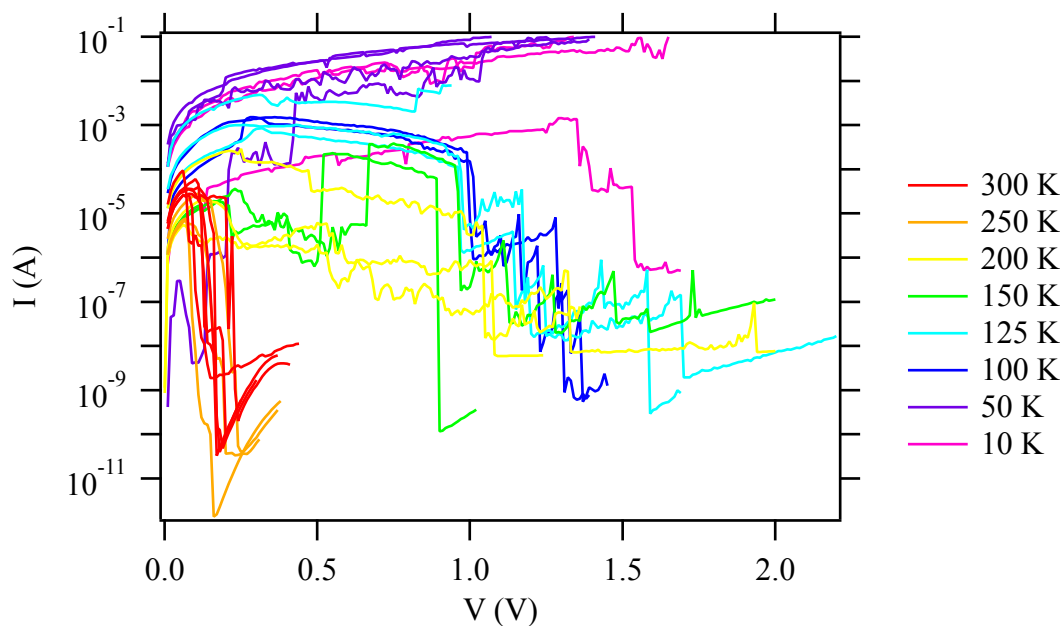


**Figure 5.7** Erase traces for fresh Ag-only devices at each temp.

### 5.4.2 Ag+SnSe Erase Traces

An overlay of all erases for Ag-only devices tested for the first time at each temperature is shown in Figure 5.8. Again, these devices have quite a bit of variation, but the same similar trends are present as with the Ag-only devices. Higher temperatures have lower erase voltages in general, though there isn't a clear trend. Conduction was generally higher for lower temperatures. Of particular interest, the 50 K temperature had the very highest conduction overall, with a clear shorting signature, while 10 K had a lot of noise, but no evidence of shorting.

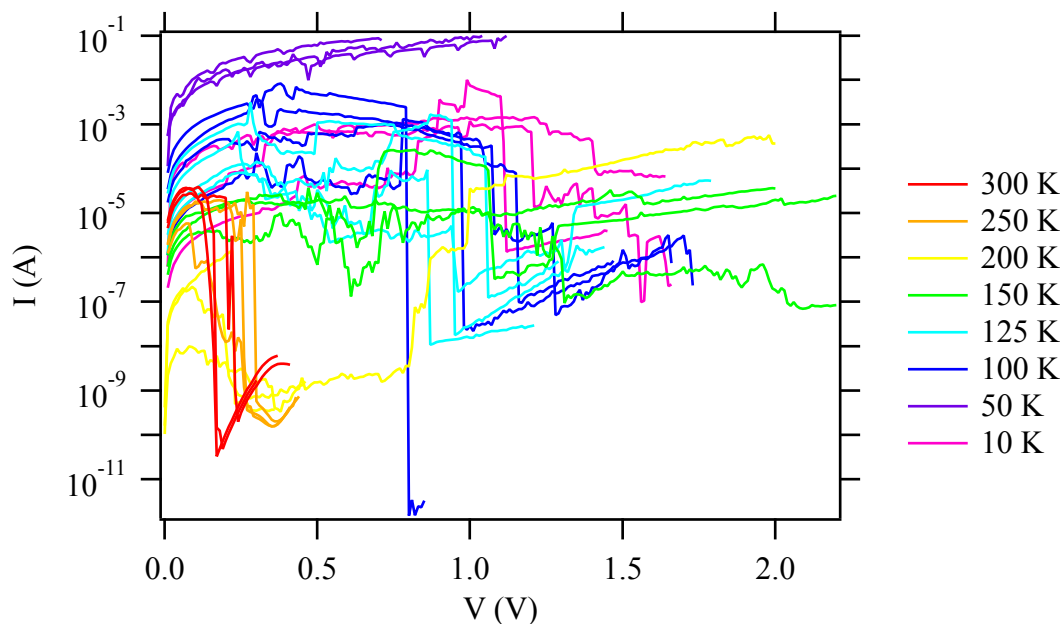


**Figure 5.8** Erase traces for fresh Ag+SnSe devices at each temp

### 5.5 Resistance Characteristics of Devices After Erase

After the erase operation, the resistance was measured to verify that the erase occurred. The same procedure was used on the post write resistance measurements. The voltage was swept from zero volts to 20 mV in steps of 1 mV. If the current reached 50  $\mu\text{A}$ , then the measurement automatically stopped on compliance.

For fresh devices, only one erase was performed; this erase was after the initial forming write. The resistance values of the fresh devices across temperatures are shown in Figure 5.9. The notable features are that at higher temperatures, from 200 to 300 K, the erase is more reliable. In other words, the resistance values are very high, essentially an open circuit. From 200 K and below, the erase does not always reliably occur. The Ag-only devices seem to have a better chance of erasing from 100 K to 200 K than the Ag+SnSe. At 50 K and below, there are shorts and a few examples of devices that erased.

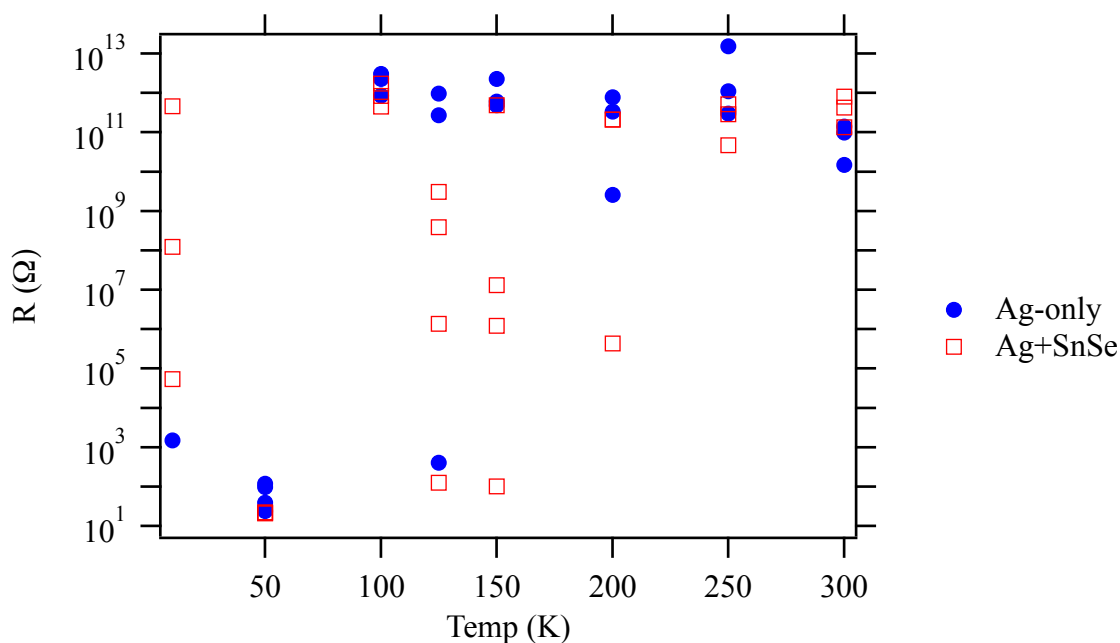


**Figure 5.9 Resistance values of fresh devices after erase across temperatures.**

### 5.6 Conclusion of Erase Characteristics

Overall, the erase traces between the Ag-only devices and the Ag+SnSe devices were similar, with lower erase voltages for the highest temperatures. The erase voltage did not precisely trend with temperature, possibly indicating disorder in the formation of the conductive path. In many cases, especially at lower temperatures, the current

gradually went down with increased voltage, instead of suddenly switching off, which occurred more frequently at the higher temperatures. The performance suggests lower ion conductivity at low temperatures.

## CHAPTER 6: CONCLUSION

### 6.1 Introduction

As computer memory requirements increase, the advantages of emerging memory devices such as Conductive-Bridge memory (CBRAM) become more significant. To implement this technology in a consumer product, several hurdles must be crossed. Reliability, speed, and long retention time are needed to compete with existing technologies, primarily NAND flash. Part of the challenge is fully characterizing the operation of the devices.

This work seeks to understand the mechanisms of electron conduction in the resistive ion-conducting material  $\text{Ge}_{32}\text{Se}_{68}$  and the mechanisms of electron and ion conduction in completed devices using Ag ions and stacked devices using SnSe material in addition to Ag ions. The purpose of testing the  $\text{Ge}_{32}\text{Se}_{68}$  devices was an effort to separate the electron conduction from the ion conduction in the Ag-only and Ag+SnSe devices. To achieve the goals of the work, low temperature conduction was analyzed.

### 6.2 Overview of Work

Three device types were analyzed in this work using voltage sweeps at temperatures ranging from 300 K down to 10 K. All devices used a common tungsten bottom electrode.

### 6.2.1 Devices Tested

The first device was resistive with 300 Å sputtered  $\text{Ge}_{32}\text{Se}_{68}$  material sandwiched between the common 600 Å W / 250 Å Cr electrode and a 380 Å sputtered W top electrode. The device size was 3 μm in diameter. The purpose of testing the device was to determine mechanisms of electron conduction that are present when a switching device is erased. The electron conduction of the resistive material also plays a role in the conduction of the switching devices. To test the resistive  $\text{Ge}_{32}\text{Se}_{68}$  device, voltage sweeps were performed up to 5 V using 1 nA compliance current limit. Temperatures were from 300 K down to 10 K.

The second device type tested was the Ag-only switching device. From top down, the device stack is 380 Å W top electrode, 100 Å  $\text{Ge}_{32}\text{Se}_{68}$ , 500 Å Ag, 300 Å  $\text{Ge}_{32}\text{Se}_{68}$  memory layer, 600 Å W, 250 Å Cr, Si substrate. This simple device is used to understand the mechanisms of Ag ion conduction in a switching device.

The third device type tested was the Ag+SnSe stack switching device. From top down, the device stack is 380 Å W top electrode, 100 Å  $\text{Ge}_{32}\text{Se}_{68}$ , 500 Å Ag, 150 Å  $\text{Ge}_{32}\text{Se}_{68}$ , 700 Å SnSe, 300 Å  $\text{Ge}_{32}\text{Se}_{68}$  memory layer, 600 Å W, 250 Å Cr, Si substrate. The purpose is to understand ion conduction in an engineered device.

### 6.2.2 Experiment Groups Within Devices

Devices were divided into two groups – those retested at each temperature and those tested fresh at each temperature. The intent was to compare the two groups since each includes different sources of variation. The retested devices include variation from device degradation as a result of mechanical changes due to probing and structural

changes as due to the voltage sweeps. The fresh devices include device-to-device process variation.

### 6.2.3 Conduction Mechanisms Investigated

For the resistive Ge<sub>32</sub>Se<sub>68</sub> devices, five electron-conduction mechanisms were investigated: Band conduction in the extended states, Mott's  $T^{-1/4}$  Variable Range Hopping, Schottky emission, Poole-Frenkel emission, and Fowler-Nordheim Tunneling.

For the Ag-only and Ag+SnSe switching devices, the mechanisms of Butler-Volmer electrochemical redox and Mott-Gurney ion hopping in addition to the electron-conduction mechanisms were investigated during the write operation. Also, it was noted that the Simmons equation for electron tunneling from localized impurity sites and vacancies has the same form as the Mott-Gurney ion-hopping equation.

To verify if the electron or ion-conduction mechanism is dominant, the IV curves were transformed using the equation of the mechanism of interest. If the transformed plot is linear, it may indicate that the mechanism is active.

## 6.3 Results

### 6.3.1 Electron Conduction in Ge<sub>32</sub>Se<sub>68</sub>

Five mechanisms were investigated. Schottky emission did not appear to be occurring since unreasonable permittivity values were obtained. The data did not fit Fowler-Nordheim tunneling. The remaining mechanisms of Band Conduction in Extended States, Mott's Variable Range hopping, and Poole-Frenkel emission had varying degrees of fit down to about 150 K. Parameters such as activation energy and relative permittivity were calculated. One device had a calculated permittivity value that

was close to the literature when using the Poole-Frenkel equation. Between devices, there was a large variation in the results. At temperatures below 150 K, none of the mechanisms fit. Conduction was higher than expected for low temperatures.

It is surmised that the dominant conduction mechanisms in 300 Å  $\text{Ge}_{32}\text{Se}_{68}$  are a combination of Band Conduction in Extended States, Variable Range Hopping, and Poole-Frenkel emission.

### 6.3.2 Conduction in Ag-Only and Ag+SnSe Switching Devices

Write traces showed that Ag-only devices did not fit to any of the electron-conduction mechanisms or to Butler-Volmer/Mott-Gurney ion-conduction mechanisms.

For Ag+SnSe devices at higher electric fields, there were indications of exponential performance, matching the BV redox and MG hopping. Ag-only devices reached threshold before any exponential performance could occur. Mott-Gurney hopping distance was calculated for the Ag+SnSe devices. The results were unreasonably large. In some cases, the hop distances were larger than the thickness of the  $\text{Ge}_{32}\text{Se}_{68}$  memory layer, which brings doubt to the validity of the results.

### 6.3.3 Threshold Voltage Characteristics

The threshold voltage marks the end of the write process. For this work, it is defined as the voltage at which the current through the device is 50  $\mu\text{A}$ . The threshold voltage increased with reduced temperature for all devices that were retested at each temperature. There was not a measurable difference in threshold voltage between the Ag-only and Ag+SnSe devices until temperatures below 200 K, where variation became very large. The conductance at threshold had Arrhenius thermally activated performance

in the temperature range of 300 K to 200 K. Below 200 K, the slope of the Arrhenius plot flattened out, indicating that threshold voltage is lower than expected for Arrhenius performance.

#### 6.3.4 Resistance Characteristics in Ag-Only and Ag+SnSe Switching Devices

Post write resistance was measured by sweeping voltage from 0 to 20 mV in 1 mV steps. Compliance current was set to 50  $\mu$ A to prevent the resistance state from being altered by the resistance readout. The performance up to 20 mV is linear.

Resistance is calculated by taking the inverse slope of the IV plot. The written resistance ranged from 10s of  $\Omega$  to 10s of k $\Omega$ . There was not a clear trend with temperature other than low resistance at low temperatures, which is probably due to top electrode breakage.

#### 6.3.5 Erase Characteristics

The erase process is accomplished by applying negative voltage to the top electrode. Metal from the filament is oxidized and moves via the electric field back towards the anode, creating a discontinuity in the filament, thus increasing device resistance. Erase traces show an ohmic response for low electric fields, then exponential, which is similar to the write characteristic. But because the source of Ag is limited, the current begins to decrease. Then, there is a sudden step function reduction in current when the main filament breaks contact, indicating that electron conduction in the amorphous Ge<sub>32</sub>Se<sub>68</sub> material is occurring. Some of the traces had multiple step function drops, potentially indicating multiple filaments, or a multifaceted filament.

#### 6.4 Future Work

At the conclusion of this work, some questions still remain about the nature of the materials used in the devices as well as the conduction mechanisms in the lowest temperature regimes. Analysis of the electron conduction in  $\text{Ge}_{32}\text{Se}_{68}$  showed that multiple mechanisms may be occurring at the same time in the temperature range of 300 K to 150 K. To further understand the mechanisms, more analysis on the device materials needs to be completed. Independent verification of the  $\text{Ge}_{32}\text{Se}_{68}$  permittivity using methods such as mercury probe could validate the Poole-Frenkel or Schottky permittivity values. Temperature analysis in both the high temperature and low temperature regions give more information on the temperature dependencies of conduction mechanisms.

None of the conduction mechanisms fit well to the data below 150 K. More work needs to be performed to understand the conduction mechanisms for very low temperatures. First, the experimental apparatus must be ruled out as an impact to the mechanisms by fixing the broken top electrodes. Then, testing should be performed using more temperatures to fully map the temperature of the conduction shift. If there is truly a fundamental performance shift below 150 K, more work needs to be performed to understand the source of the shift.

#### 6.5 Summary

Conductive-bridging memory devices offer a compelling solution that may become increasingly important in the future as electron storage memory reaches the physical boundaries of size and complexity. The conduction mechanisms of these

devices should be kept in mind while troubleshooting the challenges of making the device competitive with existing technologies.

## REFERENCES

- [1] Iliia Valov, Rainer Waser, John R. Jameson, and Michael N. Kozicki, "Electrochemical metallization memories - Fundamentals, applications, prospects," *Nanotechnology*, vol. 22, no. 25, June 2011.
- [2] C. Sandhya, P. K. Singh, S. Gupta, H. Rohra, M. Shivatheja, U. Ganguly, R. Hoffman, G. Mukhopadhyay, S. Mahapatra, J. Vasi, "Recent advances in charge trap flash memories," in *2nd International Workshop on Electron Devices and Semiconductor Technology*, 2009.
- [3] H. Tanaka, M. Kido, K. Yahashi, M. Oomura, R. Katsumata, M. Kito, Y. Fukuzumi, M. Sato, Y. Nagata, Y. Matsuoka, "Bit Cost Scalable Technology with Punch and Plug Process for Ultra High Density Flash Memory," in *IEEE Symposium on VLSI Technology*, 2007, pp. 14-15.
- [4] S. R. Ovshinsky, "Reversible electrical switching phenomena in disordered structures," *Physical Review Letters*, vol. 21, no. 20, pp. 1450-1453, Nov 1968.
- [5] C. Kim et al., "Direct evidence of phase separation in Ge<sub>2</sub>Sb<sub>2</sub>Te<sub>5</sub> in phase change memory devices," *Applied Physics Letters*, vol. 94, no. 19, pp. 193504-1 - 193504-3, 2009.
- [6] A. L. Lacaita and D. Ielmini, "Reliability issues and scaling projections for phase change non volatile memories," in *IEEE International Electron Devices Meeting*, 2007, pp. 157-160.
- [7] D. Strukov, G. Snider, D. Stewart, and S. Williams, "The missing memristor found," *Nature*, vol. 453, no. 7191, pp. 80-83, May 2008.
- [8] S. Q. Liu, N. J. Wu, and A. Ignatiev, "Electric-pulse-induced reversible resistance change effect in magnetoresistive films," *Applied Physics Letters*, vol. 76, no. 19, pp. 2749-2751, May 2000.
- [9] Yooichi Hirose and Haruo Hirose, "Polarity-Dependent memory switching and behavior of Ag dendrite in Ag photodoped amorphous As<sub>2</sub>S<sub>3</sub> films," *Journal of Applied Physics*, vol. 47, no. 6, pp. 2767-2772, June 1976.

- [10] Rainer Waser, Regina Dittmann, Georgi Staikov, and Kristof Szot, "Redox-based resistive switching memories nanoionic mechanisms, prospects, and challenges," *Advanced Materials*, vol. 21, no. 25-26, pp. 2632-2663, July 2009.
- [11] U. Russo, D. Kamalanathan, D. Ielmini, A. L. Lacaita, and M. N. Kozicki, "Study of multilevel programming in programmable metallization cell (PMC) memory," *IEEE Transactions on Electron Devices*, vol. 56, no. 5, pp. 1040-1047, May 2009.
- [12] John R. Jameson et al., "Quantized conductance in Ag/GeS<sub>2</sub>/W conductive-bridge memory cells," *IEEE Electron Device Letters*, vol. 33, no. 2, pp. 257-259, Feb 2012.
- [13] Deepak Kamalanathan, Ugo Russo, Daniele Ielmini, and Michael N. Kozicki, "Voltage-driven on-off transition and tradeoff with program and erase current in Programmable Metallization Cell (PMC) memory," *IEEE Electron Device Letters*, vol. 30, no. 5, pp. 553-555, 2009.
- [14] An Chen, "Ionic Memories: Status and Challenges," in *9th Annual Non-Volatile Memory Technology Symposium (NVMTS)*, Pacific Grove, CA.
- [15] A. Bard and L. Faulkner, *Electrochemical methods: fundamentals and applications*, 1st ed. New York, United State of America: John Wiley and Sons, 1980.
- [16] J. J. O'Dwyer, *The Theory of Electrical Conduction and Breakdown in Solid Dielectrics*. Oxford: Clarendon Press, 1973.
- [17] J. G. Simmons and R. R. Verderber, "New conduction and reversible memory phenomena in thin insulating films," *Royal Society A, Mathematical and Physical Sciences*, vol. 301, no. 1464, pp. 77-102, Oct 1967.
- [18] P. R. Emtage and W. Tantraporn, "Schottky emission through thin insulating films," *Physical Review Letters*, vol. 8, no. 7, pp. 267-268, Apr 1962.
- [19] M. Lj. Napijalo, "Temperature dependence of electric permittivity of linear dielectrics with ionic and polar covalent bonds," *Journal of Physics and Chemistry of Solids*, vol. 59, no. 8, pp. 1255-1258, Aug 1998.
- [20] Jai Singh and Koichi Shimakawa, *Advances in Amorphous Semiconductors*, D. D. Sarma, G. Kotliar, and Y. Tokura, Eds. Boca Raton, FL, USA: CRC Press, 2003, vol. 5.
- [21] J. Frenkel, "On Pre-Breakdown Phenomena in Insulators and Electronic Semiconductors," *Physical Review*, vol. 54, pp. 647-648, 1938.

- [22] M. Lenzlinger and E. H. Snow, "Fowler-Nordheim Tunneling into Thermally Grown SiO<sub>2</sub>," *Journal of Applied Physics*, vol. 40, no. 1, pp. 278-283, 1969.
- [23] A. K. Agarwal, S. Seshadri, and L. B. Rowland, "Temperature dependence of Fowler-Nordheim current in 6H- and 4H-SiC MOS capacitors," *IEEE Electron Device Letters*, vol. 18, no. 12, pp. 592-594, 1997.
- [24] Hewlett Packard. Agilent (HP) 4156A Manual. [Online].  
[http://www.home.agilent.com/upload/cmc\\_upload/All/04155-90015.pdf?&cc=US&lc=eng](http://www.home.agilent.com/upload/cmc_upload/All/04155-90015.pdf?&cc=US&lc=eng)
- [25] Agilent Technologies: Why do the Agilent 4155 and 4156 source measurement units (SMUs) use triaxial cables? [Online].  
<http://www.home.agilent.com/agilent/editorial.jsp?cc=US&lc=eng&ckey=27666:atg:faq&nid=-34161.0.00&id=27666:atg:faq>
- [26] A. Feltz, H. Hust, and A. Blayer, "Glass formation and properties of chalcogenide systems XXVI: Permittivity and the structure of glasses As<sub>x</sub>Se<sub>1-x</sub> and Ge<sub>x</sub>Se<sub>1-x</sub>," *Journal of Non-Crystalline Solids*, vol. 55, no. 2, pp. 179-190, May 1983.